INTERACTIONS OF NANOMATERIALS WITH BIOLOGICAL SYSTEMS: A STUDY OF BIO-MINERALIZED NANOPARTICLES AND NANOPARTICLE ANTIBIOTICS

by

Jennifer Chappell Gifford

B.S., Trinity College, 2009

A thesis submitted to the

Faculty of the Graduate School of the

University of Colorado in partial fulfillment

of the requirement for the degree of

Doctor of Philosophy

Department of Chemistry and Biochemistry

2015

This thesis entitled:

Interactions of Nanomaterials with Biological Systems: A Study of Bio-Mineralized Nanoparticles and Nanoparticle Antibiotics

written by Jennifer Chappell Gifford
has been approved for the Department of Chemistry and Biochemistry

_____

Dr. Daniel L. Feldheim
(Committee Chair)

_____

Dr. Dylan Taatjes

Date:_____

The final copy of this thesis has been examined by the signatories, and we find that both the content and the form meet acceptable presentation standards of scholarly work in the above mentioned discipline.

Gifford, Jennifer Chappell (Ph.D., Biochemistry, Dept. of Chemistry and Biochemistry)

Interactions of Nanomaterials with Biological Systems: A Study of Bio-Mineralized Nanoparticles and Nanoparticle Antibiotics

Thesis directed by Professor Daniel L. Feldheim

Nature is continually able to out-perform laboratory syntheses of nanomaterials with control of specific properties under ambient temperatures, pressures and pH. The investigation of existing biomolecule-mediated nanoparticle synthesis provides insight and knowledge necessary for duplicating these processes. In this way, peptides or proteins with nanomaterial mediation capabilities can be: 1) explored to further understand the ways in which biomolecules create specific nanoparticles then 2) used to create genetically encodable tags for use in electron tomography. The goal of designing such a tag was to assist in closing the resolution gap that exists in current imaging techniques between approximately 5 nm and 100 nm. Presented in this thesis are examples of peptides and proteins that form iron oxide, silver or gold nanoparticles under discrete circumstances. Three iron oxide-related bacterial proteins – bacterioferritin, Dps and Mms6 – were investigated for potential use. Similarly, a silver mineralizing peptide, Ge8, was studied upon attachment to the filamentous protein, FtsZ, and a gold mineralizing peptide, A3, was examined to characterize the way in which it mediates the formation of both Au^0 nanoclusters and nanoparticles.

Given the established interactions that occur between nanoparticles and biomolecules, it may not be surprising that gold nanoparticles displaying specific ratios of functional groups are able to interact with bacteria, in some cases inhibiting growth or

causing cell death as antibiotics. A previously developed small molecule variable ligand display (SMVLD) method was expanded to identify a nanoparticle conjugate with a minimal inhibitory concentration ($MIC_{99.9}$) of 6 μM for *Mycobacterium smegmatis*, a common laboratory model for *M. tuberculosis* and the first example of SMVLD applied to mycobacteria. Nanoparticle structure-activity relationships, modes of action and approximations of mammalian cell toxicities were also explored to expand our understanding of how these nanoparticle antibiotics function and increase our ability to rationally design potential nanoparticle therapeutics for specific targets in the future. Finally, a new method for on-particle ligand quantitation via solid-state NMR spectroscopy was developed and applied to three different cases of nanoparticle conjugates.

Acknowledgements

I would like to express my gratitude to numerous mentors, colleagues, labmates and collaborators who have contributed in some way to the work presented in this thesis. First, I would not be writing the dissertation for my PhD without the support, guidance and help from my graduate advisor, Dr. Dan Feldheim. The Feldheim laboratory members, both current and former, have also been instrumental in providing endless hours of discussion, feedback, understanding and encouragement throughout the last six years. Particularly, there is no way substantial enough to express my appreciation to Dr. Carly Carter, who not only acted as a teacher, mentor and role model during my graduate career, but also was a fantastic friend and family away from home.

I also need to recognize the many people on campus, both in and out of the department, who assisted me in setting up new experiments, instrument training and use, scheduling, advising, etc. Specifically, Theresa Nahreini, who oversees the mammalian cell culture facility in JSCBB, Dr. Rich Shoemaker, director of the departmental NMR facility, and Dr. Tom Giddings, director of the Electron Microscopy services on campus, were enormously contributory to several aspects of the research presented. Similarly, our collaborators in Dr. Christian Melander's laboratory at North Carolina State University contributed greatly.

Finally, I have to thank the Bill and Melinda Gates Foundation, NIH and University of Colorado Boulder for their financial support throughout my graduate career. In particular, the Graduate School and Dr. John Stevenson, its Dean, should be recognized for granting me a Dean's Grant for the last year of my PhD research, without which crucial experiments would not have been possible.

Table of Contents

Tables

Figures

CHAPTER 1

Genetically Encodable Tags

1.1 Introduction & Background

1.1.1 Biomaterials

The existence of naturally occurring biomolecules that serve a specific purpose, particularly in relation to the chemistry, formation and binding of nanomaterials, is a fact that cannot be ignored. There are a large number of proteins that biology has already evolved to sequester toxic metal ions in the form of inorganic nanoparticles or to assemble materials for structural rigidity. For example, magnetotactic bacteria synthesize internal iron oxide bar magnets that allow self-orientation along the Earth's geomagnetic lines, as shown in Figure 1.1.[1]

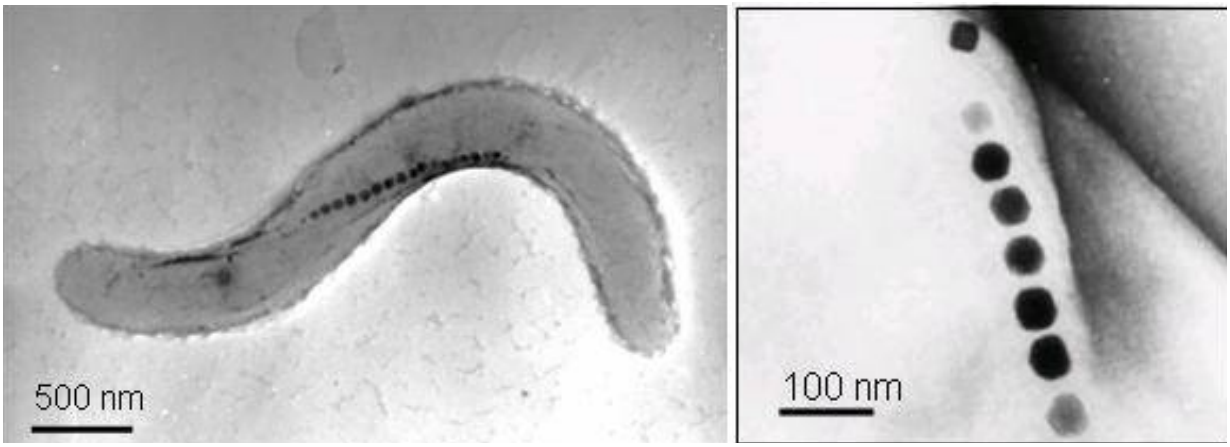

Figure 1.1 Transmission electron micrographs of the internal iron oxide bar magnet in *Magnetospirillum magnetotacticum*. (Adapted from ref. 1)

Calcium carbonate is frequently employed by marine organisms, forming both domes on the arms of the brittle stars to focus light, which alerts the organism to changes in its surrounding environment, and the hard, porous matrices that support coral growth and form extensive coral

reefs.[2, 3] When combined with phosphate, calcium also provides bones with the structure that allows substantial structural strength and integrity in all vertebrates.[4]

Often, laboratory material syntheses are unable to replicate nature. In cases when natural materials may be recreated, extreme reaction conditions are regularly required (i.e. time, temperature, pressure). It is of interest to understand the ability of biomolecules to synthesize specific materials under ambient temperature and pressure, and at neutral pH. If we can further our understanding of the reactions mediated by various biomolecules, laboratories would be able to then exploit strategies used in nature to more easily synthesize and control the formation of innumerable materials.

This thesis will investigate the chemistry of several biomolecules, both proteins and peptides, to develop a more in-depth knowledge of the reactions they mediate and the materials that result. Bacterioferritin (Bfr), DNA protection sequence (Dps) and a magnetotactic bacterial protein family (Mms) are three examples of relevant proteins that are known to mediate the formation of and/or interact with iron oxides in cells. Two peptides, named Ge8 and A3, will also be discussed for their ability to mediate the formation of Ag^0 and Au^0 nanoparticles, respectively.

1.1.2 Gap in intracellular imaging techniques

A second goal was to exploit the above biomolecules for use as genetically encodable tags. For cellular imaging techniques, there currently exists a resolution gap ranging from approximately 5 nm to 100 nm in which cellular biomolecules cannot be identified with high precision.[5] Unfortunately, the interactions between biomolecules generally occur in this size regime. Larger scales depend on optical and fluorescence microscopy to visualize whole cells

and tissues, whereas smaller objects, such as individual biomolecules, can be observed via structural techniques (NMR spectroscopy, X-ray diffraction, etc.).

The on-going development of several microscopy techniques has allowed the missing size regime to be decreased somewhat in the past two decades. Specifically, extensions of fluorescence microscopy, including stimulated emission depletion (STED), structured illumination (SI) and photoactivation light microscopy (PALM), have begun to close the previously mentioned resolution gap using signal averaging or other equivalent methods.[6, 7] In traditional fluorescence microscopy techniques, the resolution limit depends on both the size of the fluorescent excitation spot, typically half of the excitation wavelength, as well as the diameter of the pinhole through which the fluorescence is collected by the camera.[8] STED uses a normal excitation pulse followed by a longer, near-infrared pulse to deplete fluorescence emitted from the edge of the excitation spot, narrowing the excitation beam spot size by about five-fold; this method results in an approximate two-fold increase in the resolution achieved.[9]

In an alternative approach, structured illumination also is able to achieve a two-fold increase in resolution. This method takes advantage of moiré fringes that appear when two line patterns are superimposed. In this case, one pattern is generated by structured excitation light and is known, whereas the second contributing pattern comes from the sample and is unknown. By collecting images using various phases of the structured excitation light, increasing amounts of information about the sample can be gained. Via arithmetic and data processing to remove the known line pattern, the remaining pattern due to the sample can be determined.[10]

Finally, PALM employs repeated cycles of photo-activation, measurement and bleaching of the photo-activated fluorescent proteins. Again, through extensive data processing, each image can be plotted over x, y and t (time) axes in order to uniquely isolate the signal from each

fluorescent molecule present.[11] A non-linear least squares algorithm fits the resulting data to a Gaussian distribution with a factor for assumed uncertainty. By summing the Gaussians from each image collected, a probably density map is acquired where brightness is directly related to the likelihood of a fluorescent molecule being found in that location. In the best-case scenarios, i.e. observation of the brightest fluorescent molecules, PALM can separate features down to only a few nanometers.[12]

While all of these techniques reach resolutions below the limit of standard optical microscopy, each also has its own drawbacks. Both PALM and SI methods require significant data processing in order to obtain the final, higher resolution image, while STED fluorescence microscopy has a more complex instrument setup than traditional microscopes. Most importantly for this thesis, however, is that all fluorescence microscopy methods, despite resolution improvements, image only the fluorescent molecule and not the underlying protein. The protein of interest is tagged with a fluorescent protein, from which a fluorescent signal is visualized, instead of the actual tagged protein. In contrast, electron-based microscopy techniques, such as electron tomography, have the resolution to directly observe both the protein of interest and the tag simultaneously.

1.1.3 Electron tomography

Electron tomography is a three-dimensional, transmission electron microscopy technique in which a tilt series of images is collected and reconstructed to form a three-dimensional image of an object or specimen. Since this technique relies on the wavelength of electrons instead of photons, it has a resolution of only a few nanometers, much lower than that of light microscopy.[13, 14] In this way, one can directly image proteins within a biological system in their native state (cells are commonly vitrified prior to imaging by electron tomography). Vitrification

flash freezes cells before imaging, rather than requiring the addition of a fixative reagent that may alter the integrity of the biological system.

One limitation, however, is the difficulty of definitively differentiating individual proteins from one another within a tomogram due to their equally low electron density. Unless there exists a defining feature in the tomogram, such as the example shown in Figure 1.2, most proteins simply appear as similar-looking, globular entities, with no features that distinguish one from another.[15]

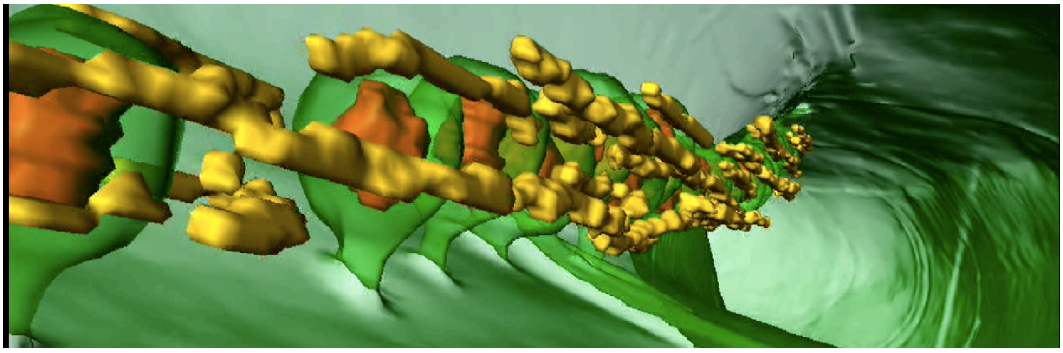

Figure 1.2 Three-dimensional electron tomogram reconstruction of the same iron oxide as Figure 1.1 within *Magnetospirillum magnetotacticum*. In this example, the presence of higher density iron oxide nanoparticles and the unique structure of the surrounding proteins allows for discrete identification of each entity and false coloring to be applied for clarity, atypical for many traditional tomograms collected. (Adapted from ref. 15)

The addition of unique, electron dense material onto a protein of interest would provide contrast and act as a marker, resulting in visualization of both the protein of interest and the tethered higher contrast, distinct tag in a tomogram. A genetically encoded biomolecule that both mediates the synthesis of and then binds the resulting metal or metal oxide nanoparticles could create the necessary electron dense material (i.e. nanoparticle) associated with a protein of interest when expressed as a chimera and after addition of the required precursor metal ions. A schematic of the proposed system is depicted in Figure 1.3. In summary, specific nanomaterial-

related biomolecules could serve as genetically encodable tags for the clear identification of proteins within a tomogram, further filling in the resolution gap.

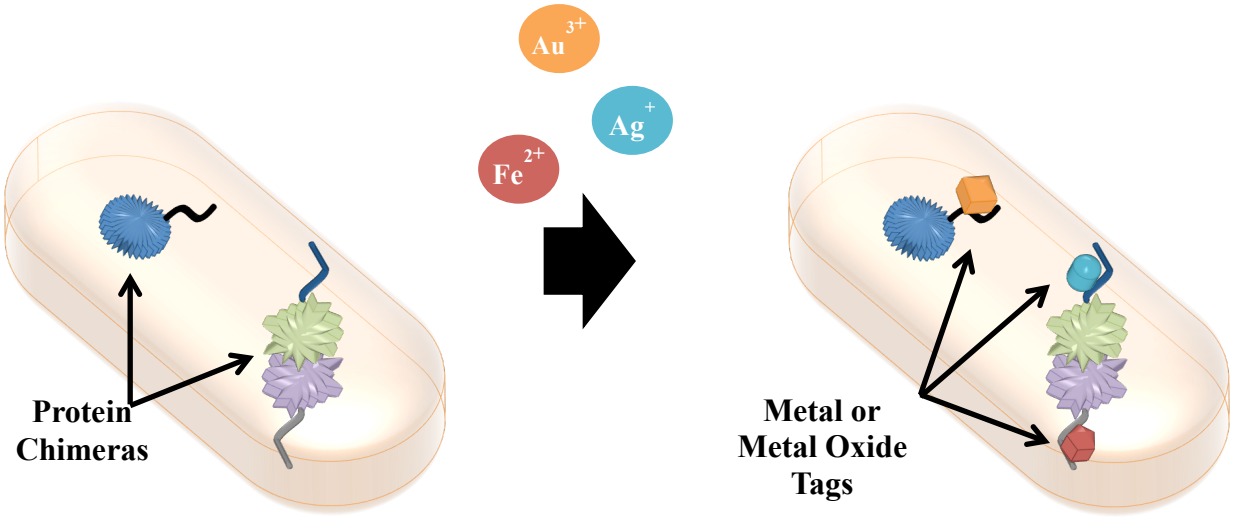

Figure 1.3 Genetically encodable tag diagram. Peptides or proteins that are able to mediate the formation of a unique metal or metal oxide nanoparticle are attached to intracellular proteins of interest. Metal ion precursors are then introduced and each peptide or protein forms its specific nanoparticle at the location of each chimera.

1.2 Development of iron-mineralizing protein chimeras

1.2.1 Iron mineralization

1.2.1.1 In water

In aqueous environments, iron cations exist in numerous complexes, the presence of each governed by specific conditions. In pure water under anaerobic conditions and below pH 7, water-based coordination occurs in the form $[Fe(H_2O)_6]^{z+}$, where z is the oxidation state of the ferrous (Fe^{2+}) or ferric (Fe^{3+}) iron cation. These aquo complexes are converted to hydroxylated species as the pH of the solution increases, leading to the precipitation of iron oxide or hydroxide solids. Anaerobic condensation of ferrous iron complexes at pH > 7 results in the formation of fairly insoluble $Fe(OH)_2$ ($K_{sp} \approx 2 \times 10^{-15}$).[16, 17]

In aerobic conditions, however, ferrous ions are oxidized to ferric iron, forming the complimentary hydroxylated ferric complexes. The hydroxo ligands then act as nucleophiles to remove water and form hydroxo bridges between consecutive iron cations; this process is known as olation. Repeated olation results in the formation of polymeric ferrihydrite, approximated as $Fe_2O_3 \cdot 0.5H_2O$. Alternatively, oxolation, in which the association of two hydroxylated species forms oxo bridges, can take place after olation.[18, 19, 20]

While all of these reactions result in the formation of various iron oxide species, they are highly dependent on temperature, pH and concentration. For example, ferrihydrite only dehydrates to hematite (α-Fe_2O_3) at pH values between 5 and 8 over an extended period of time ($t_{1/2}$ = 100 days). Similarly, the co-precipitation of ferrous and ferric iron creates magnetite (Fe_3O_4) but only at pH values greater than 8. Magnetite is sensitive to oxygen and can be converted to maghemite (γ-Fe_2O_3) by exposure to aerobic or acidic conditions and high heat (200-400°C).[16, 18, 19, 20, 21]

In more complex, natural water systems, the solubility of iron is influenced by the presence of other anions, primarily carbonate (CO_3^{2-}), sulfide (S^{2-}) and phosphate (PO_4^{3-}). At pH < 9, ferrous iron has increased solubility ($K_{sp} \approx 3 \times 10^{-11}$) with up to 2 mM carbonate.[16, 22] While sulfide typically exists in lower concentrations that carbonate (estimated to be $\leq$ 0.1 mM), it can decrease the solubility of ferrous iron up to pH 10 ($K_{sp} \approx 6 \times 10^{-19}$).[16, 22] Finally, while the aqueous solubility of ferric iron is substantially lower than ferrous iron in water ($K_{sp} \approx 4 \times 10^{-38}$ vs. $K_{sp} \approx 2 \times 10^{-15}$),[23] coordination by phosphate anions (PO_4^{3-}) does improve ferric iron solubility by several orders of magnitude ($K_{sp} \approx 6 \times 10^{-22}$).[16, 22, 24]

1.2.1.2 In proteins

Numerous native iron-binding proteins have been identified in plants, humans, animals and bacteria. While many of these proteins use iron or iron complexes as cofactors or for their catalytic activity, the most relevant function of iron-binding proteins to this thesis is the storage and regulation of iron *in vivo*.[25, 26, 27] Bacterioferritin (Bfr), DNA protection sequence (Dps) and proteins from magnetotactic bacteria (*Magnetospirillum magnetotacticum*) have each been thoroughly studied in an effort to better understand their iron binding capabilities as well as their ability to manipulate an inorganic material (iron) under conditions of neutral pH and ambient temperatures and pressures. Both Bfr and Dps proteins are well known mediators of the formation of iron oxides for iron storage in various cell types. Similarly, the magnetotactic bacterial protein family Mms binds tightly to iron oxides synthesized *in vivo*, specifically magnetite (Fe_3O_4), to create their previously mentioned internal bar magnets.[1]

Two iron-based protein tags for potential use in electron tomography have been developed. The first combines the iron chemistry of Bfr with the iron oxide binding properties of Mms; the entire construct is referred to as FLF$(mms6)_2$. Second, several alterations of Dps protein capsules (referred to as DPS_x, where x indicates the number of subunits) were developed and employed to investigate the possibility of also using Dps as a biomineralizing tag. Both of these constructs will be described in detail in the following sections.

1.2.2 FLF$(mms6)_2$

1.2.2.1 Rationale and schematic

Bacterioferritin is a 24-mer-ferritin protein found in *Escherichia coli* that sequesters Fe^{2+} ions. At high environmental iron concentrations, this sequestering activity starts at binuclear ferroxidase sites located between two monomer units to protect the cell from oxidative radical

damage; these sites facilitate a form of the Fenton reaction to oxidize Fe^{2+} to Fe^{3+}, which is then stored as ferric-oxyhydroxide within a cavity 80-Å in diameter inside the fully assembled protein (see Figure 1.4).[28] When full, the Bfr capsule can accommodate approximately 4,500 Fe^{3+} ions.[29] The ferric ions can then be released from the capsule to maintain cellular iron concentrations between micromolar and millimolar ranges. Iron release is not as well understood but there is evidence that ferric iron is reduced to ferrous iron and exits the mineral core along the same pores used for iron entry.[30] Additionally, it has been shown that a triggered opening of these pores, specifically by lysosomes in mammalian cells, is required for ferrous iron release.[31] Finally, the residues required for assembly of the 24-mer capsules have been identified and can be altered to prevent full cage assembly, resulting in the formation of only the dimer. It is important to note that in this dimeric mutant, the ferroxidase site does remain active.[27]

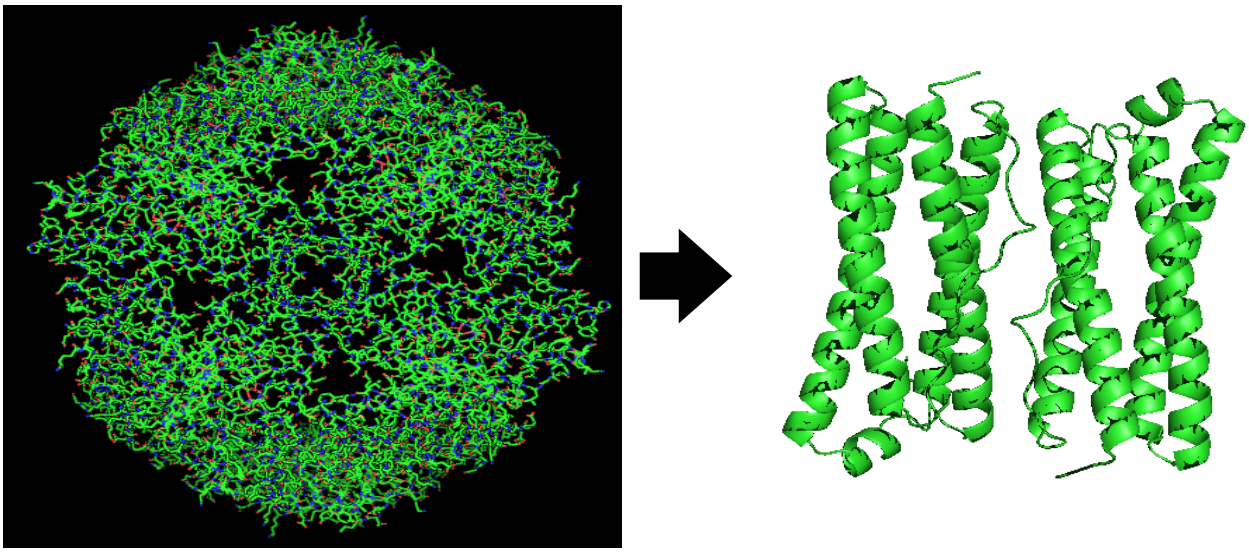

Figure 1.4 *E. coli* bacterioferritin (Bfr) as a fully formed iron storage capsule (left) and stripped down to the dimer containing the ferroxidase site that was used in the $FLF(mms6)_2$ construct (right).

The bacterium *Magnetospirillum magnetotacticum* has the ability to synthesize Fe_3O_4 *in vivo*. While many proteins in this organism have been identified as playing some role in mediating the synthesis of magnetite, the iron chemistry that occurs has not been fully

elucidated. One specific protein family, Mms, falls into this category: the proteins have been observed to bind tightly to magnetite once synthesized, but their role in magnetite formation is unknown.[1] Mms6, a member of the Mms protein family with a molecular weight of 6 kDa, has been identified as a key protein in magnetite binding through its hydrophilic C-terminus, which chelates iron by means of numerous carboxyl and hydroxyl functional groups.[32, 33] A fusion of the iron chemistry performed by a Bfr dimer with the iron oxide binding capabilities of Mms6 allowed for our first combination of both formation and binding of nanoparticles, as required by an iron oxide genetically encodable tag for potential use in electron tomography.

1.2.2.2 Protein engineering

The protein construct, named FLF(mms6)$_2$, is the chimera of an assembly-deficient Bfr dimer and two duplicate portions from the C-terminus of Mms6. Since Bfr is natively a 24-mer, the assembly-deficient mutant was used to decrease the overall size of the chimera, while still maintaining ferroxidase activity. The two individual units of the dimer were tethered together by a sequence of sixteen glycine residues, theoretically providing enough freedom for the monomers to interact as normal and form their active sites. The addition of two Mms6 fragments, specifically the acidic triplets of amino acids found in the C-terminal half of the Mms6 protein, was hypothesized to provide a binding location for the oxidized iron. In this configuration, it was proposed that the ferritin components would allow the iron oxidation chemistry to occur and the Mms6 elements would then bind the reacted iron. A schematic of the plasmids created is presented in Figure 1.5.

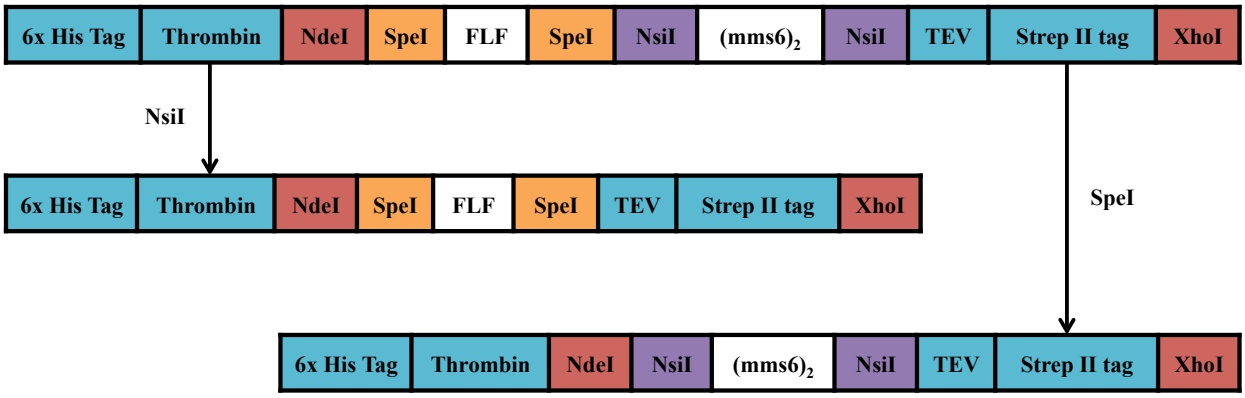

Figure 1.5 Schematic of FLF(mms6)$_2$ plasmid insert (white) with restriction sites (red, orange and purple) and affinity tags (blue) labeled. Plasmids were digested with NsiI (purple) and SpeI (orange) restriction enzymes to obtain FLF and (mms6)$_2$ alone, respectively.

The FLF(mms6)$_2$ protein was successfully expressed and purified from BL21 DE3 pLysS chemically competent *E. coli* as confirmed by sodium dodecyl sulfide polyacrylamide gel electrophoresis (SDS-PAGE). Interestingly, upon pelleting of the cells with over-expressed proteins to prepare for lysis, there was a distinct reddish-pink color observed in the cell pellet (Figure 1.6). The color seen, as compared to the typical pale beige of a control cell pellet, was an indication of increased *in vivo* iron in the presence of our FLF(mms6)$_2$ protein construct. Throughout numerous purification steps, including lysis, affinity columns, quaternary amine (Q) columns, desalting on Amicon filters and dialysis, this color remained associated with the recombinant protein; it was assumed that this reddish hue was the observable result of iron oxide formation due to the protein. This was particularly surprising since neither the media nor purification buffers were supplemented with iron at any point, indicating the high affinity our protein conjugate has for trace iron that is present in the media and/or cells.

Figure 1.6 Cell pellet colors representing *E. coli* only on the left and *E. coli* over-expressing FLF(mms6)$_2$ on the right.

Additionally, the FLF(mms6)$_2$ gene created for over-expression was specifically designed with restriction sites surrounding and unique to each

half of the construct, SpeI for the removal of FLF and NsiI for the removal of $(mms6)_2$ (refer again to Figure 1.5). The plasmid for FLF$(mms6)_2$ was successfully digested with each of these restriction enzymes in order to isolate both FLF only and $(mms6)_2$ only proteins. Similarly to the original protein chimera, these individual portions were over-expressed and purified. However, only cell pellets containing the FLF portion continued to show the distinct reddish tint, possibly indicating that iron oxide binding was occurring without the aide of Mms6 as originally intended. Cell pellets containing only the over-expressed $(mms6)_2$ fragment were observed to have no color difference from a control pellet, equally beige.

1.2.2.3 Nanoparticle characterization

Once purified, all three proteins were concentrated, then washed and dialyzed with water to remove any remaining elution buffer. To initially confirm the presence of iron in the purified protein samples, aliquots were submitted for inductively coupled plasma optical emission spectrometry (ICP-OES). As listed in Table 1.1, all three samples contained varying amounts of iron, which could only have come from their *in vivo* expression during growth, as neither elution buffer used during purification steps contained iron. While this experiment was only performed one time and therefore the results are not statistically significant, it did convince us that there was iron associated with the purified proteins, leading to further investigation.

Once the co-existence of iron and purified protein was indicated, transmission electron microscopy techniques were utilized to further elucidate properties of the iron present. Images of FLF$(mms6)_2$ by transmission electron microscopy showed spherical nanoparticles, 6.8 nm ± 4.4 nm in diameter. Electron diffraction d-spacings of these particles best matched α-FeOOH, within 5% error. Similarly, 4 nm ± 1 nm and 8 nm ± 2 nm particles were observed with FLF and $(mms6)_2$, respectively. Electron diffraction patterns for both most closely matched γ-Fe_2O_3, again

within 5% error. Representative TEM and electron diffraction images are shown in Figure 1.7 and the measured d-spacings used for possible material assignments are listed in Table 1.2. In this table, the "measured d-spacings" listed are all d-spacings observed in electron diffraction images, whereas the "assigned d-spacings" are the most likely assignment of each of those measured quantities to known values for various iron oxide phases. Due to slight variations in electron diffraction images and d-spacing measurements, the number of d-spacings observed or the value for any given d-spacing could vary, even for samples of the same iron oxide phase. Growth media and elution buffer run through the same purification steps have also been analyzed by TEM as controls; nanoparticles were not observed in either case.

Table 1.1 Iron concentrations present in one analysis via ICP-OES of several solutions. (N/A = not applicable as these solutions contained no protein, DL = measurement could not be reported as the value was below the detection limit of the instrument)

Sample Identity	Protein Conc., µM	Iron Conc., µM
Luria Broth	N/A	4
Elution Buffer (Strep II)	N/A	DL
Elution Buffer (6x His)	N/A	DL
FLF(mms6)$_2$	19	8.0
FLF	20	8.2
(mms6)$_2$	116	2.3

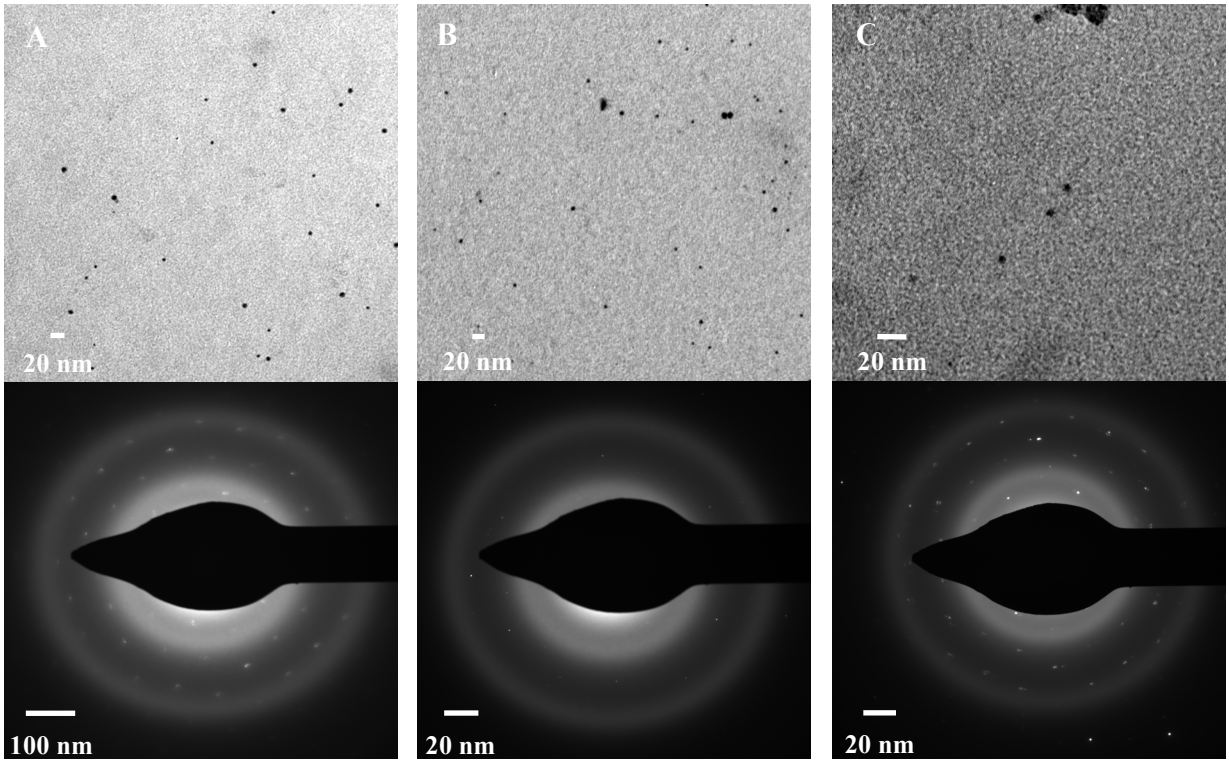

Figure 1.7 Representative TEM images of nanoparticles formed by purified FLF(mms6)$_2$ (A), FLF (B) and (mms6)$_2$ (C), and corresponding electron diffraction patterns below each.

Table 1.2 Measured d-spacings from the electron diffraction patterns of each ferritin-based tag investigated. These measurements are shown in comparison to the known d-spacings to which they were assigned, as well as the final material determination based on this comparison. The d-spacings in bold type are the most intense reflections for each predicted iron oxide phase.

Protein Tag Identity	Measured d-spacings	Assigned d-spacings	Predicted Iron Oxide Phase
FLF(mms6)$_2$	4.777	4.608	α-FeOOH
	4.305	**4.182**	
	3.529	3.380	
	2.732	2.693	
	2.251	2.250	
	1.697	1.719	
FLF	**5.801**	**5.899**	γ-Fe_2O_3

	3.833	3.731	
	3.043	3.295	
	2.614	2.638	
	2.420	2.49	
	2.079	2.086	
$(mms6)_2$	**5.771**	**5.899**	γ-Fe_2O_3
	5.020	4.816	
	3.845	3.731	
	3.385	3.406	
	2.807	2.781	
	2.369	2.490	
	2.026	2.023	
	1.719	1.703	

It should be noted that NaCl is also present in these samples and has similar d-spacings to several iron oxide phases. Therefore, nanoparticles were imaged by a dark-field scanning transmission electron microscope (DF-STEM) equipped with energy dispersive X-ray spectrometry (EDS) to differentiate between salt and iron oxide. EDS is a technique in which an x-ray source is used to excite a sample; if an atom in the sample absorbs an x-ray with sufficient energy, electrons are ejected from the core or inner shells of that atom. In order to stabilize after this event, an electron from the K, L or M outer shells releases energy and moves into the vacant, inner shell spot. The energy released is an x-ray and is characteristic of the atom.[34] Nanoparticles less than 20 nm in diameter were the primary focus, as NaCl was assumed to form the large crystals (> 50 nm) visible by TEM. An EDS spectrum obtained did verify that the nanoparticles

considered contain iron, as speculated; however, due to time constraints and issues with sample visibility under the necessary conditions to perform EDS, this was only performed one time. The spectrum, from a nanoparticle found in the DF-STEM image of a FLF(mms6)$_2$ sample, is shown in Figure 1.8 with characteristic peaks of decreasing intensity for the K_α (6.40 keV), L_α (0.70 keV) and K_β (7.06 keV) emission lines of iron.[35]

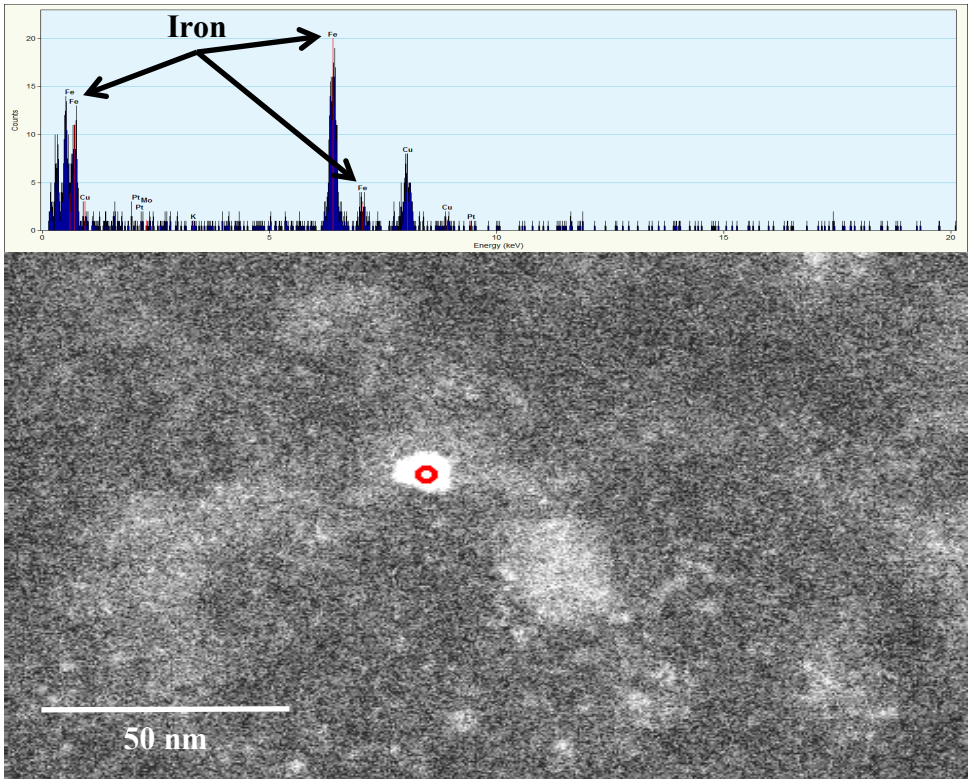

Figure 1.8 Image of nanoparticle from FLF(mms6)$_2$ sample by DF-STEM (below) and corresponding EDS spectrum (above) indicating the presence of iron. The red circle indicates the location from which the EDS measurement was obtained.

Finally, it was also of interest to titrate $FeSO_4$ into aliquots of the protein constructs to elucidate how iron "loading" may affect the resulting nanoparticles seen by TEM. For this experiment, iron oxide nanoparticles were observed and measured after each purified protein construct was incubated with varying concentrations of iron (II) sulfate (0.1 mM, 0.5 mM or 1 mM $FeSO_4 \cdot 7H_2O$). Ferrous sulfate heptahydrate was used as it is readily soluble in water

(solutions are acidic between pH 3 and 4, allowing dissolution of Fe^{2+} as previously described due to higher solubility constants at low pH),[36] but no effort was made to control exposure to oxygen (aerobic conditions) or changes in pH over the course of the incubations with protein. Solutions of ferrous iron were prepared fresh and immediately prior to use to minimize oxidation followed by precipitation of Fe^{3+}.

These experiments resulted in nanoparticles that were smaller in diameter on average, as well as with a narrower size distribution. It is hypothesized that the increased presence of ferrous iron resulted in more proteins able to create an iron oxide nanoparticle, but therefore, the resulting nanoparticles were also smaller in size. In other words, smaller, but more uniform nanoparticles were able to form on a higher percentage of protein constructs, rather than only a small percentage of proteins scavenging the available iron during cell growth and protein expression. It is possible that during protein over-expression, the first constructs produced rapidly scavenge whatever limited available iron exists, resulting in an iron-deficient environment for subsequent proteins and lack of iron mineralization occurring in these protein constructs. A summary of these measurements is presented in Table 1.3.

Table 1.3 Resulting measurements and standard deviation produced from each component of $FLF(mms6)_2$ with and without the addition of ferrous iron to the purified protein.

Protein Tag Identity	Amount of Fe^{2+} added (mM)	Size distribution of nanoparticles (nm)
$FLF(mms6)_2$	None	6.8 ± 4.4
	0.1	2.6 ± 0.4
	0.5	2.7 ± 0.4
	1	2.6 ± 0.3
FLF	none	4 ± 1

	0.1	N/A
	0.5	2.3 ± 0.4
	1	N/A
$(mms6)_2$	none	8 ± 2
	0.1	3.5 ± 0.7
	0.5	2.2 ± 0.5
	1	2.3 ± 0.6

1.2.3 DPS

1.2.3.1 Rationale and schematic

The protein Dps (DNA protection sequence) plays a similar role in iron sequestration as Bfr, converting ferrous iron to ferrihydrite using hydrogen peroxide and storing the resulting ferric iron for future cellular use.[37] This protein capsule is made up of twelve 18-kDa subunits, in comparison to the Bfr 24-mer, but forms a similarly sized capsule (approximately 9 nm in diameter internally for Dps vs. 8 nm for Bfr).[38] Despite the capsule diameter likeness to Bfr as well as having an additional ferroxidase site per dimer, Dps can only store about 500 Fe^{3+} ions within its core.[33, 34] A PyMol rendition of the active dimer unit is illustrated in Figure 1.9. The capsule is formed by hydrophobic interactions

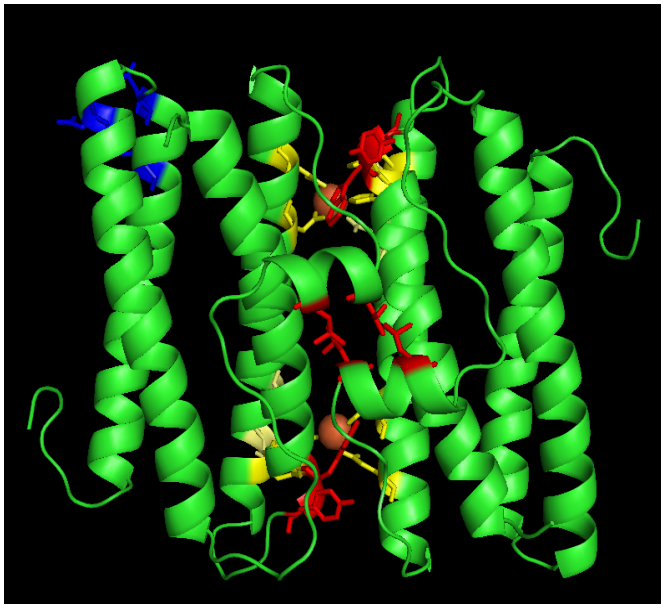

Figure 1.9 PyMol rendering of one active dimeric unit of the total 12-mer Dps capsule. Three hydrophilic residues (D121, D126 and D130) at the N-terminus of three monomers form the pore through which Fe^{2+} enters the capsule (blue). Hydrophobic residues from each monomer interact to form the dimer (red). E62 and D58 (from one monomer) with H31 and a bridging water molecule from H43 (on the second monomer) form each ferroxidase site (yellow); there are two sites created by one dimer. Finally, ferric iron exits the ferroxidase sites along E44 and D47 (pale yellow).

between each monomer and the N-terminal residues of three monomers allow Fe^{2+} entrance into the capsule via a hydrophilic pore. Ferrous iron is then converted into ferric iron by one of the two available ferroxidase sites. Once oxidized, iron is shuttled along glutamic and aspartic acid residues to form the ferrihydrite ($Fe_2O_3 \cdot 0.5H_2O$) core.[20] Since this iron capsule requires half the number of subunits, we hypothesized that native Dps may be able to act as a tag without significant engineered alterations.

1.2.3.2 Protein engineering

Several combinations of Dps monomers have been linked together (designated DPS, DPS_2, DPS_5, DPS_6, DPS_7 and DPS_{12}) to allow for assembly of the full 12-mer for use as a tag; see Figure 1.10 for a schematic of the generic plasmid insert. In this case, the linker used between each monomer was the specific peptide sequence EPRGPTIXXKPCPPCKCPAPNLL GGP, chosen for its length, loop-like structure and lack of protease or DNA restriction sites.

Figure 1.10 Schematic of the gene insert of all Dps-based constructs in pET15b. In the case where x > 1, the codons for the peptide linker EPRGPTIXXKPCPPCKCPAPNLLGGP were inserted between each Dps subunit. This linker was chosen for its limited loop structure, which also lacks protease and restriction enzyme sites, to allow for maximum flexibility and unhindered ability for the units to interact with one another.

Initially, the Dps monomer (DPS) and dimer (DPS_2) constructs were expressed and shown to create the fully assembled 12-mer of the native Dps protein via heat precipitation experiments and TEM. Lysates containing over-expressed Dps constructs were first subjected to 70°C for 10 minutes, removing all thermally unstable proteins. Native Dps capsules are well known for their thermal stability;[39] therefore, survival of this purification step was one indication that the engineering capsules displayed at least similar thermal properties to native Dps capsules.

Purified constructs were also visualized by TEM after staining. Again, the observation of intact "donuts" was used as an indication that the native structure had been maintained.

These observations led to two important conclusions about the constructs. First, the addition of an affinity tag and restriction sites to the monomer unit had not affected its ability to form a capsule, and second, the peptide sequence chosen to act as a linker to form the dimer construct has sufficient length and flexibility to also allow capsule formation. However, the use of either of these constructs would require twelve (for DPS) or six (in the case of DPS_2) recombinant units to come together to form an intact and functional tag. This is not ideal for the following reasons. Primarily, this system would rely on diffusion within the cell for the components to reach each other and so may not be as well controlled or reliable. Additionally, the need for many units to come together could create a Dps capsule decorated with the tagged protein of interest, instead of the tagged protein being decorated with distinct Dps capsules, as depicted in Figure 1.11; this potential inverse effect would guarantee alteration of the tagged protein's native location and/or interactions. For this reason, the DPS_{12} construct would be the most ideal tag, but due to its large size and the linkage of natively separate monomeric subunits into one larger unit, expression proved to be not possible.

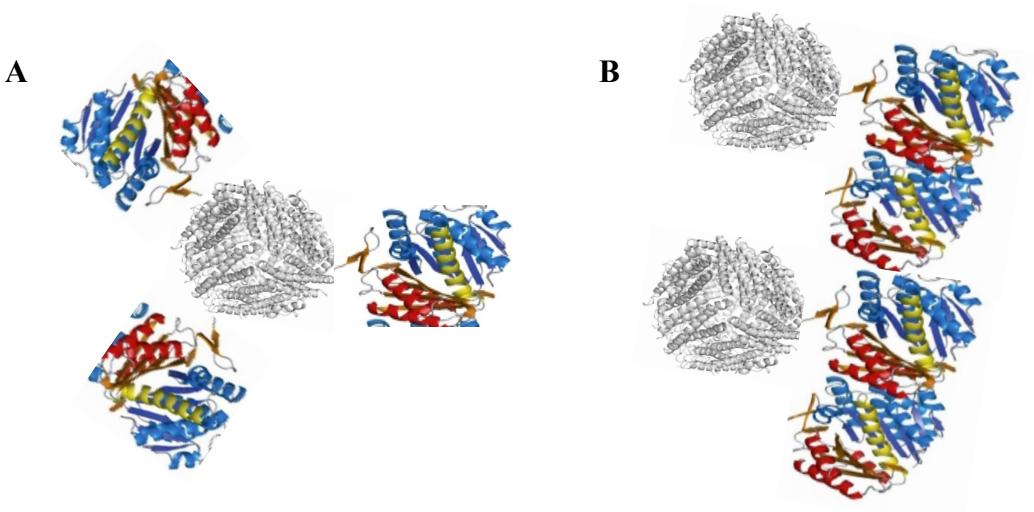

Figure 1.11 Two potential scenarios of capsule-based tag configurations. A) The capsule (grey), acting as a tag, pulls the tagged protein (multi-colored) out of its native environment in order to form the capsule. B) The capsule is able to form on the tagged protein in its native state, a filament.

In an effort to compromise between fewer subunits necessary for full capsule formation and the larger molecular weight of the protein needing to be expressed, five to seven monomer units were linked together and expressed as DPS_5, DPS_6 and DPS_7. In theory, combinations of DPS_5 and DPS_7 or two DPS_6 constructs would be able to form a full 12-mer capsule while balancing protein size and number of units required for assembly. Unfortunately, these intermediate unit numbers also had problems. Protein expression was evident by comparison of pre- and post-lysis samples via SDS-PAGE; however, purification was not possible. It was speculated that the affinity tag was not accessible due to either misfolding that occurred within one of these larger units or an unexpected configuration of the capsule that was formed. Additionally, in these larger, tethered subunits, if intact capsules did exist, they were no longer resistant to heat and precipitated with the other proteins in the lysate. A complete summary of the expression and purification results of all values of x attempted for DPS_x is listed Table 1.4.

Table 1.4 Summary of the various values of x in the DPS_x conjugates investigated for recombinant expression, purification ease, capsule integrity and therefore potential use as a genetically encodable tag. (√) = recombinant expression was verified, but construct could not be purified.

Number of linked subunits	Recombinant expression	Viable as tag
1	√	X
2	√	√
3	√	X
5	(√)	X
6	(√)	X
7	(√)	X
12	X	X

Finally, an alternative approach was devised in order to potentially circumvent the above-described problems (too many subunits required for capsule formation, too large of an individual chimera's molecular weight, too many subunits linked together resulting in compromised capsule integrity) with each previously attempted combination. This system was imagined to combine either DPS_2 or DPS_3 with the necessary number of "mutant" Dps monomers to fill in the remainder of the capsules. A schematic of how this approach was envisioned is displayed in Figure 1.12. There were two potential options for monomer mutations: one that we designed as a dimer and possessed several mutations described by Chiancone et al

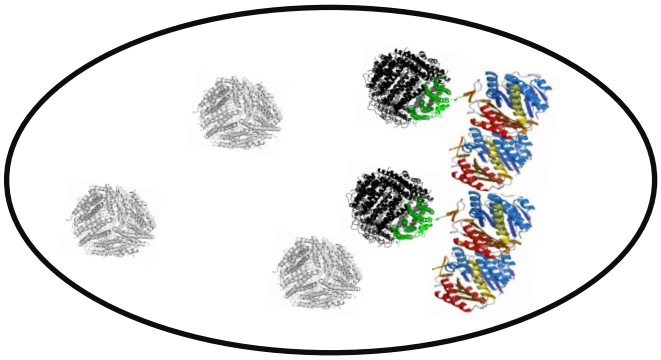

Figure 1.12 Combination of mineralizing (green) and non-mineralizing (black/grey) Dps components for a new tagging approach. If non-mineralizing mutants were highly over-expressed in comparison, they would be readily available to fill in the remainder of the capsule space, allowing for the fully assembled 12-mer necessary for iron oxide core formation without resulting in the scenario depicted in Figure 1.11A.

(Figure 1.13A) that disrupted both the hydrophilic pore (D121N, D126N and D130N) and the ferroxidase site (H31G, H43G and D58A),[40, 41] and a second monomer mutant that we received from Dr. Trevor Douglas' laboratory at Montana State University (Figure 1.13B). The Douglas mutant only had two amino acid mutations, both in the ferroxidase site (H31G and H43G). In our laboratory, these two mutants were termed C. DPS_2 and D. DPS, respectively.

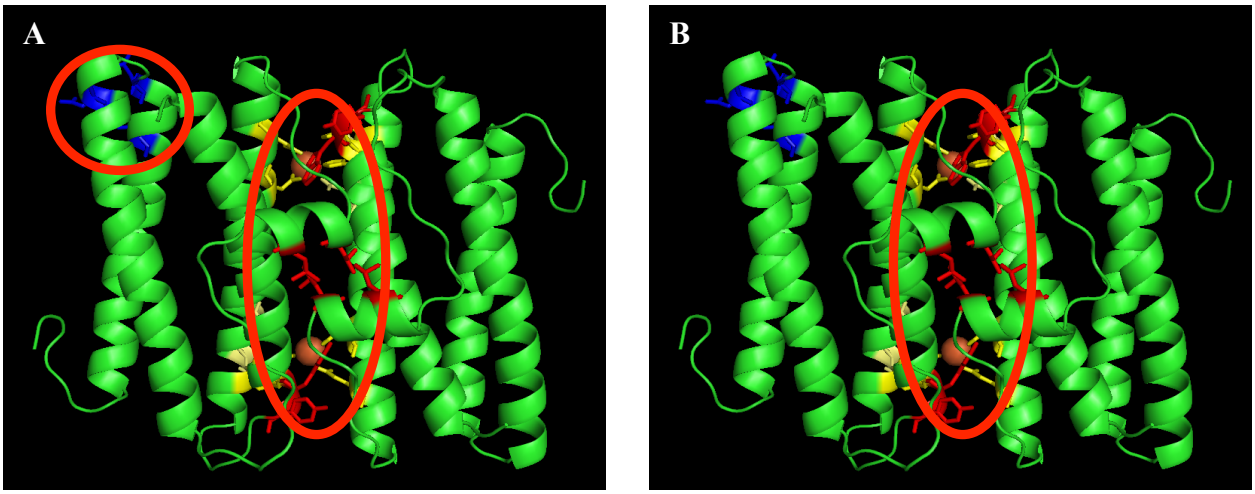

Figure 1.13 Illustration of mutation locations in C. DPS_2 and D. DPS. A) Mutations in both the hydrophilic pore and ferroxidase sites as described by Chiancone et al. The following six mutations were made: H31G, H43G, D58A, D121N, D126N and D130N. B) Mutations in only the ferroxidase sites as received from Dr. Trevor Douglas's laboratory at Montana State University. The mutations were H31G and H43G only.

It was theorized that by combining a low expression level of an intact DPS_2 or DPS_3 and an over-expressed, in comparison, mutant Dps construct, a full 12-mer capsule could be formed that included only one DPS_2 or DPS_3. In this situation, the DPS_2 or DPS_3 could act as the iron-oxidizing component, with its intact ferroxidase site between two monomers, and the other mutant Dps units would simply provide the remainder of the capsule structure for ferric iron storage. While both of the linked constructs, DPS_2 and DPS_3, were successfully over-expressed and purified individually, there was TEM evidence (Figure 1.14) that the DPS_3 format disrupted complete capsule formation in a portion of the total population. This is most likely due to the length of the linker; by rough measurements in PyMol, two different distances were observed, a

shorter one between the dimeric subunits and a longer one from the dimer to a third monomer. The linker could potentially only span the shorter distance to allow for dimer formation, but then not provide enough length to span the longer distance necessary for the addition of a third monomer. As a result, all following experiments were completed only with DPS_2 and each of the mutant forms of Dps.

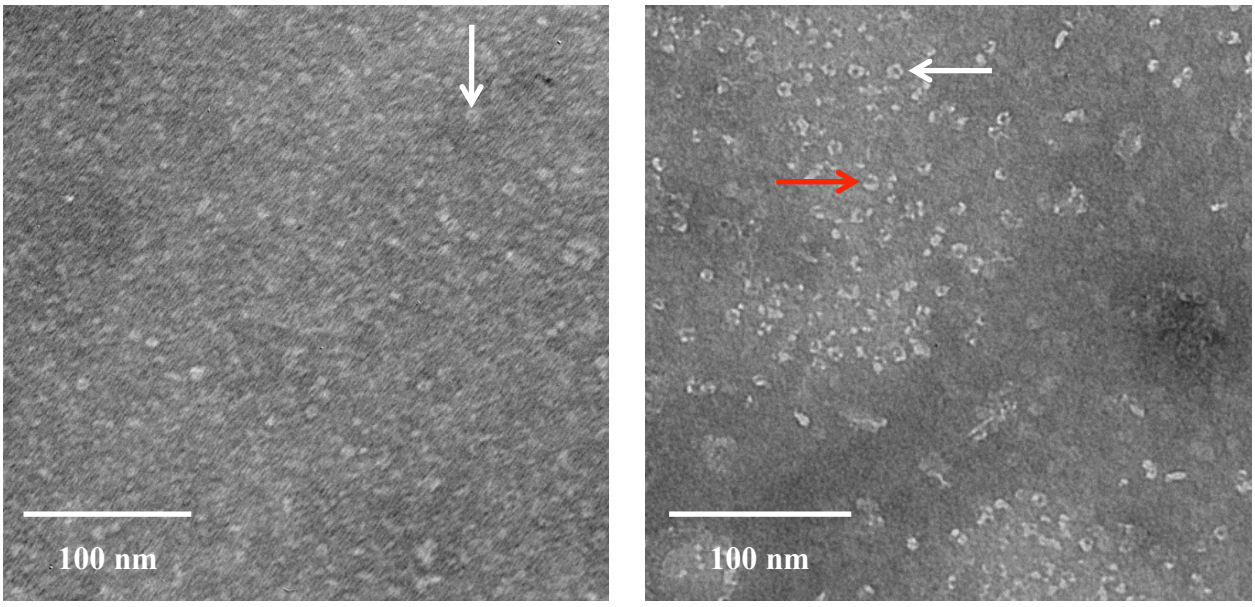

Figure 1.14 Representative stained TEM images for DPS_2 (left panel) and DPS_3 (right panel). The white arrows in both panels indicate fully formed capsules. However, the red arrow points to a partial capsule, a common observation in images for Dps constructs where $x \geq 3$.

Each gene was placed into its own plasmid, as sketched in Figure 1.15, to alter either expression inducement control or expression levels. For the combination of DPS_2 with C. DPS_2, pCOLADuet-1 and pBAD28 were used, which are IPTG and arabinose-inducible, respectively. In the second system, DPS_2 and D. DPS were both under IPTG inducer control in pET15b and pET30, in that order. In this case, however, the hypothesis was that the difference in expression levels natively occurring in each of these plasmids would be enough to differentially express DPS_2 versus D. DPS. The co-expression and purification of both components of the two systems were successful, and full capsule formation continued to be visible via TEM.

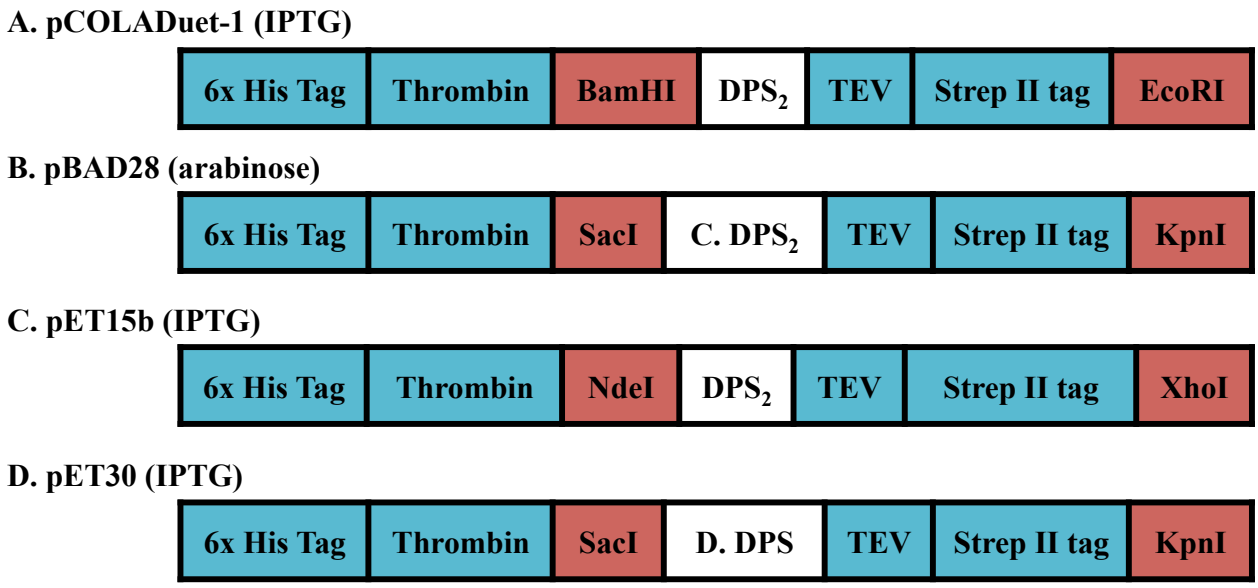

Figure 1.15 Gene inserts of two combinations of DPS_2 with non-mineralizing mutants. In the first combination, A & B, induction by two different molecules, IPTG vs. arabinose, allows for differential control. The plasmids of the second pair (C & D) are both induced by the addition of IPTG; however, pET30 is inherently a higher expressing plasmid than pET15b, resulting in differential expression of the contained plasmids.

1.3 Genetically encodable tag applications

1.3.1 Switching to peptides instead of protein chimeras for tag

After the development of two potential genetically encodable tag systems, the ability to apply these tags to actual biological scenarios is necessary. The simplest format in which to do this is to pick a biomolecule with a repeating and/or assembly-based structure for initial tagging *in vitro*. In this situation, the tag would be distinctly visible since it would be present numerous times in a well-defined, repeating pattern caused by the tagged protein of interest's scaffolding. For this, we considered both capsules, such as reusing ferritin, and filamentous proteins like FtsZ or MreB for the tagged species. By tagging each subunit of ferritin, we hypothesized a capsule coated in nanoparticle tags would be clear by TEM. However, the smaller available volume to allow large tags like $FLF(mms6)_2$ to exist and therefore the potential disruption of capsule

formation by these tags was worrisome. For this reason, it was concluded that a protein filament could provide more axial space in which the tags could exist and FtsZ was chosen for our first application.

The second concern, despite the potential increase in freedom of motion provided by a protein filament, was the complexity and size of the bulky protein tags investigated thus far. Other work in the laboratory at the time was focused on several bio-mineralizing peptides; by combining these two avenues, two smaller biomolecules (i.e. peptides) were initially investigated as the first potential demonstration of a genetically encodable tag.

1.3.1.1 Silver mineralization by Ge8

The first peptide, Ge8 (sequence SLKMPHWLHLLP), was originally isolated during a phage display selection for the formation of germania (Ge^0) networks from a germanium precursor ($C_4H_{12}GeO_4$).[42] A fellow member of the Feldheim laboratory pulled this peptide out of the literature as part of a screen for the ability to mediate the formation of inorganic nanoparticles. She discovered that in addition to the Ge^0 activity, Ge8 was also able to mediate the formation of Ag^0 nanoparticles in the presence of HEPES and light. Furthermore, this peptide continued to function when tethered on one end to a surface.[43] Due to all of the above-mentioned properties and features, it was believed that Ge8 would work as a demonstration of an *in vitro* tagging system. Unfortunately, due to the inherent antibacterial properties of silver,[44, 45] a Ge8 genetically encodable tag would likely have limited use in *in vivo* applications. This resulted in the consideration of a second peptide tag, A3, which was capable of mediating the formation of gold, instead of silver, nanoparticles.

1.3.1.2 Gold mineralization by A3

A3 (AYSSGAPPMPPF) is another example of a material-active peptide found via phage display, similarly to Ge8. It was originally isolated for its strong affinity for both silver and gold surfaces.[46] This was further exploited when it was discovered that the peptide not only bound these metal surfaces, but also in the presence of HEPES buffer, A3 facilitated the formation of 10 nm – 20 nm diameter Au^0 nanoparticles, observable by UV-visible spectroscopy and TEM.[47] Previous mutation studies of A3 led to the hypothesis that the tyrosine residue was responsible for its gold reduction activity.[46, 48] However, these experiments were always done in HEPES buffer, and we have found that A3 was actually only capable of forming small Au^0 clusters (6-7 atoms in size) if HEPES was left out of the reaction, again evident by UV-visible spectroscopy. The variation in the observed λ_{max} for these two species, Au^0 nanoparticles versus Au^0 clusters, is compared in Table 1.5.

Table 1.5 Comparison of the change in UV-visible absorbance properties when HEPES is left out of the reduction reaction of Au^{3+} to Au^0 mediated by the peptide A3.

Reaction	λ_{max} (nm)
A3 + $HAuCl_4$ + HEPES	523
A3 + $HAuCl_4$	348

While this phenomenon does not directly aid in the development of A3 as a genetically encodable tag, it has potential interest to the field of gold cluster optics. Numerous small Au^0 clusters (less than 100 atoms) have been discussed in the literature and several are cumulatively presented on the graph in Figure 1.16; in particular, the variation in the excitation and emission wavelengths corresponding to increasing cluster sizes from three atoms to 31 atoms is shown.[49, 50, 51, 52, 53, 54] Wavelength variations are observed due to the changing surface plasmon resonance of the gold clusters as additional atoms are added.[55] The nanocluster formed by A3 fits into this regime

without difficulty, estimated to be approximately 6 atoms by the equation for the line of best fit through the emission data. The maximum absorbance intensity, and therefore the greatest presence of clusters formed, is observed at 1:1 gold precursor to peptide. It is worth noting as well that the cluster size is slightly tunable by pH. An increase in buffer pH from pH 5 to pH 10 removes about two atoms from the cluster, going from an average of 6.9 atoms to 5.3 atoms. The wavelength corresponding to maximum absorbance also varies with the identity of the buffer system, indicating that this could potentially play a role in A3-mediated formation of these nanoclusters as well. Phosphate-buffered saline (1x) was typically used for experiments, however, switching to 200 mM acetate buffer or 1x phosphate buffer still resulted in gold clusters by UV-visible spectroscopy, simply with slightly lower or higher λ_{max} values respectively.

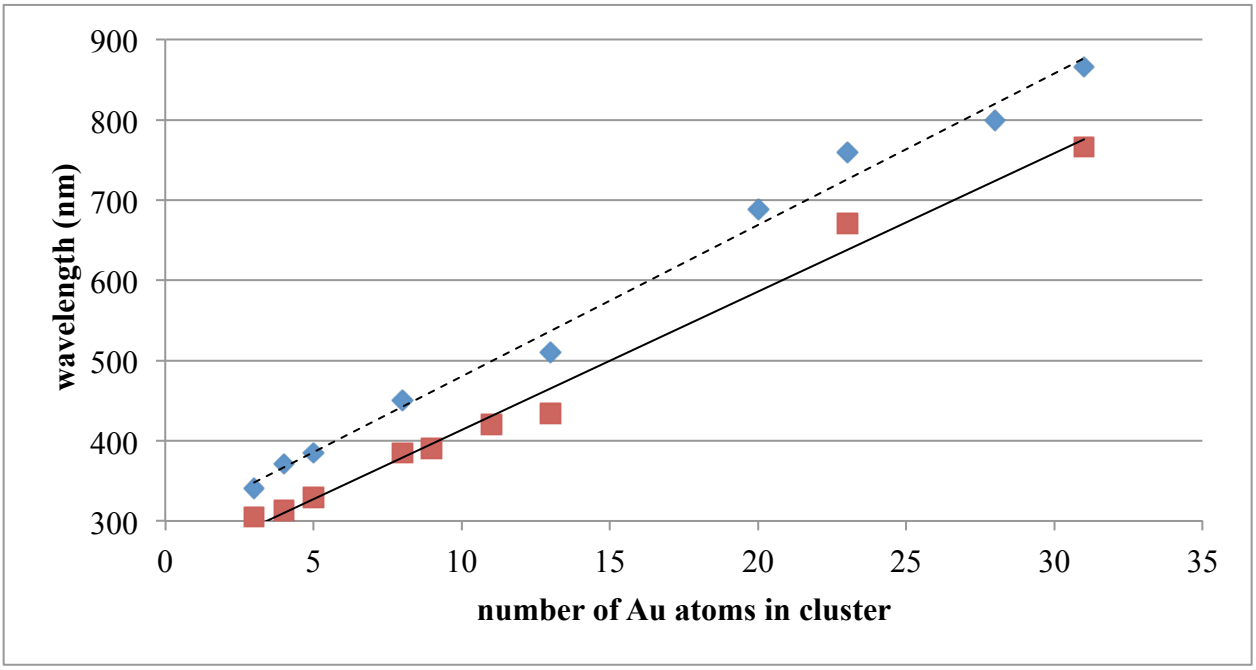

Figure 1.16 Graphical collection of excitation (■) and emission (◆) λ_{max} values as reported throughout the literature. As shown, both sets of data fit a linear equation well; the excitation equation is $y = 18.884x + 291.29$ with an $R^2 = 0.99119$ and the emission equation is $y = 17.252x + 240.9$ with an $R^2 = 0.98803$. (Adapted from refs. 49-54)

Based on these observations, it was hypothesized that the gold reduction from Au^{3+} to Au^0 to form these clusters must be due to three electrons provided by the peptide itself, potentially from the tyrosine and methionine residues present in the sequence.[56, 57, 58] The reduction potential of Au^{3+} to Au^0 is +1.4 V and Au^+ to Au^0 is +1.69 V.[59] Reduction potentials of tyrosine (-0.76 V to -1.00 V),[60, 61, 62] methionine (-1.19 V to -1.75 V),[63, 64] and water under oxidizing conditions (-0.816 V to -1.229 V) would be sufficient in combination to reduce one gold ion to Au^0 per peptide.[65] The peptide must also provide an internal binding and nucleation site, possibly via the methionine or structured proline residues within the sequence.[66, 67] Then upon the addition of HEPES and light to the system, more electrons are available to reduce excess Au^{3+} resulting in the growth of nanoclusters to nanoparticles. HEPES is well reported in the literature to facilitate electron transfer in reduction-oxidation reactions, decreasing necessary potentials,[68, 69] as well as form radicals under oxidizing conditions that could further provide electrons for the reduction of gold.[70] A schematic summarizing the formation of Au^0 nanoparticles by the peptide A3 is presented in Figure 1.17.

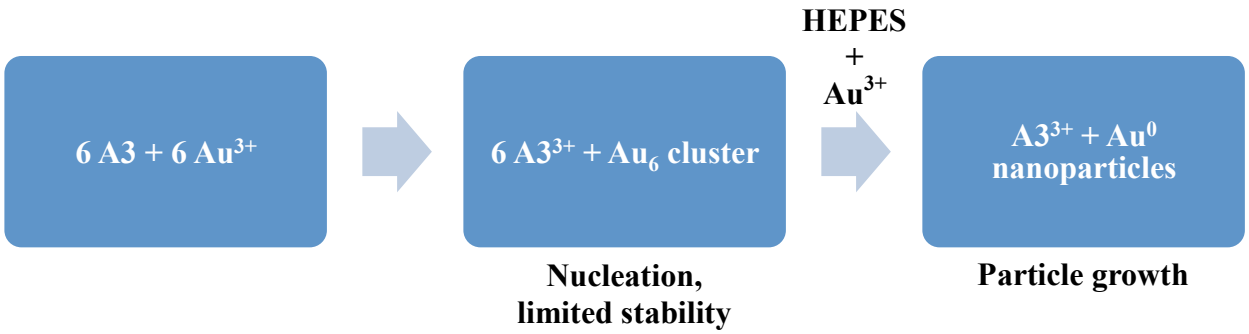

Figure 1.17 Schematic depicting the potential formation of Au^0 nanoclusters and nanoparticles by the peptide A3. Initially, a 1:1 ratio of peptide to precursor Au^{3+} results in the reduction of gold by amino acids in A3 to form six-atom Au^0 clusters with limited stability. Then, upon the addition of HEPES, light and excess Au^{3+}, 10 nm – 20 nm diameter Au^0 nanoparticles grow from the pre-formed nanoclusters. The HEPES buffer both facilitates further electron transfer between gold ions and peptides, as well as directly participates in gold reduction via radical formation (see text).

1.3.2 Tagging application: FtsZ filament labeling

The filamentous protein FtsZ was chosen as the initial *in vitro* scaffold. In *E. coli*, FtsZ is an essential protein that forms a ring around the interior of the cell membrane as part of the earliest steps in cell division.[71, 72] This ring, known as the Z ring, serves as the assembly point for all other cell division proteins and machinery.[73, 74] Most importantly for use in our tag system, FtsZ assembly is dependent on GTP hydrolysis via internal GTPase activity based on Ca^{2+} regulation.[75, 76] In the development of this system, it was hypothesized that this GTP/Ca^{2+} regulation could be exploited for precise control over filament formation, particularly in *in vitro* experiments. Examples of the *in vivo* cellular location of and *in vitro* filament bundles formed by FtsZ are depicted in Figure 1.18. Finally, FtsZ has been engineered into over-expression plasmids previously and successfully labeled with GFP by other laboratories.[38, 39, 40] For our experiments, the GFP label was replaced with the gene for either a trimer of Ge8 peptides or a single A3 peptide in pET15b (Figure 1.19).

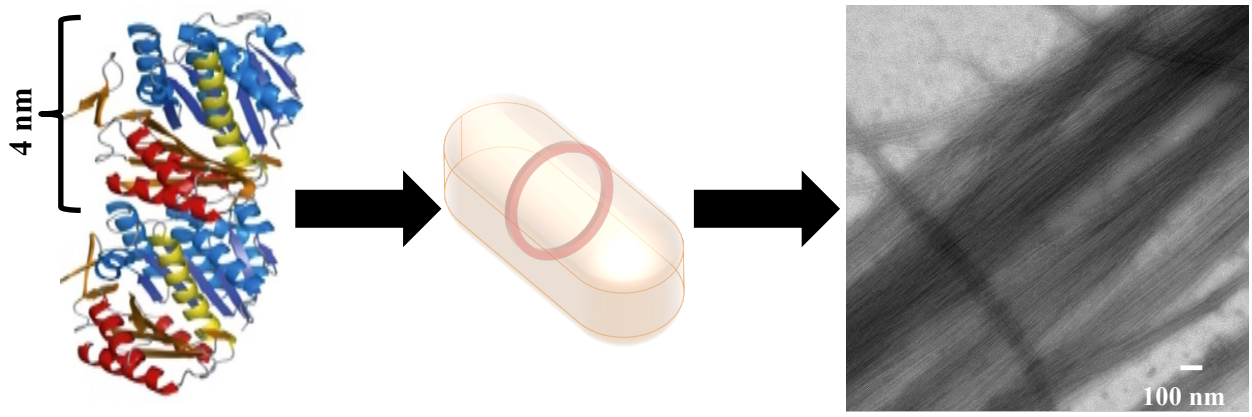

Figure 1.18 Filament assembly of the *E. coli* cell division protein FtsZ. Monomer units, 4 nm in diameter, form the repeating units of the filament, left. *In vivo*, these filaments bundle at the midsection of the cell, just inside the cell membrane, to initiate cell division (shown as a red ring in the illustration of a cell, middle). After over-expression, purification and staining on a TEM grid, bundles of filaments can easily be observed *in vitro*, shown in the right-hand panel.

Figure 1.19 Schematic of tagged FtsZ insert with restriction sites and affinity tags labeled. The "Tag" portion corresponds to either an insert of a Ge8 trimer or A3 monomer. Plasmids were digested with the SpeI restriction enzyme to obtain FtsZ only for controls.

Thus far, both ftsZ-$(Ge8)_3$ and ftsZ-A3 conjugates have been successfully over-expressed and purified via a glycerol lysis specific for membrane-associated, filamentous proteins followed by affinity columns. As both stabilizing the filaments long enough to be viewed by TEM and having them survive the conditions necessary for particle formation are difficult, extensive troubleshooting and manipulation of the system and its conditions were required. More specifically, ftsZ-A3 and the conditions necessary for Au^0 nanoparticle formation proved to fully disrupt filament assembly. Therefore, all results presented are focused on the ftsZ-$(Ge8)_3$ construct.

1.3.3 TEM of nanoparticles formed on filaments

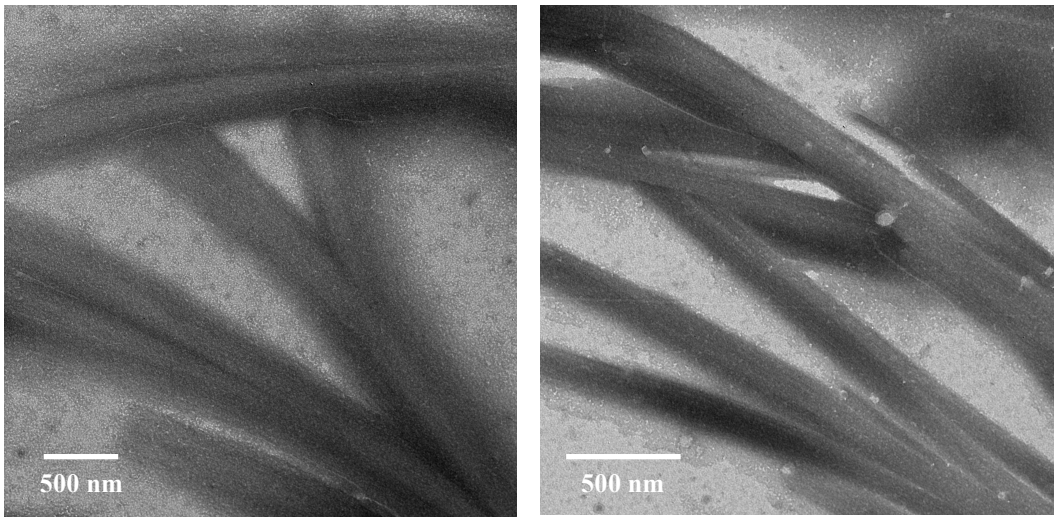

Figure 1.20 Representative stained TEM images of assembled FtsZ only (left panel) and the ftsZ-$(Ge8)_3$ conjugate (right panel). As depicted, the presence of a Ge8 trimer on each FtsZ unit does not inhibit the formation of fully assembled, lengthy bundles of filaments.

As mentioned, ftsZ-$(Ge8)_3$ was the more successful demonstration of a tagged system. First, it was determined that the addition of $Ge8_3$ to the C-terminal end of FtsZ did not prevent filament assembly, as shown in Figure 1.20. Once filament assembly was observed, the filaments were incubated with Ag^+ and HEPES in light to allow silver nanoparticles to form. While this step often partially disrupted assembled filaments, resulting in much shorter segments viewed via TEM, evidence was seen that some FtsZ segments with Ge8 attached could be imaged with formed nanoparticles (Figure 1.21).

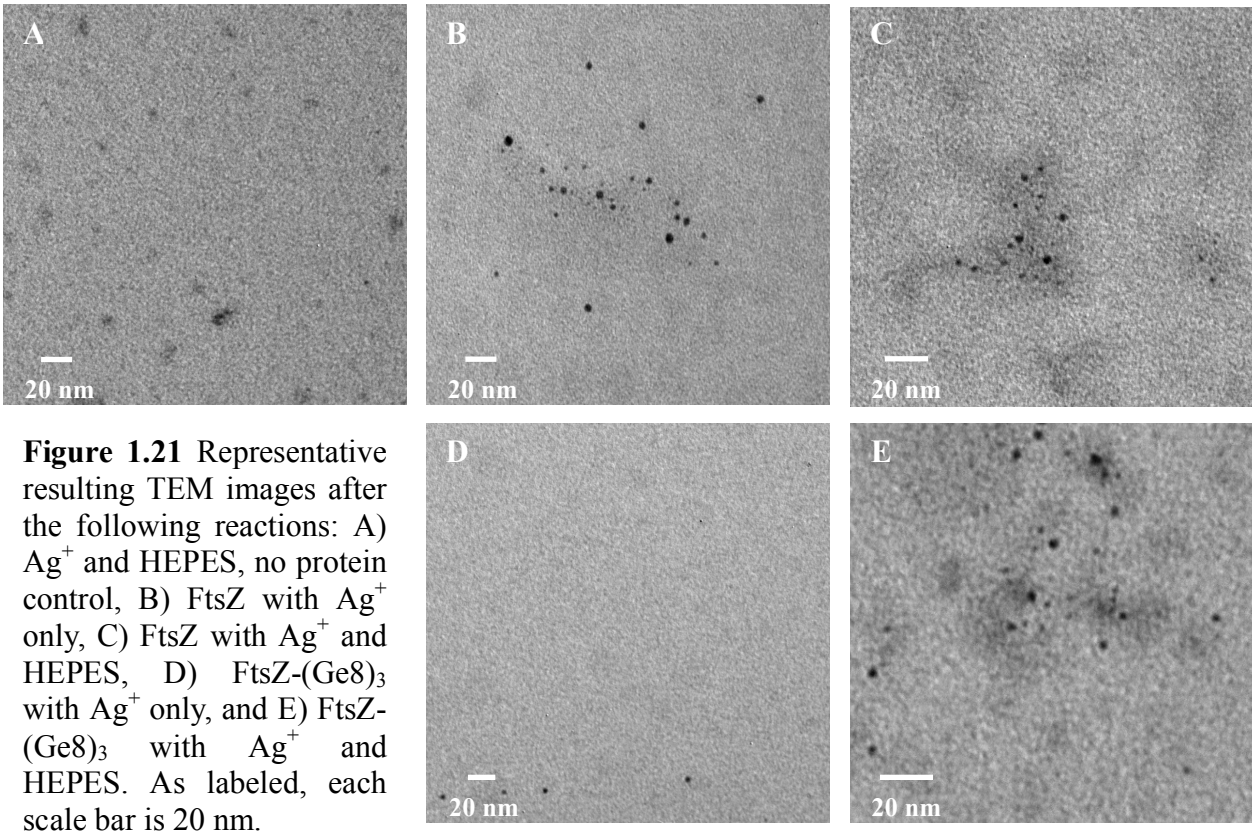

Figure 1.21 Representative resulting TEM images after the following reactions: A) Ag^+ and HEPES, no protein control, B) FtsZ with Ag^+ only, C) FtsZ with Ag^+ and HEPES, D) FtsZ-$(Ge8)_3$ with Ag^+ only, and E) FtsZ-$(Ge8)_3$ with Ag^+ and HEPES. As labeled, each scale bar is 20 nm.

In particular, these were identified by strings of nanoparticles on the copper grids spaced an average of 6.3 nm apart, with a majority of the measurements falling between 3 nm – 5 nm (37.5%) or between 7 nm – 9 nm (31.3%). Due to the size of an FtsZ protein, the repeating assembly of the filament, and the identical location of each tag on each segment, a distance of 4 nm between each nanoparticle was expected (refer back to Figure 1.18). The trend that appeared

in these measurements was that either every or every other FtsZ unit was being labeled by a $Ge8_3$-associated silver nanoparticle, resulting in the measurements clustering around both 4 nm and 8 nm (see Figure 1.22).

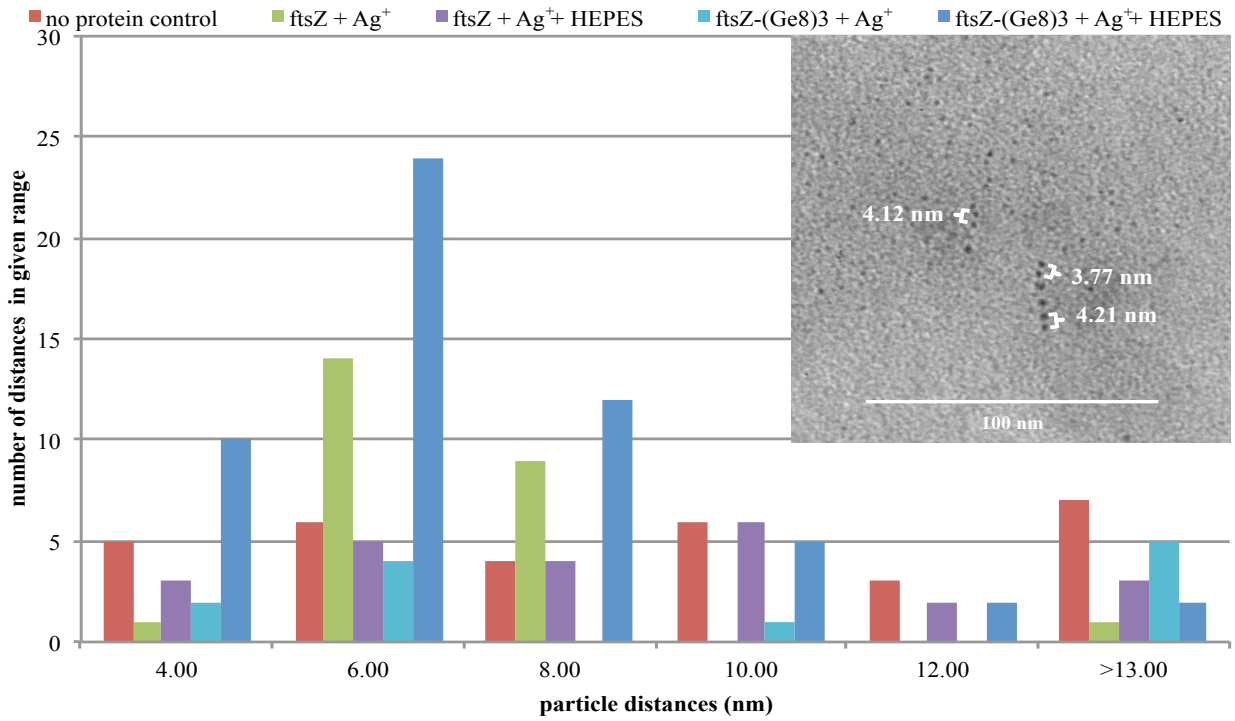

Figure 1.22 Collection of nanoparticle distance measurements from numerous TEM images. As indicated by the legend above the graph, the five sample types are the no protein control containing only Ag^+ and HEPES (red bars), FtsZ with Ag^+ only (green), FtsZ with Ag^+ and HEPES (purple), ftsZ-$(Ge8)_3$ with Ag^+ only (cyan) and ftsZ-$(Ge8)_3$ with Ag^+ and HEPES (blue). The inset provides an example TEM image of ftsZ-$(Ge8)_3$ with Ag^+ and HEPES from which distances were taken. All measurements were done in ImageJ software

Unfortunately, however, examples of nanoparticles presumed to be on FtsZ filaments were also observed in controls when only FtsZ and Ag^+ were present. While this occurred much less often (50% fewer corresponding measurements, see green and cyan bars in Figure 1.22), this does indicate that in the presence of FtsZ, Ag^0 was formed without $Ge8_3$ or HEPES. Due to this observation, it has been concluded that FtsZ most likely played a role in the nanoparticles formation and our tag was not necessary for this system to produce silver nanoparticles.

1.4 Conclusions and future outlooks

The long-term goal of this project was to build a library of genetically encodable tags that would provide unique electron density for use in electron tomography. Regrettably, due to the completion of funding and collaborations, this has not yet occurred in our laboratory. However, several engineered biomolecules have been developed or investigated further for their abilities to mediate the formation of metal and metal oxide nanoparticles. Meanwhile, other laboratories have begun to employ a similar tagging approach, also using a ferritin-based tag, with great success.[77]

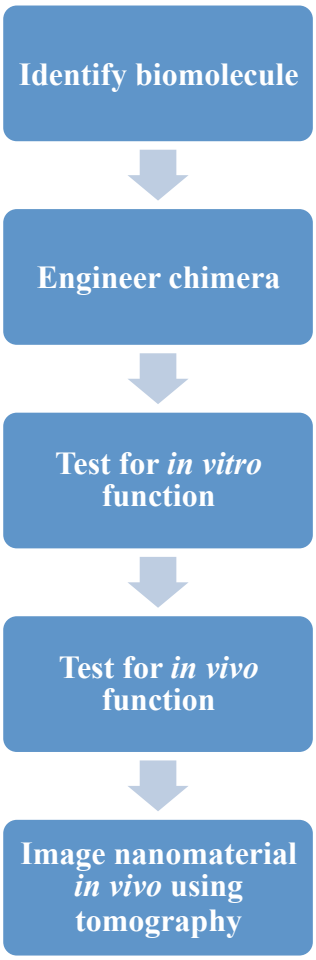

Figure 1.23 Flowchart of project goals.

While our tagging ideas have not been demonstrated in an *in vivo* application, the work presented in this chapter has made significant progress in the development and understanding of numerous biomolecules that could have future use as tags for electron tomography. Based on the outline of the project goals, presented as a flowchart in Figure 1.23, several biomolecules have been identified to be capable of mediating the formation of differing nanoparticles and were engineered into chimeras to exploit specific functions and roles. The resulting nanoparticles in each of these systems were also observed and investigated *in vitro*.

The first iron oxide system presented – FLF$(mms6)_2$, FLF and $(mms6)_2$ – has successfully been expressed, purified, and associated iron has been confirmed. Via TEM images of FLF$(mms6)_2$, it was determined that this protein chimera mediated the formation of approximately 6.8 nm nanoparticles most likely of the composition α-

FeOOH (based on electron diffraction measurements). When broken into individual components, both the size and structure of the nanoparticles was altered; FLF resulted in nanoparticles with an approximate diameter of 4 nm, whereas $(mms6)_2$ yielded an average size larger by a factor of two. In both of these cases, the iron oxide nanoparticles most closely matched d-spacings for γ-Fe_2O_3, again by electron diffraction. The iron found in all three of these nanoparticles was scavenged from the cells or media, as no additional iron was added during cell growth or protein expression. It is of interest to characterize a greater number of nanoparticles observed by TEM with EDS or electron energy loss spectroscopy (EELS) to more confidently report the iron oxide phase of each. Finally, when iron supplementation was provided, the resulting nanoparticles from all three constructs were two to four times smaller and more monodispersed than the original nanoparticles. It is hypothesized that this observation may result from all proteins in solution being exposed to all available iron at the same time, whereas during over-expression, the first proteins synthesized immediately scavenged the scarce amount of iron present in the growth media. In all cases, it is notable that the engineered constructs are able to out-compete the precipitation of insoluble ferric iron to form iron oxide nanoparticles of discrete sizes and compositions.

The Dps constructs developed and investigated seemed to be unable to scavenge as much iron from its environment and so while capsules formed, they tended to be unfilled or only partially filled. Two monomeric units were successfully linked together via a carefully chosen linker to form a dimer (DPS_2). This construct behaved like the native monomer in several aspects that were monitored – expression and purification, as well as capsule formation (evaluated by resistance to heat) and lack of iron by TEM. While numerous larger constructs were designed, including DPS_3, DPS_5, DPS_6, DPS_7 and DPS_{12}, two issues arose. When the construct grew too

large in molecular size (DPS_5 or greater), expression and/or purification proved to be extremely difficult. With DPS_3, expression and purification were successful but the linker length was insufficient to allow for proper capsule formation, resulting in incorrectly formed and unstable capsules. In order to make the system more feasible, the preliminary development of a DPS_2 tag in combination with a Dps mutant has occurred. This situation would allow the semi-native dimer to act as the mineralizing tag component, whereas the over-expressed (in comparison), non-mineralizing mutant would comprise the rest of the capsule, providing iron oxide compartmentalization only.

Finally, with several examples of potential protein genetically encodable tags developed, the cell division, filamentous protein FtsZ was chosen as a proof-of-concept tagging scaffold. The protein filament is made up of repeating monomer units, each 4 nm in length. Thus far, two peptides constructs were employed for tag demonstration, a trimer of Ge8 peptides (ftsZ-$(Ge8)_3$) and a single A3 peptide construct (ftsZ-A3). It was decided that a tagging system with the significantly smaller bio-mineralizing peptides would be a more realistic starting point, instead of using the larger and much more complex ferritin- or Dps-based constructs. Previous work in the laboratory led to the further investigation of peptides A3 and Ge8 for this purpose.

The gold-mineralizing peptide A3 had been shown to mediate the formation of 10 nm – 20 nm Au^0 nanoparticles in the presence of HEPES.[46] In this publication, it was suggested that the tyrosine residue in the peptide was responsible for gold reduction and nanoparticle formation. However, upon further investigation as presented here, the HEPES buffer plays a much larger role in this reaction, presumably as both a facilitator of electron transfer and reducing agent, since it is readily oxidized in water with light. It was observed that Au^{3+} added to A3 only was reduced in a 1:1 ratio to form approximately six-atom Au^0 nanoclusters. This reduction activity

is most likely due to the complementary redox potentials of the amino acid residues tyrosine or methionine. These clusters were then grown to the 10 nm – 20 nm nanoparticles described upon the addition of HEPES and excess Au^{3+} in light, where the presence of both A3 peptides and HEPES allowed further reduction of the supplementary gold.

While the conditions necessary for Au^0 nanoparticle formation entirely destroyed filament integrity in ftsZ-A3, the ftsZ-$(Ge8)_3$ construct yielded Ag^0 nanoparticles in a filament-based pattern approximately either 4 nm or 8 nm apart as observed via TEM, indicating nanoparticle formation was occurring on every or every other subunit. Unfortunately, FtsZ seemed to also be capable of mediating Ag^0 nanoparticle formation on its own and so this construct cannot be carried forward further in this application. Any use of the biomolecules discussed in a tagging system relies upon a demonstration of its function *in vivo*, which has not yet been performed. However, a further understanding of the way in which biomolecules may mediate the formation of specific nanoparticles has been developed.

1.5 Experimental

1.5.1 Plasmid engineering

Gene sequences for bacterioferritin, Mms6 and Dps were obtained from an *E. coli* protein database. The desired portions of each of these were inserted into the cloning and sequencing region of pET15b, pET30, pBAD28[78, 79] or pCOLADuet-1 vectors[80]. Specifically, the gene inserts were placed between XhoI and NdeI restriction sites to allow for use of the native 6x His tag to be included as part of the expressed when available. Additionally, this placement also provided induction control, either by IPTG or arabinose depending on the identity of the plasmid. Following each gene insert, which results in expression on the protein C-terminus, the codons for a TEV protease sequence followed by the Strep II affinity tag were included to aid in

purification. TEV was added for removal of the Strep II tag if it became necessary. Finally, in some cases, restriction sites SpeI and NsiI were placed on both sides of individual portions of the conjugate in order to remove specific pieces. BioBasic, Inc. performed gene synthesis and sequencing.

When truncates of the plasmids were desired, digestion and ligation occurred according to the literature of each restriction or ligation enzyme. In brief, 5 μg of plasmid DNA was incubated in 1x REact buffer (Invitrogen) with 10 U of the appropriate restriction enzyme for 2 hours at 37ºC. The digestion reaction was then directly combined with 2000 units of T4 ligase (NEB) and 1x T4 DNA ligase reaction buffer (NEB) for 12 hours at 16ºC. Enzyme deactivation was done at 65ºC for 10 minutes, followed by storage at 4ºC until transformation was performed. For plasmid amplification, a Maxi-prep kit (Invitrogen) was employed exactly as described in its manual. All DNA quantitation was determined by measurement of the OD_{260}.

1.5.2 Transformation, protein expression and induction

Plasmids from BioBasic, Inc. or after ligation were transformed into chemically competent BL21 pLysS DE3 *E. coli* following the recommended Stratagene procedure (protocol #230240-12). These cells are engineered to be chloramphenicol resistant and each plasmid provided a second antibiotic resistance, resulting in the presence of double resistance to strongly confirm successful transformation. Inductions were allowed to proceed from two to four hours using either 1 mM IPTG or 1 mM arabinose.

1.5.3 Protein purification and quantitation

After induction was complete, cultures were centrifuged at 8,000x g for 5 minutes to form a cell pellet, media was decanted and the remaining pellets were frozen at -20ºC overnight. Most proteins were then taken through the B-Per Lysis Kit (Thermo) to chemically lyse the cells.

In the cases of specifically troublesome (aka membrane-associated) proteins, pellets were resuspended in a glycerol-based lysis buffer – 40 mM Tris pH 8, 125 mM NaCl, 1 mM $Mg(NO_3)_2$ and 10% glycerol – then mechanically lysed via 3-5 freeze/thaw cycles in liquid nitrogen. Cell debris was removed via centrifugation at 16,100x g for 5 minutes. Finally, the lysate was purified through various methods, requiring either one or several in combination. Most conjugates were purified via Strep II affinity columns (all $FLF(mms6)_2$ variations, DPS_2, ftsZ and ftsZ-A3). The purification procedure was followed exactly as published for the resin, except we excluded EDTA from all buffers. If the Strep II tag was unavailable, 6x His resin was employed (ftsZ-$(Ge8)_3$). Finally, after either affinity column, further purification was often necessary by a quarternary amine (Q) column. Dps is heat resistant to 70ºC; this feature was used regularly to clean up lysate before affinity column purification, as well as determine the structural integrity of potential capsules formed by our engineered, linked Dps variations.[35]

All column fractions were analyzed by SDS-PAGE for purity and correct molecular weight. Proteins were then concentrated on molecular weight cut-off filters (Amicon) and dialyzed into water or 100 mM Tris depending on later applications. Once concentrated in the desired buffer, protein concentrations were determined by a Bradford assay. In brief, 1x Bradford reagent (Bio-Rad) was combined with varying concentrations of a BSA protein standard (typically 0.1 mg/mL to 1 mg/mL) to create a calibration curve. Triplicate dilutions of purified protein were also combined with 1x Bradford. OD_{595} values were measured for all solutions and protein concentrations could be calculated from the equation for the line of best fit for the calibration curve.

1.5.4 FtsZ conjugate assembly and nanoparticle formation reactions

For experiments involving the filamentous protein FtsZ, two reactions for 1) assembly of the filament and 2) formation of metal nanoparticles were necessary. Filament assembly was carried out by incubating the purified protein in the presence of 100 mM MES buffer, 1 mM EDTA, 10 mM $CaCl_2$, 5 mM $Mg(NO_3)_2$ and 1 mM GTP. This reaction was placed on ice for 10 minutes followed by 10 minutes at 37ºC. A 20 μL aliquot of this protein reaction was dropped onto a TEM grid for 2 minutes, wicked away, and then washed with water for 30 seconds. To proceed with nanoparticle formation, these grids were inverted onto another 20 μL drop containing 1 mM $AgNO_3$ with or without 10 mM HEPES, depending on the reaction. This entire set up was placed into a moist petri dish and allowed to react for two hours, before washing with water and drying.

1.5.5 ICP-OES

One milliliter of media, buffer or purified protein sample was submitted for analysis by ICP-OES in the Laboratory for Environmental and Geological Studies (LEGS) in the Department of Geological Sciences on campus. The instrument used was an ARL 3410+ inductively coupled optical emission spectrometer.

1.5.6 Transmission electron microscopy

Electron microscopy was performed using a Phillips CM100 instrument with an accelerating voltage of 80 kV and a 2k x 2k AMT CCD camera. In general, 20 μL drop of protein and/or nanoparticle solution was placed onto a glow-discharged, 300 mesh copper, carbon-coated TEM grid (EM Sciences). This drop was allowed to incubate for two minutes before wicking. The grid was then washed with a 20 μL drop of Milli-Q H_2O for 30 seconds.

When desired, protein staining was completed via the addition of NanoVan, a vanadium based stain from Nanoprobes, Inc., for 10 seconds followed by wicking and a thorough drying period.

1.5.7 Electron diffraction

Electron diffraction patterns were obtained on the above TEM instrument, with a higher accelerating voltage (100 kV). Based on the setup of the electron beam and the camera, the nominal camera length was determined to be 175 mm. All experimental d-spacings were compared to known values for NaCl, Ag, and various phases of Fe_3O_4, Fe_2O_3, FeOOH and FeO.

1.5.8 DF-STEM with EDS

Grids were prepared as previously described and analyzed through the Materials Characterization Laboratory at Pennsylvania State University using a scanning transmission electron microscope with both dark field and energy dispersive X-ray spectroscopy capabilities.

1.6 References

[1] Matsunaga, T.; Sakaguchi, T.; Tadakoro, F. *Appl. Microbiol. Biotechnol*. **1991**, *35 (5)*, 651-655.
[2] Aizenberg, J.; Tkachenko, A.; Weiner, S.; Addadi, L.; Hendler, G. *Nature*, **2001**, *412 (6849)*, 819-822.
[3] Goreau, T.F. *Annals of the New York Academy of Sciences*, **1963**, *109*, 127.167.
[4] Currey, J.D. Bones: Structure and Mechanics; Princeton University Press: Princeton, New Jersey, 2006.
[5] Giepmans, B.N.G. *Histochem. Cell. Biol.* **2008**, *130*, 211-217.
[6] Davis, I. *Biochemical Society Transactions*, **2009**, *37 (5)*, 1042-1044.
[7] Heintzmann, R.; Ficz, G. *Briefings in Functional Genomics and Proteomics*, **2006**, *5 (4)*, 289-301.
[8] Pawley, J.B. Handbook of Biological Confocal Microscopy (3rd Ed.); Springer: New York, NY, 2006.
[9] Klar, T.; Jakobs, S.; Dyba, M.; Egnar, A.; Hell, S.W. *PNAS*, **2000**, *97 (15)*, 8206-8210.
[10] Gustafsson, M. *Journal of microscopy*, **2000**, *198 (January)*, 82-87.
[11] Betzig, E. *Opt. Lett.* **1995**, *20*, 237-239.
[12] Betzig, E.; Patterson, G.H.; Sougrat, R.; Lindwasser, O.W.; Olenych, S.; Bonifacino, J.S.; Davidson, M.W.; Lippincott-Schwartz, J.; Hess, H.F. *Science*, **2006**, *313 (September)*, 1642-1645.
[13] Jensen, G.J.; Briegel, A. *Curr. Op. Microbiol.* **2007**, *17*, 260-267.
[14] Li, Z.; Jensen, G.J. *Curr. Op. Microbiol.* **2009**, *12*, 333-340.
[15] Komeili, A.; Li, Z.; Newman, D.K.; Jensen, G.J. *Science*, **2006**, *311 (5758)*, 242-245.
[16] Stumm, W.; Lee, G.F. *Aquatic Sciences*. **1960**, 295-320.
[17] U.S. Geological Survey. Chemistry of Iron in Natural Water; Government Printing Office: Washington, D.C., 1962.
[18] Flynn, C.M. Jr. *Chemical Reviews*. **1984**, 31-41.
[19] Jambor, J.L.; Dutrizac, J.E. *Chemical Reviews*. **1998**, 2549-2587.
[20] Schwertmann, U.; Friedl, J.; Stanjek, H. *Journal of Colloid and Interface Science*, **1999,** *223*, 215-223.
[21] Jolivet, J.-P.; Chanéac, C.; Tronc, E. *Chem. Comm.* **2003**, 481-487.
[22] California State University, Dominguez Hills. Selected Solubility Products and Formation Constants at 25°C. http://www.csudh.edu/oliver/chemdata/data-ksp.htm (accessed April 7, 2015).
[23] Gayer, K.; Woontner, L. *Journal of Physical Chemistry*, **1956**, *57 (13)*, 1-3.
[24] Hem, J.D. *Geological Society of America Bulletin*, **1972**, *February*, 433-450.
[25] Aisen, P.; Enns, C.; Wessling-Resnick, M. *The International Journal of Biochemisty & Cell Biology*, **2001**, *33 (10)*, 940-959.
[26] Braun, V.; Braun, M. *FEBS Letters*, **2002**, *529*, 78-85.
[27] Krewulak, K.; Vogel, H. *Biochimica et Biophysica Acta (BBA)*, **2008**, *1778 (9)*, 1781-1804.
[28] Carrondo, M. *EMBO Journal*, **2003**, *22 (9)*, 1959-1968.
[29] Malone, S.A.; Lewin, A.; Kilic, A.; Svistunenko, D.A.; Cooper, C.E.; Wilson, M.T.; LeBrun, N.E.; Spiro, S.; Moore, G.R. *J. Am. Chem. Soc.* **2004**, *126*, 496-504.

[30] Theil, E.C.; Takagi, H.; Small, G.W.; He, L.; Tipton, A.R.; Danger, D. *Inorganica Chimica Acta*, **2000**, *297 (1-2)*, 242-251.
[31] Kidane, T.; Sauble, E.; Linder, M. *American Journal of Physiology: Cell Physiology*, **2006**, *291 (3)*, C445-C455.
[32] Prozorov, T.; Mallapragada, S.K.; Narasimhan, B.; Wang, L.; Palo, P.; Nilsen-Hamilton, M.; Williams, T.J.; Bazylinski, D.A.; Prozorov, R.; Canfield, P.C. *Adv. Func. Mater.* **2007**, *17 (6)*, 951-957.
[33] Arakaki, A.; Masuda, F.; Amemiya, Y.; Tanaka, T.; Matsunaga, T. *Journal of Colloid and Interface Science*, **2010**, *343*, 65-70.
[34] Amptek, Inc. What is XRF?. http://www.amptek.com/xrf/ (Accessed April 8, 2015).
[35] Amptek, Inc. Periodic Table and X-Ray Emission Line Lookup Chart. http://www.amptek.com/periodic-table-and-x-ray-emission-line-lookup-chart/ (Accessed April 8, 2015).
[36] *Iron (II) sulfate heptahydrate*; MSDS F7002; Sigma Aldrich: St. Louis, MO, Feb 27, 2015.
[37] Almirón, M.; Link, A.J.; Furlong, D.; Kolter, R. *Genes & Development*, **1992**, *6*, 2646-2654.
[38] Bozzi, M.; Mignogna, G.; Stefanini, S.; Barra, D.; Longhi, C.; Valenti, P.; Chiancone, E. *J. Biol. Chem*. **1997**, *272 (6)*, 3259-3265.
[39] Franceschini, S.; Ceci, P.; Alaleona, F.; Chiancone, E.; Ilari, A; *FEBS*. **2006**, *273*, 4913-4928.
[40] Ilari, A.; Latella, M.C.; Ceci, P.; Ribacchi, F.; Su, M.; Giangiacomo, L.; Stefanini, S.; Chasteen, N.D.; Chiancone, E. *Biochemistry*. **2005**, *44*, 5579-5587.
[41] Ceci, P.; Chiancone, E.; Kasyutich, O.; Bellapadrona, G.; Castelli, L.; Fittipaldi, M.; Gatteschi, D.; Innocenti, C.; Sangregorio, C. *Chem. Eur. J.*, **2010**, *16*, 709-717.
[42] Dickerson, M.B.; Naik, R.R.; Stone, M.O.; Cai, Y.; Sandhage, K.H. *Chem. Comm.* **2004**, 1776-1777.
[43] Carter, C.J.; Ackerson, C.J.; Feldheim, D.L. *ACS Nano*, **2010**, *4 (7)*, 3883-3888.
[44] Panáček, A.; Kvítek, L.; Prucek, R.; Kolář, M.; Večeřová, R.; Pizúrová, N.; Sharma, V.K.; Nevěčná, T.; Zbořil, R. *J. Phys. Chem. B*. **2006**, *110*, 16248-16253.
[45] Marambio-Jones, C.; Hoek, E.M.V. *J. Nanopart. Res.* **2010**, *12*, 1531-1551.
[46] Naik, R.R.; Stringer, S.J.; Agarwal, G.; Jones, S.E.; Stone, M.O. *Nat. Mater.* **2002**, *1 (3)*, 169-172.
[47] Slocik, J.; Stone, M.; Naik, R. *Small*. **2005**, *1 (11)*, 1048-1052.
[48] Slocik, J.; Naik, R.; Stone, M.; Wright, D. *Journal of Materials Chemistry*, **2005**, *15 (7)*, 749-753.
[49] Link, S.; Beeby, A.; FitzGerald, S.; El-Sayad, M.A.; Schaaff, T.G.; Whetten, R.L. *J. Phys. Chem. B*. **2002**, *106*, 3410-3415.
[50] Zheng, J.; Petty, J.T.; Dickson, R.M. *JACS*, **2003**, *125*, 7780-7781.
[51] Tran, M.L.; Zvyagin, A.V.; Plakhotnik, T. *Chem. Comm.* **2006**, 2400-2401.
[52] Xie, J.; Zheng, Y.; Ying, J.Y. *JACS*, **2009**, *131 (3)*, 888-889.
[53] Nijamudheen, A.; Datta, A. *Journal of Molecular Structure: THEOCHEM*. **2010**, *945*, 93-96.
[54] Palmal, S.; Jana, N.R. *WIREs Nanomed. Nanobiotechnol.* **2014**, *6*, 102-110.
[55] Link, S.; El-Sayed, M. A. *Journal of Physical Chemistry B*, **1999**, *103 (40)*, 8410-8426.
[56] Harriman, A. *Journal of Physical Chemistry*, **1987**, *91 (3)*, 6102-6104.
[57] Fecenko, C.; Meyer, T.; Thorp, H. *JACS*, **2006**, *25*, 11020-11021.
[58] Nam, K.; Lee, Y.; Krauland, E. *ACS Nano*, **2008**, *2 (7)*, 1480-1486.
[59] Atkins, P.; de Paula, J. *Elements of Physical Chemistry*, 4th ed.; Oxford University Press: New York, 2005.

[60] Harriman, A. *Journal of Physical Chemistry*, **1987**, *91 (3)*, 6102-6104.
[61] DeFelippis, M.R.; Murthy, C.P.; Faraggi, M.; Klapper, M.H. *Biochemistry*, **1989**, *28 (11)*, 4847-4853.
[62] Barry, B. *Photochemistry and photobiology*, **1993**, *57 (1)*, 179-188.
[63] Milligan, J; Aguilera, J.; Ly, A.; Tran, N.Q.; Hoang, O.; Ward, J.F. *Nucleic Acids Research*, **2003**, *31 (21)*, 6258-6263.
[64] Berges, J.; De Oliveira, P.; Fourre, I.; Houee-Levin, C. *Journal of Physical Chemistry B*, **2012**, *116 (31)*, 9352-9362.
[65] Tinoco, Jr., I.; Sauer, K.; Wang, J.C. *Physical Chemistry: Principles and Applications in Biological Sciences*, 3rd ed.; Prentice Hall: Upper Saddle River, NJ, 1995.
[66] Chen, C.; Rosi, N. *Angewandte Chemie International Edition*, **2010**, *49 (11)*, 1924-1942.
[67] Tan, Y.; Lee, J.; Wang, D. *JACS*, **2010**, *18*, 5677-5686.
[68] Cuculic, V.; Mlakar, M.; Branica, M. *Electroanalysis*, **1998**, *10 (12)*, 852-856.
[69] Baker, C.J.; Mock, N.M.; Roberts, D.P.; Deahl, K.L.; Hapeman, C.J.; Schmidt, W.F.; Kochansky, J. *Free Radical Biology and Medicine*, **2007**, *43 (9)*, 1322-1327.
[70] Grady, J.; Chasteen, N.; Harris, D. *Analytical Biochemistry*, **1988**, *173 (1)*, 111-115.
[71] Buddelmeijer, N.; Beckwith, J. *Current Opinion in Microbiology*, **2002**, *5*, 553-557.
[72] Li, Z.; Trimbler, M.J.; Brun, Y.V.; Jensen, G.J. *The EMBO Journal*, **2007**, *26*, 4694-4708.
[73] Sun, Q.; Margolin, W. *J. Bacteriol*. **1998**, *180 (8)*, 2050-2056.
[74] Anderson, D.E.; Gueiros-Filho, F.J.; Erickson, H.P. *J. Bacteriol.* **2004**, *186 (17)*, 5775-5781.
[75] Yu, X.-C.; Margolin, W. *The EMBO Journal*. **1997**, *16 (17)*, 5455-5463.
[76] Chen, Y.; Erickson, H.P. *J. Biol. Chem.* **2005**, *280*, 22549-22554.
[77] Wang, Q.; Mercogliano, C.P.; Löwe, J. *Structure*, **2011***, 19*, 147-154.
[78] Guzman, L.-M.; Belin, D.; Carson, M.J.; Beckwith, J. *J Bacteriol.* **1995**, *177 (14)*, 4121-4130.
[79] Khlebnikov, A.; Skaug, T.; Keasling, J.D. *Journal of Industrial Microbiology and Biotechnology*, **2002**, *29*, 34-37.
[80] Held, D.; Yaeger, K.; Novy, R. *Novagen: inNovations*, **2004**, *19*, 17-19.

CHAPTER 2[1]

Gold Nanoparticle Antibiotics – Part One

Active conjugate towards *M. smegmatis*

2.1 Introduction & Background

2.1.1 Current antibiotics

The first general class of antibiotics, β-lactams, was introduced in the late 1920s, with the remaining majority in place by 1965. This means that on average, specific antibiotics or classes of antibiotics have been on the market for 70 or more years. Other than β-lactams, the main classes also include aminoglycosides, tetracyclines, chloramphenicols, glycopeptides, oxazolidinones and quinolones, all small molecules that target cell wall synthesis, biosynthesis, cell signaling, etc.[2] While each class potentially targets a different cellular process that results in growth inhibition or cell death, the repeated use of these same antibiotics inevitably leads to the development of bacterial resistance.

In a similar, but more specific situation, *Mycobacterium tuberculosis* (TB) antibiotics are equally old, with most in use since the 1940s-1960s.[3] These antimycobacterials also started with a disadvantage as they typically are much less efficacious and have more severe side effects than antibiotics prescribed for more common infections.[4, 5] A normal TB treatment prescription, if you have a drug susceptible infection, requires a cocktail of four drugs taken twice a day for six months. This regimen becomes even more extensive in the case of resistant strains of TB, in which as many as six antibiotics may be required for up to two years.

2.1.2 Bacterial resistance

The emergence of resistance to multiple antimicrobial agents by pathogenic bacteria has become a significant global public health threat. Drug resistant bacterial infections cause considerable patient mortality and morbidity, and rising antibiotic resistance is seriously threatening the vast medical advancements made possible by antibiotics over the past 70 years.[6] For example, according to the Center for Disease Control, 2 million people each year acquire bacterial infections that are resistant to one or more antibiotics in the United States alone. As a direct result of their infection, 23,000 of these people will die. Methicillin-resistant *Staphylococcus aureus* (MRSA) is responsible for the largest percentage of these infections and has a 13.8% mortality rate. Both enterobacteriaceae (including *E. coli* and *Klebsiella pneumoniae*) and *Pseudomonas aeruginosa* infections have mortality rates of approximately 6.5% due to the prevalence of multidrug-resistant (MDR) strains. Finally, despite the low abundance of TB infections in this country, only about 1,000 infections per year, almost 5% of those people will die from this disease.[7]

Worldwide, TB is second only to HIV/AIDS as the greatest killer due to a single infectious agent. The World Health Organization (WHO) estimated that 8.6 million people were infected and 1.3 million people died in 2012 alone.[8] MDR-TB, which is defined as strains resistant to the two first-line antibiotics isoniazid and rifampin, is present in almost all countries with TB infections, resulting in 450,000 active cases and 170,000 deaths. Furthermore, 10% of all MDR-TB diagnoses are actually extensively-drug resistant (XDR) TB and are additionally resistant to treatment with fluoroquinolones and at least one of the second-line, kanamycin-based injectable TB drugs. Seventy

percent of these people will die within one month of being diagnosed and the survival rate is only 2%.[9] As of September 2013, 92 countries had reported as least one case of XDR-TB, including the United States.[5]

Without developing innovative approaches to combat these multi-drug resistant pathogens, many fields of medicine will be severely affected, including surgery, premature infant care, cancer chemotherapy, care of the critically ill, and transplantation medicine, all of which are feasible only with the existence of effective antibiotic therapy. This situation is so dire that the WHO has identified multi-drug resistant (MDR) bacteria as one of the top three threats to human health, while the infectious disease society has issued a call to action from the biomedical community to deal with the MDR bacterial threat.[10, 11] Of all the potential bacterial threats, the members of the so-called ESKAPE pathogens (*Enterococcus faecium*, *S. aureus*, *Klebsiella pneumoniae*, *Acinetobacter baumannii*, *Pseudomonas aeruginosa*, and Enterobacteriaceae), as well as *M. tuberculosis*, are considered the greatest threat to human health due to the development of multi-drug resistance and therefore diminishing options for treatment.[12, 13]

Resistance can develop via several pathways. These mechanisms include or are related to: 1) genetic resistance, 2) efflux pumps, and 3) enzymes.[14] Prokaryotes spontaneously experience a genetic mutation 0.0033 times per DNA replication, each of which could lead to naturally acquired resistance.[15] Most bacteria also have intrinsic genes that confer antibiotic resistance, called the *mar* (multiple antibiotic resistance) genes. When an antibiotic, disinfectant or organic solvent is present that causes cell stress, growth inhibition or death, *mar* repression is deactivated and transcription of MarA is able to proceed.[16] This gene governs the expression levels of more than sixty

other genes, in majority related to membrane porins and efflux pumps, such as OmpF in *E. coli*, as well as the two-component system SoxS that responds to superoxide cell stress.[17, 18] The most general way for a bacterium to remove antibiotics and therefore become resistant to their action is to alter or over-express efflux pumps in the cell membrane. In this situation, pumps can simply eject the undesired molecule back out of the cell, preventing therapeutic concentrations from building up within the cell.[19, 20] More specifically to certain types and structures of antibiotic classes, mutations in enzymes can become beneficial to the survival of bacteria. In these cases, enzymes can either degrade or alter antibiotics, ultimately rendering the drug inactive.[21, 22] Probably the most famous class of antibiotic-modifying enzymes are β-lactamases, which are usually involved in cell wall synthesis, but can cleave or hydrolyze β-lactam antibiotics such as penicillin and ampicillin.[14]

For *M. tuberculosis*, the cellular mechanism for antibiotic resistance has been well established in many cases.[23] As mentioned, MDR-TB strains are resistant to both isoniazid and rifampin. Isoniazid is a pro-drug that requires enzymatic activation. Mutations in *katG*, *inhA* and *ahpC* result in decreased activity of catalase/peroxidase and two reductases, respectively, which all contribute to activating isoniazid.[20, 24] Similarly, resistance to pyrazinamide, another first-line TB antibiotic, depends upon a mutation in *pncA* and resulting low levels of the enzyme pyrazinamidase, preventing the pro-drug from being activated to pyrazinoic acid.[25] TB becomes resistant to rifampin, which inhibits RNA synthesis, via a genetic mutation in *rpoB* and therefore the β subunit of RNA polymerase.[26, 27] Finally, streptomycin, one of the oldest TB antibiotics that primarily interacts with the 30S ribosomal subunit to disrupt protein synthesis, is

rendered inactive by a mutation in the *rpsL* gene leading to an altered ribosomal S12 protein and recovery of translation.[28]

A summary of the major classes of antibiotics is shown in Table 2.1, including common examples of each class, the year in which the class was developed, what types of infection(s) each generally treats, the known resistance mechanism(s) and when that resistance mechanism was first observed. It is worth drawing attention to the short time period between the development of each type of antibiotic and the discovery of resistance to that type.

Table 2.1 Examples of major antibiotic classes, specific drugs from those classes, corresponding year they were introduced in the clinic, what it was used to treat, the resistance mechanism that has since been discovered and when that resistance was first observed. (Adapted from refs. 13-18)

Class of Antibiotic	Example	Drug Developed	Treatment Uses	Resistance Mechanism	Resistance Developed
β-lactam	Penicillin	1943	Ear, Streptococcal infections	Enzymatic degradation, sequestration	1965
Aminoglycoside	Streptomycin	1944	Gram-negatives	Enzymatic alteration	1947
Tetracycline	Doxycycline	1950	Lyme disease	Efflux pumps	1959
Glycopeptides	Vancomycin	1972	Gram-positives	Cellular modification	1988
Quinolones	Levofloxacin	1996	UTIs, Pneumonia	Cellular modification, efflux pumps	1996
Oxaolidonones	Linezolid	2000	Vancomycin-resistant *S. aureus*	Cellular modification	2001

2.1.3 Gold nanoparticles

Our laboratory sought to develop highly potent nanoparticle antibiotics that are active both *in vitro* and *in vivo* as new therapeutics and anti-resistance agents against the previously mentioned pathogens. It was hypothesized that a nanometer-scale drug such as a nanoparticle would continue to provide large chemical diversity, in comparison to small molecules, while also being resistant to the effects of efflux pumps due to their larger sizes. Furthermore, the easily manipulated, surface monolayer allows the presentation of numerous functional groups at once, providing higher valency and the ability to modify with molecules that can increase circulation lifetimes and decrease mammalian toxicity (as will be discussed).

Nanoparticles exist in numerous sizes, shapes and compositions, ranging from ~ 1 nm to several hundred nanometer diameter spheres, rods, triangles, cubes and hexagons of Au, Ag, Pt, Cu, etc.[29, 30, 31, 32, 33, 34] Gold was specifically chosen for several reasons. First, gold nanoparticles have well-established syntheses that can be simple (i.e. two-step), aqueous and extremely reproducible. In particular, Kornberg and colleagues described one such protocol in *Science* in 2007 to create para-mercaptobenzoic acid (pMBA) capped 2 nm gold nanoparticles of the formula $Au_{144}pMBA_{60}$.[35] The resulting nanoparticles are both water-soluble and small. It was our hypothesis that nanoparticles with a smaller diameter would be able to gain internal access to bacterial cells, possibly reaching more specific targets than larger nanoparticles able to only interact with the membrane and surface-exposed targets.

While methods for other nanoparticle preparations vary widely, there is often less control over precise size and shape, as well as requirements for oxygen-free

environments during synthesis and decreased solubility in water.[20, 21, 23] Due the obvious need for both oxygen and water in biological systems, we were specifically looking for a nanoparticle synthesis that would be stable in the presence of both for our downstream application. Additionally, the pMBA-coated base nanoparticles do not inhibit bacterial growth, providing an inert platform on which to develop antibiotics. The antimicrobial activity of silver has been well established,[25] and the combination of our antibiotic ligand sets on the surface of silver instead of gold could be an interesting future direction to investigate. However, the goal of this project thus far has been to exploit the combinatorial properties of individually inert components (pMBA-coated gold nanoparticles and small molecule thiols) to create potent nanoscale drugs.

In the Feldheim laboratory, we follow an adapted version of the Kornberg procedure that results in $Au_{230}pMBA_{87}$.[36, 37] Briefly, trihydrate gold chloride ($HAuCl_4 \bullet 3H_2O$) is incubated with pMBA in methanol at basic pH overnight, reducing Au^{3+} to Au^{+} and forming an Au^{+}-pMBA polymer. This is then further reduced by the addition of $NaBH_4$ and results in 2.7 nm ± 0.8 nm Au^0 nanoparticles capped with pMBA. Then, using a modest library of 12 commercially available organo-thiols, shown in Figure 2.1, a small molecule variable ligand display (SMVLD) method was previously developed to create more than 120 different gold nanoparticle conjugates, each with three mixed organo-thiol ligands, and tested for inhibition and resistance formation against different strains of bacteria.[38, 39]

The thiols were chosen to display a variety of functional groups, providing varying degrees of hydrophobicity, hydrogen bonding and charge or mimicking biomolecules such as amino acids and sugars. Activity depended upon the specific

combination of ligands attached to the particle surface and, with a 99.9% minimum inhibitory concentration ($MIC_{99.9}$) of 250 nM for *E. coli* and 625 nM for *K. pneumoniae*, the nanoparticles that have been previously isolated are more potent toward *E. coli* inhibition than many small-molecule antibiotics on the market currently such as ampicillin (12 μM), gentamicin (1 μM), and chloramphenicol (13 μM).[40, 41] Examples of the identified ligand combinations with growth inhibition activity towards *E. coli* are shown in comparison to chloramphenicol in Table 2.2.

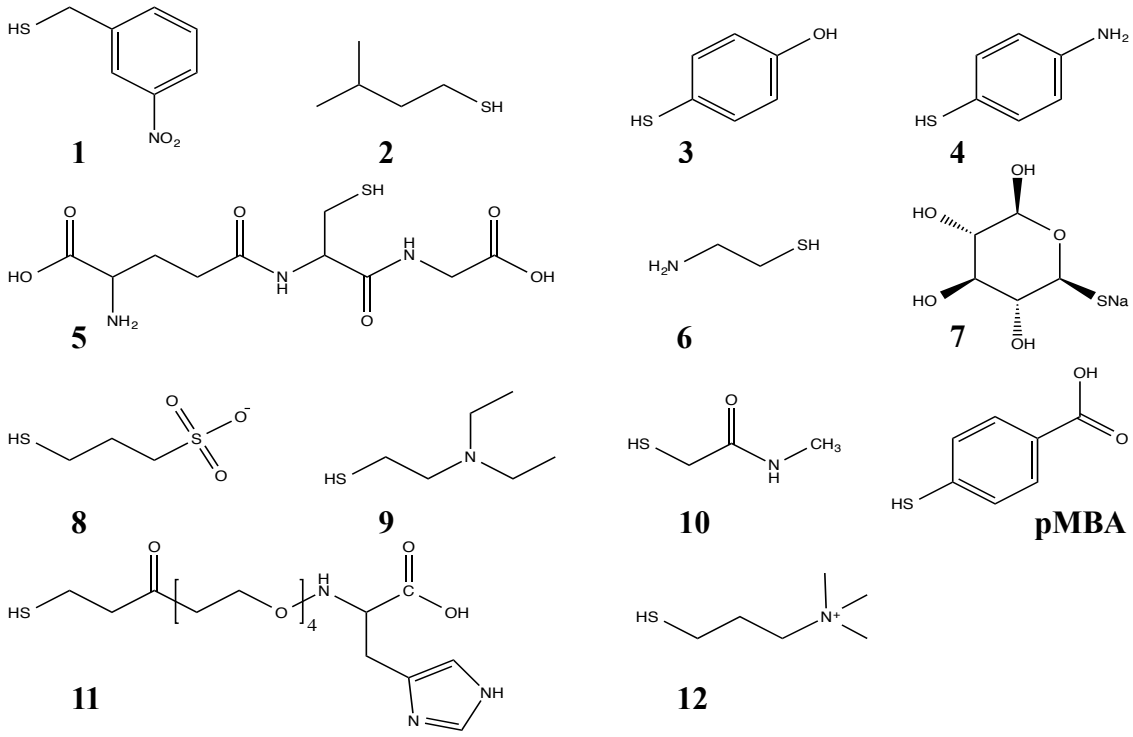

Figure 2.1 Library of para-mercaptobenzoic acid (pMBA) and 12 other organothiols. These molecules were chosen to provide a variety of functional groups. All were commercially available, except for thiol 11, which was a custom synthesized "peptide".

Table 2.2 Active *E. coli* nanoparticle conjugate previously developed with ligand combinations and $IC_{99.9}$ listed. Chloramphenicol is listed to illustrate a current, commercially available antibiotic that was chosen as our positive control in most experiments. (Adapted from ref. 42)

Antibiotic Name	Ligands	$IC_{99.9}$ (μM)
LAL-32	5, 6, 8	0.25
LAL-33	6, 8, 9	0.5
LAL-42	6, 8	1
LAL-52	5, 6, 11	0.25
Chloramphenicol	N/A	12

Former results also indicated that these nanoparticles have essentially equivalent activity against MDR strains of these bacteria, as well as have varying degrees of susceptibility to the evolution of resistance, as shown in Figure 2.2.[42] Preliminary murine studies have also resulted in limited to no *in vivo* toxicity.[43] In summary, our nanoparticles thus far have proven to be potent against both *E. coli* and *K. pneumoniae*. Their ease of synthesis (particularly in the creation of a relatively small library that produced potent hits), lack of cytotoxicity and ability to delay the onset of resistance all contribute to the potential for these conjugates to be one of the few new classes of bacterial antibiotics to emerge in the last decade.

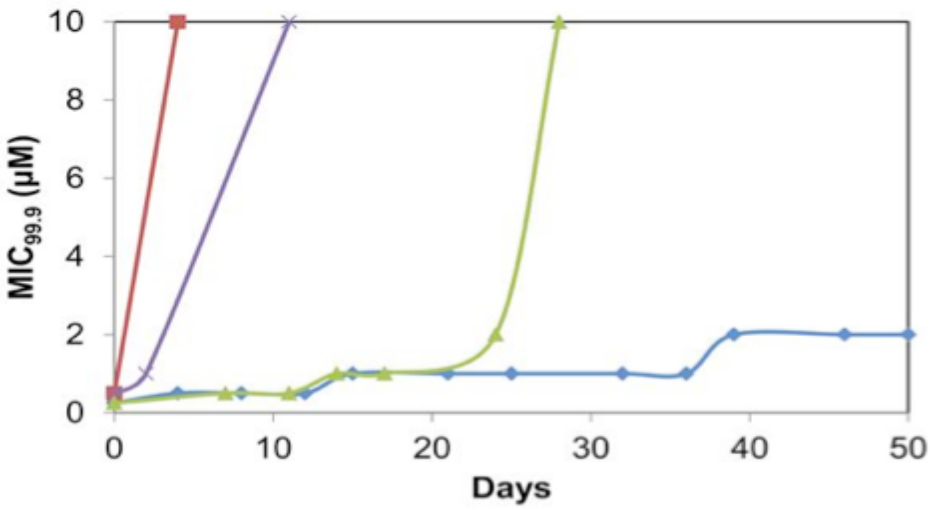

Figure 2.2 Evolution of resistance of *E. coli* to four different nanoparticle conjugates. ■ **LAL-42**, X **LAL-33**, ▲ **LAL-52**, ♦ **LAL-32**. Each point at 10 μM represents the highest concentration tested and the $MIC_{99.9}$ was not reached. (Adapted from ref. 42)

2.2 Development of nanoparticle conjugate active towards *M. smegmatis* growth inhibition

2.2.1 Introduction

My goal was to alter the nanoparticle conjugates described above to be active towards the growth inhibition of mycobacterial targets, for the first time. As will be discussed in depth in the following sections, the SMVLD method allows for simple manipulation of both ligand identity and ligand feed ratio. Could we expand the feed ratio parameter space to tune efficacy and bacterial/mycobacterial specificity? Given the growing concerns with *M. tuberculosis* treatment and resistance, this mycobacterium was chosen as the primary target. However, as TB is a biosafety level three organism due to its infectious nature and limited universal treatment options, *M. smegmatis* is the typical laboratory, non-pathogenic model used for TB.[44, 45]

M. smegmatis is identified as a saprophytic, rapid growing mycobacterium (RGM), meaning it has a doubling time of only 3-4 hours in comparison to the 24 hours of *M. tuberculosis*, that is cultured in Middlebrook 7H9 broth and grown on 7H10 agar, as are other mycobacteria.[46] Despite its non-pathogenicity, *M. smegmatis* possesses numerous homologues to proteins identified in *M. tuberculosis* related to virulence, specifically in two-component systems, sigma factors and hypoxia-responsive genes.[47, 48] Additionally, a protein secretion pathway for antigens ESAT-6 and CFP-10 and the existence of dormancy are both crucial to TB's infectious and persistent abilities and have found to be conserved in *M. smegmatis*.[49, 50, 51] Beyond maintained factors related to virulence between TB and *M. smegmatis*, both mycobacteria have similar general cell wall structures and mycothiol biosynthetic processes.[52]

Furthermore, there is precedence of screening libraries of potential antibiotics against *M. smegmatis* to determine promising hits for TB, resulting in new compounds for treatment of both drug-susceptible and MDR-TB strains.[53, 54] Specifically, the antitubercular class of phenazines were originally identified for their ability to inhibit the growth of *M. smegmatis*, and libraries of both fluoroquinolones and diarylquinolones were first screened against *M. smegmatis* to narrow down compounds to test against TB.[55, 56, 57] Given this information, the use of this model was hypothesized to result in active conjugates against *M. smegmatis* and *M. tuberculosis*.

A series of nanoparticle conjugates with varied feed ratios were screened against *M. smegmatis* for growth inhibition (refer to Section 2.5.3 for a description of the chosen method and a comparison to other established protocols). Once an active ligand combination was found, it was of interest to elucidate further correlations between the

nanoparticle structure and its resulting growth inhibition activity, deemed nanoscale structure-activity relationships (NSAR). These experiments included feed ratio manipulation with ligand quantitation by NMR, specificity assays, and an investigation of the variation in nanoparticle diameter upon feed ratio changes. Finally, it was hypothesized that intracellular targets were affected by our nanoparticle conjugate, conferring bactericidal activity and specificity. To test this hypothesis, several mode of action experiments were completed, consisting of membrane permeability and membrane potential assays followed by TEM imaging.

2.2.2 Nanoscale structure-activity relationship (NSAR) experiments

2.2.2.1 Feed ratio manipulation

From the above-described SMVLD library of 120 nanoparticle conjugates screened previously for *E. coli* growth inhibition, conjugate LAL-33 was shown to have a $MIC_{99.9}$ of 500 nM.[26] This conjugate displayed on its surface pMBA plus ligands 6 (cysteamine), 8 (3-mercapto-1-propane sulfonic acid) and 9 (2-diethylaminoethane thiol). To investigate whether this conjugate had broad-spectrum activity, it was tested against *M. smegmatis* using plating and colony count analysis. LAL-33 showed no activity against *M. smegmatis* up to 10 μM, the highest concentration tested.

However, an important feature of the SMVLD method is that simply adjusting the ratio of thiol ligands attached to the gold nanoparticle surface may further optimize the activity of a lead conjugate! We were thus interested in exploring whether this approach could turn previously identified sets of ligands, such as those present on LAL-33, from an inactive nanoparticle formulation to one with growth inhibition activity towards *M. smegmatis*. We therefore rescreened LAL-33 around an expanded feed ratio parameter

space. LAL-33 is prepared using a feed ratio of 46:1 (thiol to gold) for thiol 6, and 34:1 for thiols 8 and 9. As a result of this expanded search, several potent new conjugates were identified (Table 2.3). A feed ratio of 46:1 for all three thiols yielded the most potent conjugate, resulting in an $MIC_{99.9}$ of 6 μM and a minimal bactericidal concentration (MBC) of 8 μM. We define the MBC as the lowest concentration that provides at least 5 logs or 99.999% of growth inhibition vs. untreated control. This conjugate is designated LAL-3346.

Table 2.3 Results of an expanded feed ratio screen performed to identify new nanoparticle conjugates with *M. smegmatis* growth inhibition activity.

Conjugate Name	Feed Ratio, Thiol 6	Feed Ratio, Thiol 8	Feed Ratio, Thiol 9	% Inhibition	Inhibitory concentration, μM
LAL-33	46	34	34	N/A	>10
LAL-3316	46	46	16	83.7	8
LAL-3333	46	46	34	99.1	8
LAL-3346	46	46	46	99.9	6

To determine whether *M. smegmatis* growth inhibition was due to the thiol-coated gold nanoparticle conjugate or if activity could be recapitulated by the free ligands alone, different combinations of thiols 6, 8, and 9 were mixed in solution and screened for activity. As we have noted for other bacteria previously, no combination of free thiols in solution was active against *M. smegmatis* up to a total thiol concentration of 1 mM. Nanoparticle conjugates were also synthesized with various combinations of only one or two of the ligands at a time (6 only, 8 only, 9 only, 6 & 8, 6 & 9, and 8 & 9). These conjugates were also inactive up to the highest concentration tested, 10 μM. Nanoparticles with only the original pMBA ligand attached also showed no activity at

any concentration up to 50 μM. We therefore conclude that the specific combination of thiols 6, 8, and 9 and the conjugation of these thiols to the nanoparticle surface at a specific feed ratio are necessary for growth inhibition.

The specificity of LAL-3346 for *M. smegmatis* vs. other bacteria was tested using *E. coli*, *K. pneumoniae*, *S. aureus* and methicillin-resistant *S. aureus*, as well as two non-TB mycobacteria *M. abscessus* and *M. avium*. There was no significant activity towards any of these species with the exception of *E. coli*, which had an $MIC_{99.9}$ of 2 μM.

2.2.2.2 Post-exchange nanoparticle size

LAL-3346 was characterized further by transmission electron microscopy (TEM). TEM images of pre- (pMBA-capped nanoparticles) and post-exchange LAL-3346 nanoparticles revealed a change in core diameter from 2.7 nm ± 0.8 nm to 1.6 nm ± 0.6 nm (Figure 2.3). From this result, it was concluded that post-exchange particles were smaller than pMBA-gold nanoparticles, but similarly monodispersed in size. LAL-33, LAL-3316, and LAL-3333 (the inactive or less active conjugates from Table 2.3) were also measured to rule out if the smaller size was conferring activity. In all cases, post-exchange nanoparticles were the same size within standard deviation as LAL-3346, as depicted in Figure 2.4, despite varying degrees of activity towards *M. smegmatis*. This indicated that the size reduction that occurred during the exchange reaction, which is likely the result of Au etching,[58] was not responsible for antimycobacterial activity. Similarly, the presence of thiols 6, 8, and 9 on the surface of these smaller nanoparticles is not sufficient to cause growth inhibition of *M. smegmatis*; instead, it was determined that the specific feed ratios of this ligand combination were responsible for growth

inhibition or cell death of *M. smegmatis*. Representative TEM images used for measuring particle diameters for all five nanoparticle types are shown in Figure 2.5.

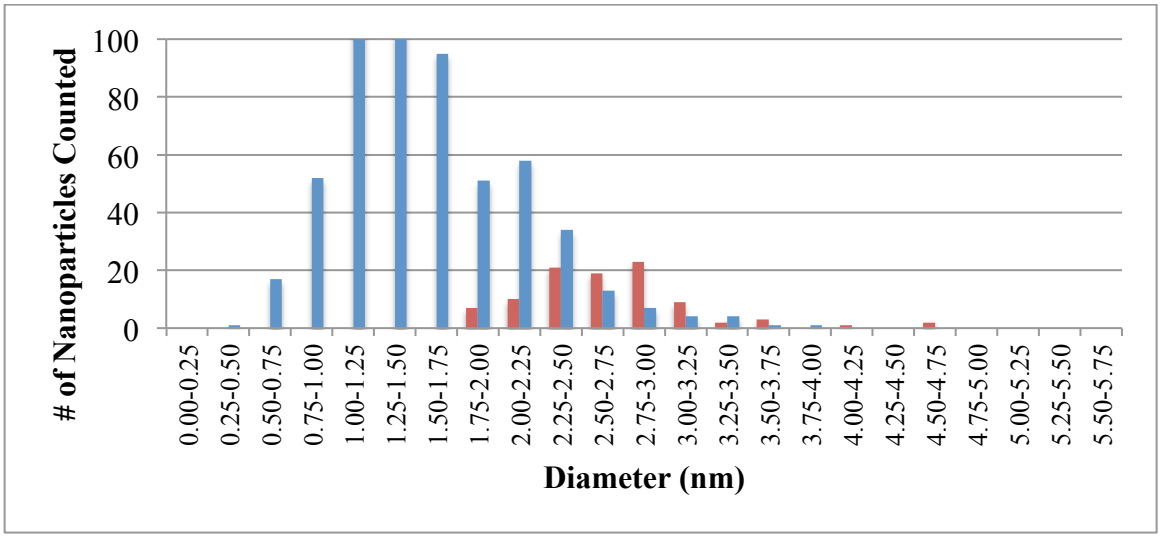

Figure 2.3 Distribution of diameter measurements of pMBA-only (red bars) and LAL-3346 (blue) nanoparticle diameters. Measurements were made in ImageJ software. For pMBA-only nanoparticles, the resulting average diameter was 2.7 nm ± 0.8 nm (sample size = 98), whereas the average size of LAL-3346 nanoparticles was 1.6 nm ± 0.6 nm (sample size 832; two of the largest bars are cut off at 100 nanoparticles for ease of viewing).

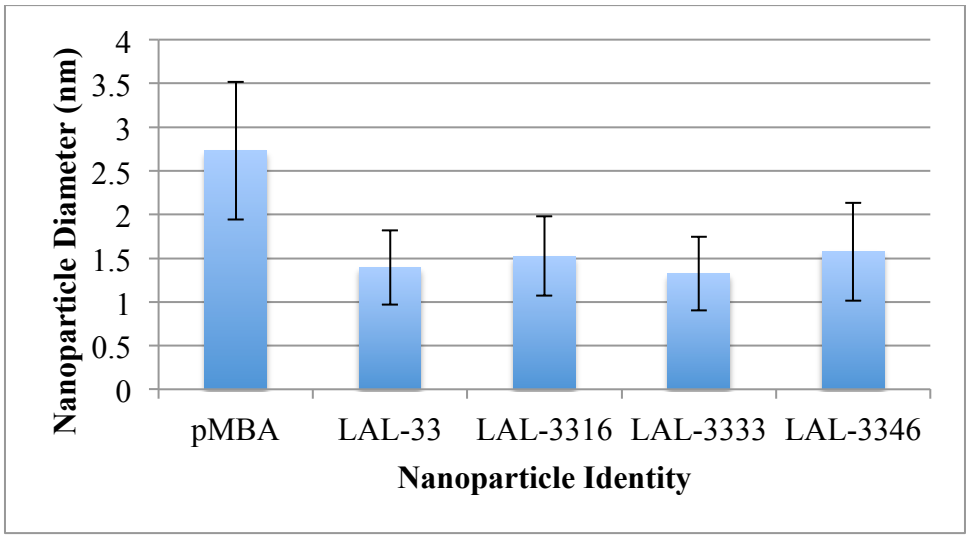

Figure 2.4 Diameter distribution of pMBA-only, LAL-33, LAL-3316, LAL-3333 and LAL-3346 nanoparticle conjugates as determined by measurements on TEM images in ImageJ software. The resulting averages with standard deviation were 2.7 nm ± 0.8 nm, 1.4 nm ± 0.4 nm, 1.5 nm ± 0.5 n, 1.3 nm ± 0.4 nm and 1.6 nm ± 0.6 nm, respectively. All averages were based on measurements of at least 98 nanoparticles per sample type.

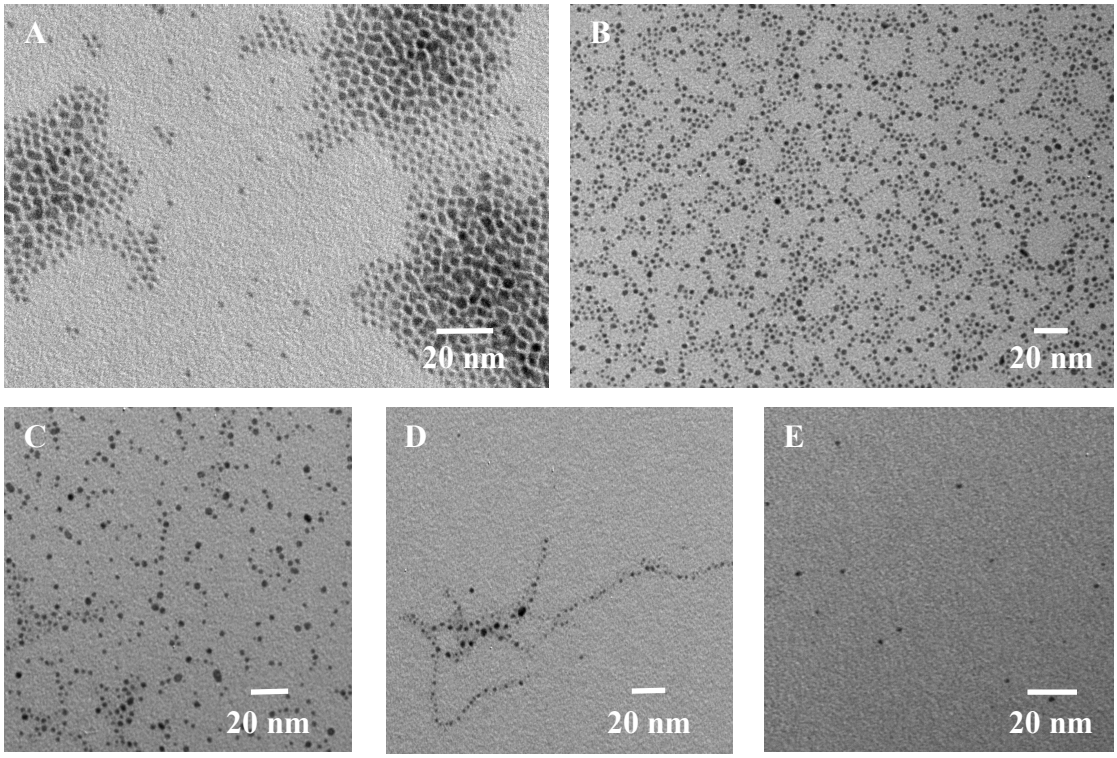

Figure 2.5 Representative TEM images of A) pMBA-only, B) LAL-3346, C) LAL-33, D) LAL-3316 and E) LAL-3333. Scale bars are 20 nm, as denoted in each image.

2.2.2.3 Defining relative levels of thiol ligands on nanoparticles

Solid-state NMR spectroscopy confirmed the presence of all three ligands in relative specific amounts. In brief, the nanoparticle exchange reactions were scaled to produce approximately 20 mg of each nanoparticle conjugate studied. These were dried under vacuum, added to silica at 20% to 40% nanoparticles by weight and mixed to create a homogenous sample for NMR. The resulting approximately 80 mg samples were packed into 5 mm rotors and analyzed by solid-state NMR spectroscopy. Initially, a quantitative spectrum of pMBA-only nanoparticles was obtained, with integrated intensities quantitatively correlating to the 6:1 ratio of aromatic carbons to carboxyl carbons present in the structure of pMBA (Figure 2.6). Although it turned out that the signal to noise was enough to only allow quantitative integration in this case, with one

ligand displayed on the nanoparticle surface, this served as the initial proof of concept for the application of this method to approximate relative ligand ratios on more complex nanoparticles.

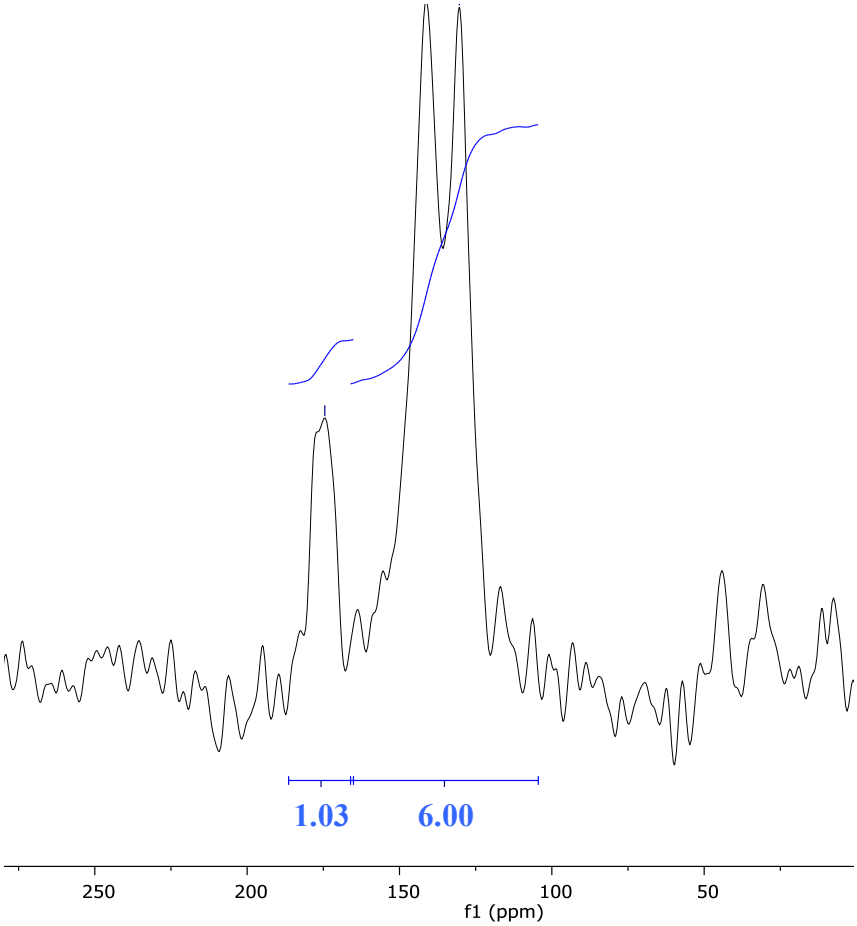

Figure 2.6 ^{13}C CPMAS NMR spectrum of pMBA-only nanoparticles on SiO_2 (25% nanoparticles by weight). The integrated intensities of the aromatic vs. carboxyl carbon correspond to the expected value of 6:1.

Spectra were then obtained, prepared in the same manner as the pMBA-only nanoparticle sample, for nanoparticles with thiol 8 or thiol 9 only, LAL-42 (thiols 6 and 8), LAL-33 (thiols 6, 8 and 9 at the original feed ratios) and LAL-3346. A comparison of thiol 8, thiol 9 and LAL-42 to either LAL-33 (Figure 2.7) or LAL-3346 (Figure 2.8) allowed for deconvolution of overlapping peaks and assignment of each peak to its

corresponding thiol. By normalizing to the unique peak of the methyl carbons of thiol 9, semi-quantitative molar ratios of each ligand were determined. An overlay of LAL-33 and LAL-3346 in Figure 2.9 depicts the spectral differences that led to these conclusions.

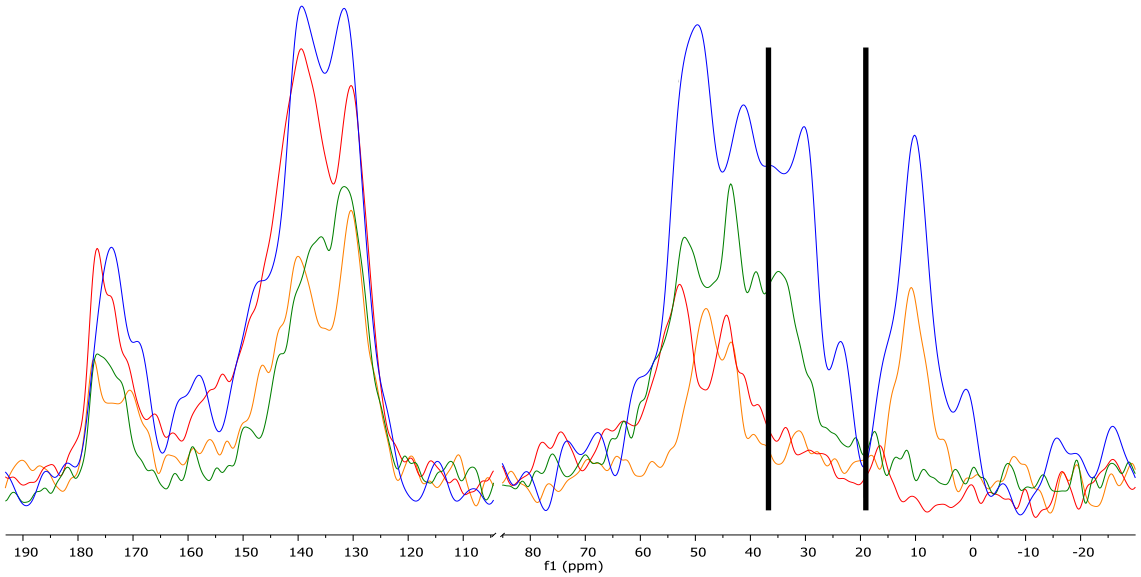

Figure 2.7 The superposition of the ^{13}C CPMAS NMR spectra of LAL-33 (blue), LAL-42 (green), thiol 8 only nanoparticles (red) and thiol 9 only nanoparticles (orange). Black bars indicate the spectral features that must be due to thiol 6 only.

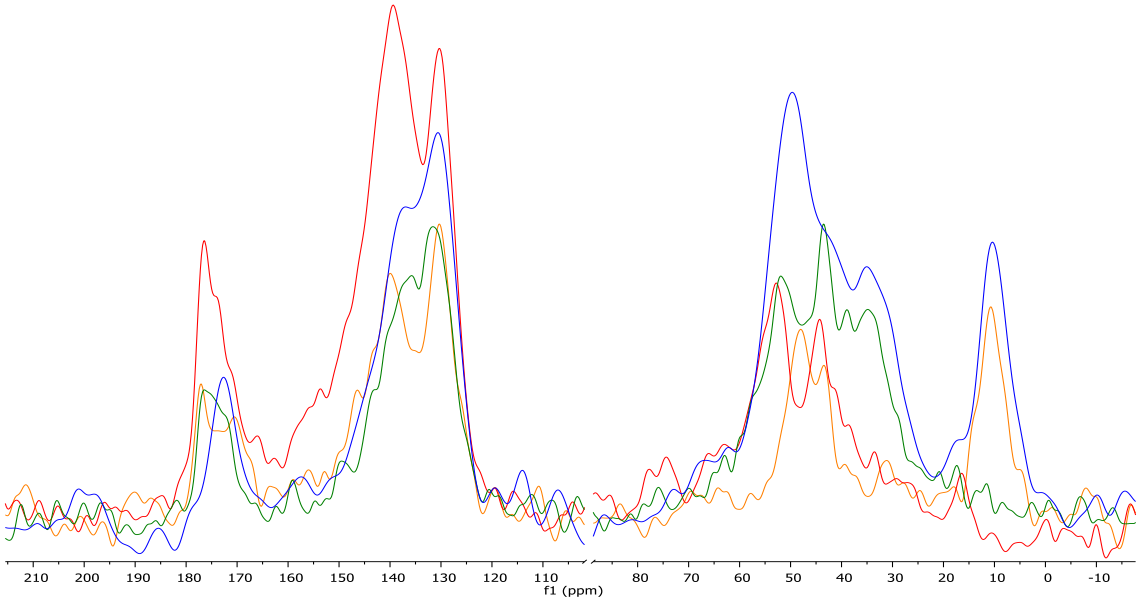

Figure 2.8 The superposition of the ^{13}C CPMAS NMR spectra of LAL-3346 (blue), LAL-42 (green), thiol 8 only nanoparticles (red) and thiol 9 only nanoparticles (orange).

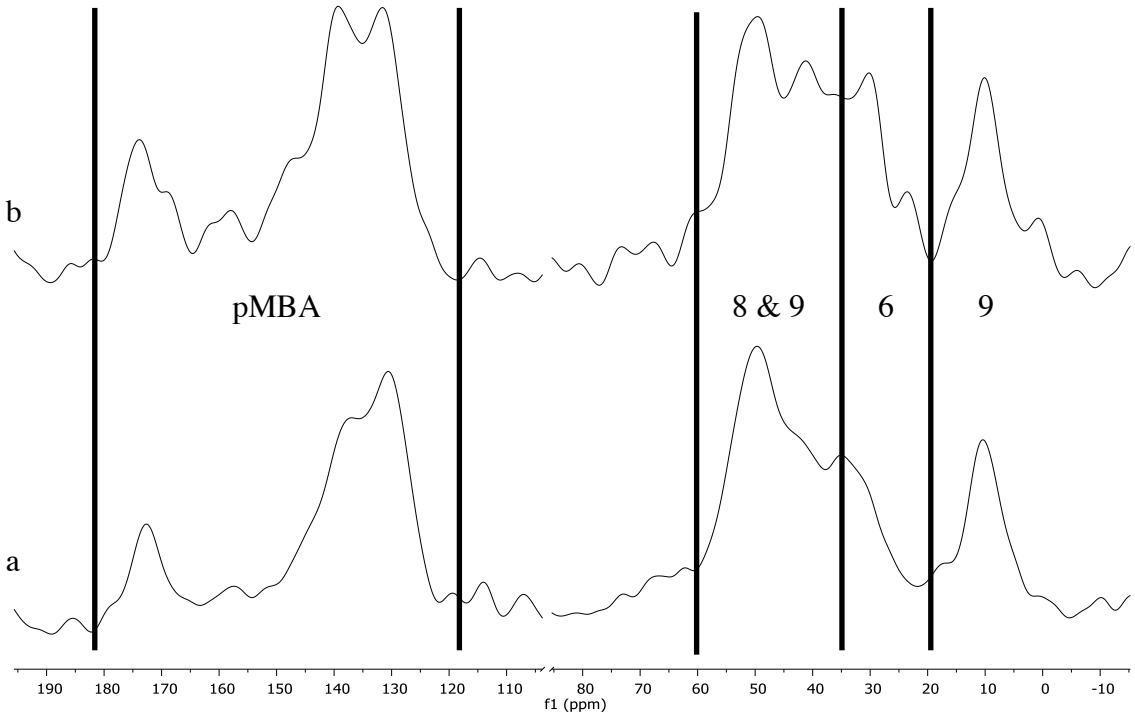

Figure 2.9 Overlay plot of the ^{13}C CPMAS NMR spectra of LAL-3346 (a) and LAL-33 (b), each deposited on SiO_2 at approximately 25% nanoparticle by weight. Black bars indicate regions of spectral features due to each ligand: pMBA (120-180 ppm), 6 (25-35 ppm), 8 (35-60 ppm) and 9 (10 ppm, 35-60 ppm).

In summary, the solid-state NMR studies showed that all ligands input into the exchange reaction were present on both LAL-33 and LAL-3346, and that the molar ratio of thiol 8 to thiol 6 observed did increase from LAL-33 (0.6:1.2 thiol 8:6) to LAL-3346 (1.0:1.3 thiol 8:6) as would be expected by the increase in feed ratio. These results indicate that adjusting the ligand feed ratio does affect the molar ratio of ligands bound to the surface of the nanoparticles. It must be noted, however, that this method is evaluating the population and the molar ratios presented represent an average composition of that population. Both the feed ratios and resulting molar ratios as determined by the above NMR spectra are compared for LAL-33 and LAL-3346 in Table 2.4.

Table 2.4 Comparison of feed ratios input and molar ratios determined from NMR spectra for LAL-33 and LAL-3346. The values presented have been normalized to pMBA for ease of comparing exchanged thiol ratios.

		Thiol 6	Thiol 8	Thiol 9	pMBA
LAL-33	**Feed Ratio**	46	34	34	N/A
	Molar Ratio	1.2	0.6	0.9	1.0
LAL-3346	**Feed Ratio**	46	46	46	N/A
	Molar Ratio	1.3	1.0	1.3	1.0

2.2.3 Mode of action experiments

2.2.3.1 Membrane permeability

Several experiments were then performed to investigate the mode of action of these particles. As with the *E. coli* inhibitors published previously, LAL-3346 nanoparticles contain the cationic ligands 6 and 9, which have the potential to disrupt cell membranes.[59, 60] Therefore, an assay to probe membrane integrity and cell viability was completed first using the LIVE/DEAD BacLight Bacterial Viability kit from Invitrogen. Briefly, this kit employs two fluorescent nucleic acid stains that differentially access the inside of cells based on membrane permeability. SYTO-9 labels all cells, live or dead, regardless of membrane integrity; it fluoresces green. The second stain, propidium iodine (PI), fluoresces red and is only able to stain the bacteria's nucleic acids if membrane damage allows the molecule internal access. Furthermore, when both stains are present simultaneously, propidium iodine decreases the fluorescence of SYTO-9, ensuring the resulting fluorescent signal is distinctly due to PI and red.

M. smegmatis was incubated with LAL-3346 nanoparticles ranging in concentration from 0.25 μM to 16 μM, as well as 1% Triton-X as a positive control that induces cell membrane damage. Upon each treatment, a change in the ratio of red PI fluorescence to green SYTO-9 fluorescence was monitored. This ratio was then converted to % by dividing it by the red:green ratio for untreated cells. An increase in percentage corresponds to increasing membrane permeability. LAL-3346 was determined to increase the fluorescent ratio by between 11% and 17%, summarized in Table 2.4. In comparison to 1% Triton-X, the highest concentration of LAL-3346 caused one quarter of the amount of increase in fluorescence ratio. These lower percentages indicate that while membrane permeability is increased in the presence of LAL-3346, cells could still be viable and membrane disruption is unlikely to be the most significant mode of action of nanoparticle activity.

Table 2.5 *M. smegmatis* membrane permeability assay results by LIVE/DEAD BacLight Bacterial Membrane kit from Invitrogen in the presence of increasing concentrations of LAL-3346 nanoparticles. The averages listed are from five technical replicates, using the same batch of nanoparticles in each replicate.

Particle Concentration (μM)	Increase in Fluorescence Ratio (%)
0.25	-5 ± 12
1	11 ± 18
4	15 ± 2
16	17 ± 16
1% Triton-X	58 ± 4

2.2.3.2 Membrane potential

Next, we employed a BacLight Bacterial Membrane Potential kit and flow cytometry to investigate changes in membrane potential that might be induced by the presence of pMBA or LAL-3346 nanoparticles. $DiOC_2(3)$ is a fluorescent dye that typically emits green fluorescence at 530 nm and can cross the cell membrane; in healthy cells with an intact membrane potential, the cytosolic concentration of $DiOC_2(3)$ is greatly increased, resulting in aggregation of the dye and a shift in fluorescence to red emission (600 nm).[61] This shift allows the dye to act as a membrane potential indicator. Data for these experiments are plotted such that the green fluorescence is labelled FL_2 and on the y-axis, and red fluorescence is labelled FL_1 and on the x-axis; each red point represents the fluorescence signal of one cell as it flows past the detector in the instrument.

In comparison to the untreated but $DiOC_2(3)$-stained negative control (Figure 2.10F), which represents cells with a normal membrane potential that rapidly uptake the dye, LAL-3346 (Figure 2.10C, D) was observed to have a similar red fluorescent emission, indicating similar cellular absorption of $DiOC_2(3)$ and membrane potential. However, pMBA nanoparticles (Figure 2.10B) behaved more like the positive control in the experiment, carbonyl cyanide 3-chlorophenylhydrazone (CCCP, Figure 2.10A), a reagent that reduces membrane potential by eliminating proton gradients. Figure 2.10E illustrates the detection of the auto-fluorescence of *M. smegmatis*, when no treatment or fluorescent stain was applied. The shifts in fluorescent counts are further depicted quantitatively in Figure 2.11, by presenting relative amounts of fluorescence that fall into each of the three outlined regions in flow cytometry plots.

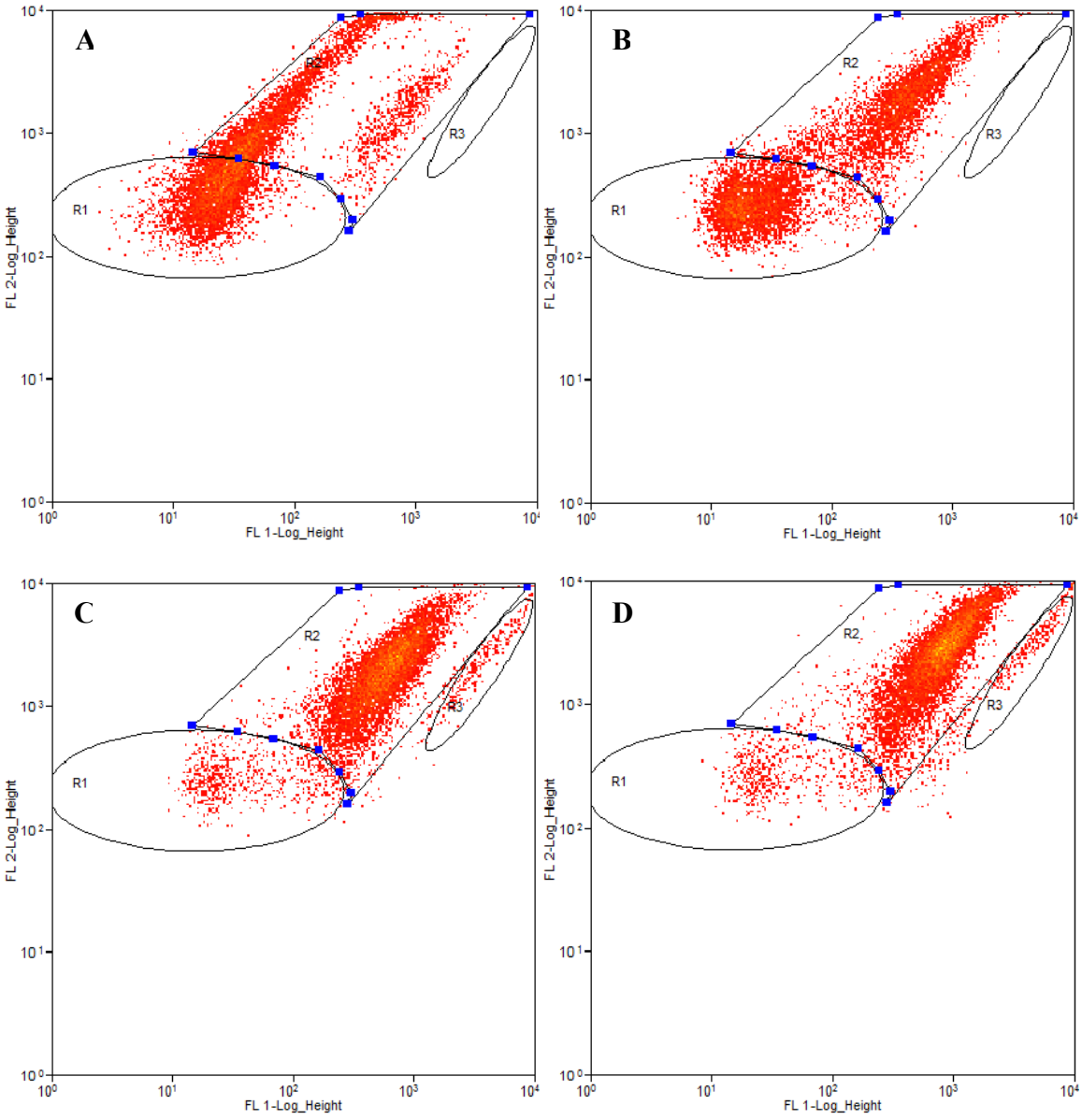
A
B
C
D
R1
R2
R3
FL 2-Log_Height
FL 1-Log_Height

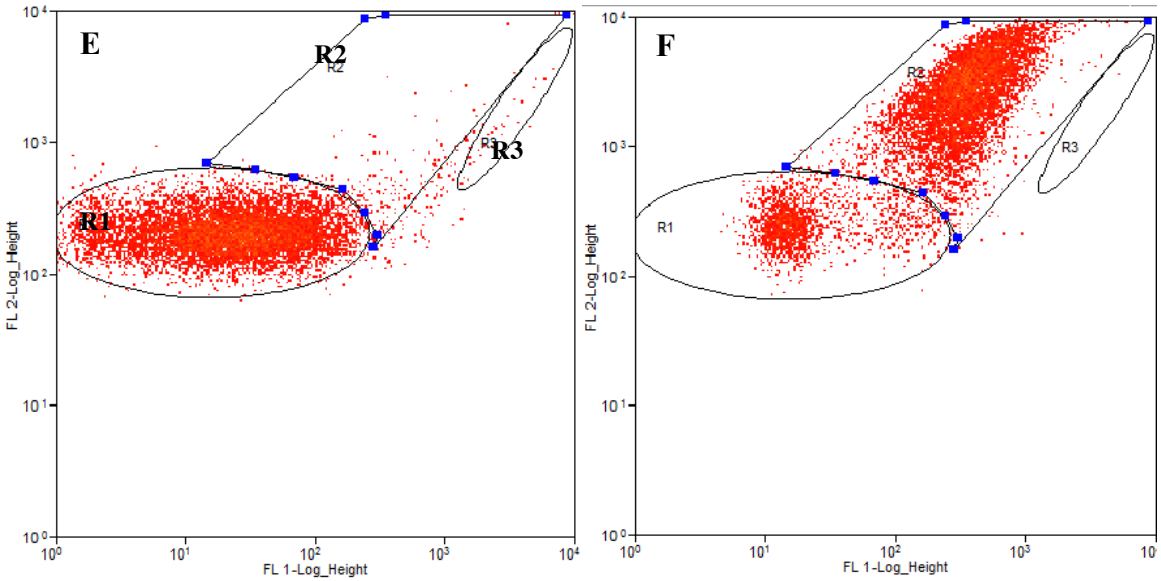

Figure 2.10 Changes in *M. smegmatis* membrane potential as measured in one flow cytometry assay due to incubation with CCCP (positive control, panel A), 8 μM pMBA base nanoparticles (B), and 6 μM and 8 μM LAL-3346 nanoparticles, respectively (C) and (D), after staining with $DiOC_2(3)$. Negative controls with mycobacterium only (E) and no treatment but $DiOC_2(3)$ (F) are also shown. Gated regions R1, R2 & R3 are labeled in panel E for use in Figure 2.11. All LAL-3346 nanoparticles used were prepared from the same batch of pMBA-only nanoparticles.

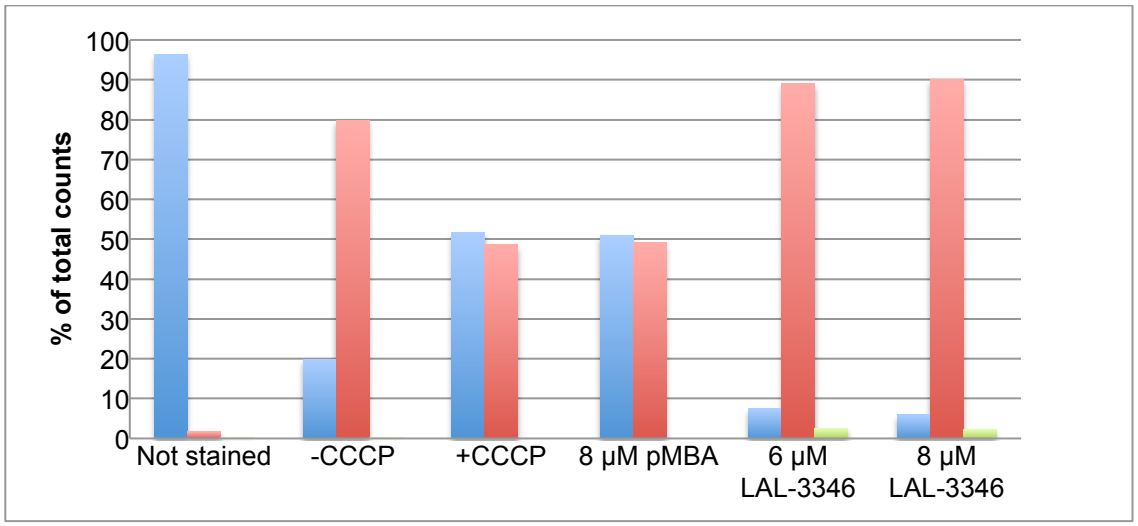

Figure 2.11 Quantitative comparison of the relative number of fluorescent counts in each of the three regions previously identified and outlined in the flow cytometry plots in Figure 2.10 (see panel E for region labels). Percentages for R1 (blue bars), R2 (red bars) and R3 (green bars) were determined by the counts in each region divided by the total number of counts (approximately 10,000 for each sample).

The first notable shift in fluorescence is between the auto-fluorescence of untreated *M. smegmatis* and the fluorescence due to the uptake of $DiOC_2(3)$. At this point, any remaining fluorescence in R1 is due to unstained mycobacteria. Upon treatment with either CCCP or 8 μM pMBA-coated nanoparticles, the red fluorescence due to normal cellular membrane potential and the uptake of $DiOC_2(3)$ is decreased and approximately half of the cells return to the R1 region. Finally, treatment with bacteriostatic or bactericidal concentrations of LAL-3346 maintains the high red fluorescence of $DiOC_2(3)$, indicating an intact membrane potential. Based on the relative amounts of fluorescence, it may be concluded that LAL-3346 actually increases the membrane potential slightly over normal. The region labeled R3 encompasses a third small population of cells that have a unique fluorescent signal only present when treated with LAL-3346. *M. smegmatis* after incubation with LAL-3346, but without $DiOC_2(3)$ fluorescent stain, should be analyzed in the future in an attempt to elucidate if R3 arises due to the nanoparticles on their own. In summary, these experiments indicated that pMBA-coated gold nanoparticles affect the membrane potential without causing growth inhibition or cell death, while LAL-3346 nanoparticles affect cell growth but do not decrease the membrane potential in comparison to the controls.

2.2.3.3 Transmission electron microscopy

In order to gain further insight into the interactions between gold nanoparticles and *M. smegmatis*, nanoparticles were incubated with *M. smegmatis* cells. The cells were then pelleted, washed to remove un-associated nanoparticles, and taken through a fixation and sectioning procedure prior to imaging by TEM. The images taken show pMBA-coated gold nanoparticles clumped together outside of the mycobacterial cell membrane,

potentially providing a mechanistic basis for the disrupted membrane potential observed by flow cytometry. In contrast, LAL-3346 nanoparticles were internalized into the mycobacteria (Figure 2.12). The potential therefore exists for LAL-3346 to affect *M. smegmatis* growth by interacting with intracellular biomolecular targets. It should be noted that the magnification required to view nanoparticles in the TEM images prevents imaging of entire cells or populations of cells. This means that while the images certainly indicate trends in nanoparticle interactions with *M. smegmatis*, we are unable to report on the entire population. Images seen only represent a small subset (tens of cells) of the total number of mycobacteria (millions to billions of cells) in any given incubation with nanoparticles.

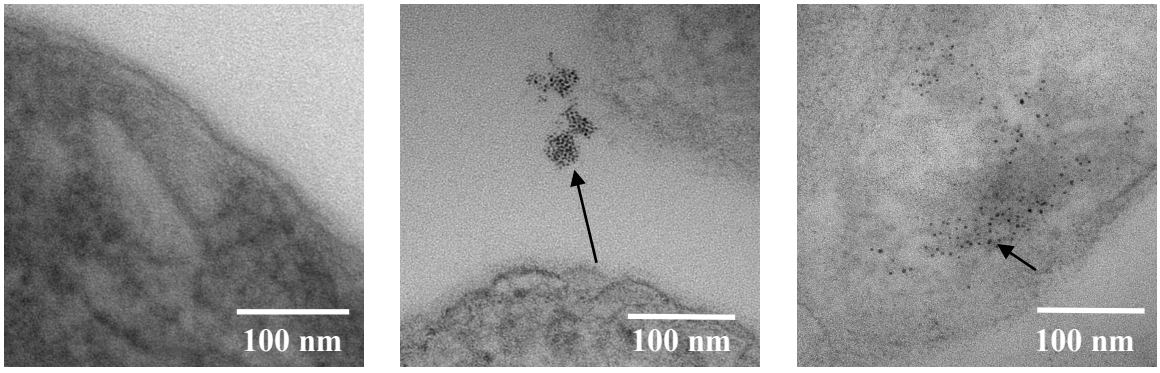

Figure 2.12 Transmission electron micrographs of untreated *M. smegmatis* (left panel), *M. smegmatis* treated with pMBA-only gold nanoparticles (middle panel) and *M. smegmatis* treated with LAL-3346 nanoparticles (right panel). The arrows indicate the edge of the cell membrane at their tails and the location of the nanoparticles at their points.

2.3 Potential application to TB or non-TB mycobacterium (NTM)

2.3.1 Dithiol ligands for increased long-term stability

In order to move from *M. smegmatis* growth inhibition to *M. tuberculosis*, the long-term stability of the nanoparticles in Middlebrook 7H9 media at 37ºC needed to be

optimized, as TB is cultured over several weeks rather than the three-day growth period for *M. smegmatis*. By incubating LAL-3346 in 7H9 broth at 37ºC at a concentration 2x the MBC, growth inhibition assays could be completed over time by diluting this stock of nanoparticles. It was quickly determined that within one week, 10% of activity was lost, seen as a decrease from bactericidal to 90% growth inhibition at the same concentration of nanoparticles (8 μM). After two weeks, less than 50% growth inhibition was observed. As is, it will be unlikely that LAL-3346 will remain functional and able to inhibit the growth of TB over the necessary time period. This loss in efficacy of LAL-3346 was hypothesized to be due to degradation or exchange of ligands off of the surface of the gold nanoparticle, since we have previously shown that both the attachment of the ligands to and the specific ratio of each on the nanoparticle surface are necessary for growth inhibition.

It was therefore surmised that we could increase the stability of LAL-3346 in 7H9 and at 37ºC by using dithiol or disulfide versions of the ligands. The ability of a dithiol to form two gold-sulfur bonds with the nanoparticle surface could allow the ligand to remain attached throughout longer experiments. Thiol 8, 3-mercapto-1-propane sulfonic acid, was commercially available as a dithiol (2,3-dimercapto-1-propanesulfonate) from Sigma-Aldrich; this dithiol was purchased and labeled as thiol 17. An organic chemist within the Feldheim laboratory, Dr. Ganghyeok Kim, was successfully able to synthesize a disulfide version of thiol 6 as well, referred to as thiol 16. Chemical structures of thiols 16 and 17 are shown in comparison to thiols 6 and 8 in Figure 2.13. Starting with the incorporation of these two dithiol/disulfide ligands onto LAL-3346, numerous feed ratio combinations were tested for solubility, purification survival and *M. smegmatis* growth

inhibition. In result, two feed ratios that incorporated dithiol 16 were discovered to have the same MBC as LAL-3346; these are LAL-3346A and LAL-3346N. LAL-3346A displays pMBA as well as thiols 6, 8, 9 and 16 at 46x gold feed ratios, whereas LAL-3346N has the same thiols presented, but with thiol 16 at double the feed ratio (92x). A summary of all combinations tested is listed in Table 2.5.

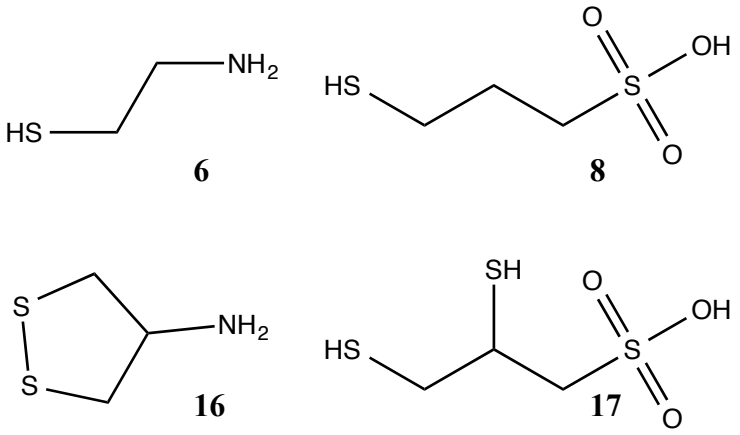

Figure 2.13 Comparisons of dithiol/disulfide versions of ligands 6 (cysteamine) and 8 (3-mercapto-1-propane sulfonic acid). Ligand 16 is 2-amino-1,3-propane disulfide and replaces 6, whereas ligand 17 is 2,3-dimercapto-1-propanesulfonic acid to replace 8.

Unfortunately, further stability testing could not be completed, as we did not have enough of thiol 16. Interestingly, 2-aminobutane-1,4-dithiol is commercially available from Sigma-Aldrich, but as the name indicates, it has an additional carbon (butane vs. propane). The same feed ratios were repeated with the butane version of thiol 16, without success. Nanoparticles were not as soluble in water after exchange and did not result in the same efficacy as LAL-3346A or N. This again demonstrates the specific requirement of both ligand identity and feed ratio for the function of these nanoparticle antibiotics.

Table 2.6 Incorporation of thiols 16 and 17 into LAL-3346 nanoparticles. For each feed ratio variation tried, the result was either no pellet formed during purification (NP), precipitated out during wash steps (P) or able to be tested. Conjugates were tested up to 8 μM; if none of the concentrations tested inhibited growth, then this is indicated by a "-" symbol.

Version of LAL-3346	Feed Ratio, Thiol 6	Feed Ratio, Thiol 8	Feed Ratio, Thiol 9	Feed Ratio, Thiol 16	Feed Ratio, Thiol 17	Result	$IC_{99.9}$ (μM)
original	46	46	46	-	-	T	6
A	46	46	46	46	-	T	8
B	-	46	46	46	-	P	N/A
C	-	46	46	92	-	T	-
D	-	46	46	138	-	T	-
E	46	46	46	-	46	P	N/A
F	46	23	46	-	46	P	N/A
G	46	-	46	-	46	P	N/A
H	46	-	46	-	92	P	N/A
I	-	46	46	23	-	NP	N/A
J	46	-	46	-	23	T	-
K	-	-	46	23	23	T	-
L	23	46	46	46	-	NP	N/A
M	46	-	46	-	138	NP	N/A
N	46	46	46	92	-	T	8

2.3.2 Expanded feed ratios for activity towards NTM

As previously mentioned, LAL-3346 showed no activity towards two non-tuberculosis mycobacteria tested, *M. abscessus* and *M. avium*. In order to continue to test the expanded feed ratio theory, numerous exchange combinations of thiols 6, 8, and 9 were created, varying feed ratios for each thiol as listed in Table 2.6. No combination

attempted showed any activity towards either NTM up to 10 μM, the highest concentration tested.

Table 2.7 Expanded feed ratios of LAL-3346 conjugate tested for growth inhibition of *M. abscessus* and *M. avium*.

Version of LAL-3346	Feed Ratio, Thiol 6	Feed Ratio, Thiol 8	Feed Ratio, Thiol 9
original	46	46	46
1	69	46	46
2	92	46	46
3	46	69	69
4	46	92	46
5	46	46	69
6	46	46	92
7	92	92	46
8	92	46	92
9	46	92	92
10	92	92	92
11	69	69	46
12	69	46	69
13	46	69	69
14	69	69	69

2.4 Conclusions and future outlooks

In conclusion, we have successfully applied our SMVLD method to the discovery of active nanoparticle conjugates for *M. smegmatis* growth inhibition, as illustrated in Figure 2.14. The most active mixed thiol/gold nanoparticle conjugate, LAL-3346, was discovered by expanding the ligand feed ratio space around a previously established

conjugate (LAL-33) that was active for *E. coli* inhibition. Remarkably, by slightly adjusting the feed ratio of two out of three thiols in the ligand exchange reaction, we were able to transition from a ligand composition that was inactive toward *M. smegmatis* to one that was highly potent (LAL-3346). This result adds significantly to our previous understanding of the nanoscale structure-activity relationships (NSAR) of these nanoparticles, which was in part that both the combination of ligands and their attachment to the nanoparticle surface is necessary for activity. As a result of this work, we now know that the specific density of ligand sets should also be considered when formulating highly active antibiotic nanostructures. This feature has interesting implications in considering these nanoparticle conjugates as future platforms for antibiotic discovery, in which discrete sets of ligands can be identified with antimicrobial properties. Tuning properties for bacterial specificity and efficacy then may rely only upon the specific feed ratio of each ligand in the defined set. In developing active conjugates for other pathogens, these previously identified ligand sets would limit the number of combinations necessary to screen in order to find a conjugate that is active for bacterial growth inhibition.

It has also been shown that LAL-3346 appears to be internalized, without significantly altering membrane permeability or membrane potential and suggesting that intracellular targets may be accessed by gold nanoparticles. The specific origin of these targets may be explored in the future with a DNA microarray or RNA sequencing analysis; however, data from similar experiments with *E. coli* and *Klebsiella pneumoniae* in the laboratory implicate disruption of cell division to be a major component of the nanoparticle conjugates activity. This would be a relatively unique mycobacterium drug

target, as a majority of current TB antibiotics inhibit or disrupt protein, RNA or DNA synthesis as their primary mode of action.[27] Additionally, pathways involving cell wall biosynthesis and cellular stress responses to metal contamination were both up regulated in *E. coli* and *K. pneumoniae* studies. Isoniazid and pyrazinamide both target mycolic acid synthesis and membrane transport, indicating cell wall targets are previously established to cause growth inhibition.[27] Furthermore, stress responses to metal contamination is not unexpected given gold makes up the core of our nanoparticles. It would be of interest to start by investigating the possibility that *M. smegmatis* is similarly affected by LAL-3346.

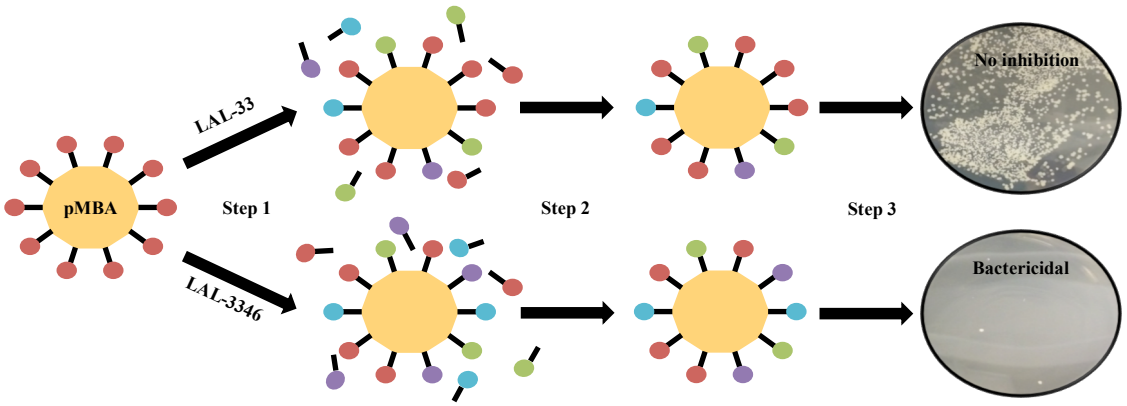

Figure 2.14 Schematic of the overall SMVLD method and its application to LAL-33 vs. LAL-3346 with the resulting *M. smegmatis* growth inhibition. Step 1 describes the initial SMVLD exchange reaction. In the second step, exchanged nanoparticles are purified, washed and concentrated. Finally, each nanoparticle type is incubated with *M. smegmatis* and growth inhibition is determined via plating and colony counting (step 3).

While the mechanism of nanoparticle passage through the mycobacterial cell membrane has not yet been elucidated, it may be occurring via several different pathways. First, as discussed earlier, the possibility of thiol 6 and 9 to act as cations and disrupt the membrane could contribute to cell growth inhibition and death. Since the pKa values of the amine groups of both thiols are between pH 10 and 11, a majority of the

population should be protonated and positively charged at neutral pH.[62] However, a lack of significant increase in membrane permeability was observed, indicating that this is likely not the most crucial contributor to efficacy towards *M. smegmatis*. Therefore, other potential methods of entering the cell may play a larger role.

The porin MspA has been shown to provide the main hydrophilic route through the membrane of *M. smegmatis*.[63] However, its constriction site has been reported to be only 1.3 nm ± 0.3 nm in diameter.[64, 65] The larger end of this size range could allow for entry of some portion of the 1.6 nm ± 0.6 nm LAL-3346 nanoparticles, but that does not account for the preferential efficacy of LAL-3346 over LAL-33, LAL-3316 or LAL-3333, which could also all obtain at least some entry via MspA. The remaining pathway to address then is passive diffusion directly through the membrane itself. While this seems hard to imagine, given the complexity of the membrane structure and its well-known ability to prevent access, there is precedence for "snorkelling" in other systems, a phenomenon in which a mixture of hydrophobic and sulfonate ligands displayed on gold nanoparticle surface use their flexibility to insert the conjugate into membranes.[66, 67, 68, 69] In additional support, mixed-monolayer nanoparticles have been shown to have unexpected solubility properties,[70] possibly aiding in their ability to interact with and enter into cell membranes. The increase in feed ratios of both thiols 8 and 9 could increase the ability for these nanoparticle conjugates to "snorkel" and successfully pass through the cell membrane.

Thus far, it is concluded that the combination of thiols 6, 8 and 9 as displayed on LAL-3346 is specific for *M. smegmatis*, potentially due to differences in the cell wall. Mycobacteria have very complex and unique cell walls that provide a strong defense

mechanism against a myriad of antibiotics. The outermost layer of the mycobacterial cell wall is made up of glycopeptidolipids, mycolic acids and variations of lipoarabinomannan (LAM).[71, 72] One specific example of cell wall variation is the phosphoinositol-capped LAM (PI-LAM) of *M. smegmatis*, which is similar to *M. fortuitum* but not to the mannose-capped LAM (Man-LAM) of TB or either NTM.[29, 73] If LAM identity plays a role in the ability of LAL-3346 to interact with *M.* smegmatis, then it may inhibit growth of *M. fortuitum*, without affecting *M. avium* and *M. abscessus* as observed. Nanoparticle antibiotics with growth inhibition activity towards other pathogenic mycobacteria might be found by expanding the feed ratios of the remaining previously identified active conjugates (LAL-32, LAL-42 or LAL-52).

Finally, upon synthesis of dithiol 16, it would be of significant interest to study LAL-3346A and LAL-3346N in more extensive detail, particularly focused on if long-term stability is gained by the addition of a dithiol or disulfide ligand to these conjugates. The potential gain in stability would allow for more confident testing of these conjugates against slow-growing mycobacterium, such as *M. avium* and *M. tuberculosis*. In an era of necessity, our nanoparticle exchange method and its success toward the non-pathogenic TB surrogate *M. smegmatis* provides a potential innovative pathway for the future development of new antibiotics against challenging bacterial or mycobacterial pathogens.

2.5 Experimental

2.5.1 Synthesis of pMBA-Au nanoparticles

pMBA-modified, 2 nm diameter gold nanoparticles were synthesized as described. Approximately 136 mg of $HAuCl_4 \cdot 3H_2O$ (Sigma Aldrich) was dissolved in 20 mL methanol. Simultaneously, approximately 210 mg para-mercaptobenzoic acid

(pMBA) (TCI-America) was dissolved in 15.4 mL ultrapure H_2O and 0.64 mL 10 M NaOH by vigorous shaking. The pMBA solution was then added to the stirring gold solution. This polymer formation reaction was allowed to react overnight with constant stirring. The solution was then split into three flasks and diluted with 62 mL methanol and 178 mL ultrapure H_2O. A 7.5 mL 0.25 M solution of $NaBH_4$ (Sigma Aldrich) was freshly prepared, and 2.4 mL was added to each of the three reaction flasks. The solution was diluted further with 24 mL ultrapure H_2O then the nanoparticle formation reaction was allowed to proceed for another 24 hours with constant stirring. To harvest the nanoparticles, 2 mL 5 M NaCl and 150 mL methanol was added to each flask to cause precipitation. The precipitated nanoparticles are then pelleted in 50 mL conical tubes by centrifugation at 3,200x g for 5 minutes. The pellets are left to air-dry overnight, before resuspending in filter-sterilized ultrapure H_2O and washing six times on 10k M.W.C.O. filters (Millipore). The nanoparticle concentration was determined by UV-visible spectroscopy using the ε_{510} of 409,440 $M^{-1}cm^{-1}$, which was determined previously by Dr. Chris Ackerson. This was done by creating a standard curve of absorbance values from known amounts of nanoparticles, assuming the formula $Au_{144}(pMBA)_{60}$, resulting in a similar extinction coefficient to other published 2 nm Au-pMBA nanoparticles.[74] Nanoparticle size and distribution is observed by 15% tris-borate-EDTA polyacrylamide gel electrophoresis and transmission electron microscopy.

2.5.2 Place exchange reactions

Four-milliliter exchange reactions were started by first diluting 29.6 nmol of pMBA-Au nanoparticles in 4 mL of sterile 20 mM Na_2HPO_4 pH 9.5. Ligands 6 (cysteamine), 8 (3-mercapto-1-propane sulfonate) and 9 (2-diethylaminoethane thiol)

were added in specific molar feed ratios (46x molar amount of gold for all three ligands on the most potent *M. smegmatis* nanoparticles, LAL-3346) from 20 mM frozen stocks in water. Reactions are shaken at 19°C for 24 hours. The place exchange nanoparticle products are then harvested by the addition of 2 mL 5 M NaCl and 9 mL methanol. Precipitated nanoparticles are collected by centrifugation at 3,200x g for 5 minutes. Pellets are resuspended in 4-6 drops filter-sterilized ultrapure H_2O then precipitated again with 0.5 mL 5 M NaCl and approximately 8 mL methanol. Centrifugation was repeated and pellets were dried overnight then resuspended and washed eight times with filter-sterilized ultrapure H_2O over 10k M.W.C.O. filters (Millipore). Purified nanoparticles are quantified the same as before, using UV-visible spectroscopy and a ε_{510} of 409,440 $M^{-1}cm^{-1}$.

2.5.3 Bacterial growth inhibition assays

A plating and colony count method was used for nanoparticle conjugate susceptibility testing and to determine inhibitory nanoparticle concentrations. This method was chosen for its direct quantitation of growth inhibition and ease of experimental setup, despite being a more time and labor-intensive method. A colorimetic assay using Alamar Blue, which only requires the time necessary for growth in liquid culture, has been successfully employed in drug susceptibility screens;[75] however, as solutions containing nanoparticles are already colored, it was a concern that the color change would be less clear in the presence of nanoparticles. Numerous other agar-based methods also exist, such as disk diffusion, the Etest and luciferase reporting via the "Bronx Box".[76, 77, 78] In each technique, varying amounts of a specific antibiotic are incorporated into the agar and the concentration at which a transition from growth to no

growth occurs is identified as the minimum inhibitory concentration. While all three of these methods require the same amount of time as plating and colony counting, they are somewhat subjective as the amount of growth inhibition or the transition where that occurs can be unclear. Finally, there are more advanced instruments available for both radiometric and fluorescent detection of antibiotic susceptibility, specifically BACTEC technology.[79, 80] However, as mentioned, these require specialized and expensive instrumentation, as well as the possible handling of radioactive material (depending on the way in which the measurements are performed).

For all antibiotic susceptibility testing in our laboratory, overnight cultures of *M. smegmatis* (ATCC 700084) were started from 4 isolated colonies picked off of Middlebrook 7H10 Agar (Fisher) with a pipette tip and grown in 3 mL of Middlebrook 7H9 Broth (Fisher) at 37°C and 225 rpm. Cultures are then diluted to OD_{600} = 0.002 in 7H9 and 250 μL were combined with an equal volume of nanoparticles (also diluted in 7H9 to the desired concentration). Final volume for each was 500 μL. Samples were incubated for 72 hours at 37°C and 225 rpm, sealed with parafilm to prevent evaporation. Percent inhibition values were determined by serially diluting cultures in 1x PBS and plating on 7H10 agar, grown for 3 days at 37°C and performing colony counts. For specificity tests, similar methods were followed for *E. coli* (ATCC 25922), *K. pneumoniae* (ATCC BAA-2146), methicillin-resistant *S. aureus* (ATCC BAA-44), *M. abscessus* (ATCC 19977) and *M. avium* (MAC104WT) with appropriate broth and agar for each: Mueller-Hinton broth/agar, Mueller-Hinton II (cation-adjusted) broth/agar, or 7H9 broth and 7H10 agar.

2.5.4 Transmission electron microscopy – Nanoparticle measurements

Nanoparticle samples were dropped onto 300-mesh copper grids, and allowed to adhere for 10 – 20 seconds before wicking away the liquid. TEM imaging was conducted using a Philips CM100 microscope with an 80 kV acceleration voltage. Individual nanoparticles within each image were then measured in ImageJ to provide average diameters for different particle types.

2.5.5 Solid-state NMR spectroscopy

Solid-State, Cross-Polarization Magic Angle Spinning (CPMAS), ^{13}C NMR was used to verify the ligands on the gold surface, and to estimate the distribution of the individual ligands on the gold surface. NMR was performed using a Varian INOVA-400 (Agilent Technologies, Inc.) spectrometer operating at 100.63 MHz for ^{13}C observation. The probe incorporates a 5mm Magic Angle Spinning module and coil assembly designed and constructed by Revolution NMR, Inc. (Fort Collins, CO), and capable of spinning up to 13KHz with Zirconia rotors (also from Revolution NMR, Inc.). Spectra were acquired using cross-polarization spin-lock and decoupling Rf fields of 80.5 KHz, and TPPM (Time Proportional Phase Modulation) decoupling was applied during signal acquisition. Chemical shifts were referenced using the absolute, calibrated spectrometer configuration frequency and magnetic field offset, such that the methyl carbons of hexamethylbenzene appear at 17.3 ppm. Samples were prepared by uniformly depositing the nanoparticles onto high surface area silica gel, yielding 20-40% by weight nanoparticles on silica, such that the 90 μL volume of the 5mm rotors was completely filled for stable spinning. Before combination with the silica gel, nanoparticles were washed eight times with filter-sterilized ultrapure water over an amicon filter with

M.W.C.O. of 10 kDa to remove any salt, methanol or free ligands that may be present from the previous steps. Sample spinning frequencies from 10.5-11.5 KHz were employed with the sample oriented at the *magic angle* (54.736 degrees, relative to the magnetic field axis, calibrated using the 79Br spinning sideband pattern of KBR).

To optimize the uniform cross-polarization of ^{1}H magnetization to all ^{13}C nuclei, spectra were acquired using three cross-polarization contact times (1.6, 2.4, and 3.3 mSec), and these were summed to yield the final spectrum. These optimal contact times were determined using variable contact-time experiments, and chosen to obtain uniform excitation across all carbon atoms. Spectra of ligand exchanged samples were the result of 18,432 to 22,272 scans, yielding adequate signal-to-noise ratios to confirm the existence of the ligands on the gold, and allowing the approximate determination of the average ratio of ligands on the particle surface. Due to spectral overlap, integrated intensities were deconvoluted and normalized to the well-resolved CH_3 resonance of thiol 9 (2-diethylamino ethane thiol). By acquiring spectra of LAL-42, and nanoparticles prepared with thiol 8 only (3-mercapto-1-propane sulfonate) or thiol 9 only, it is possible to subtract the intensities from carbons known to correspond to thiols 8 and 9, leaving the intensity contribution from thiol 6. Due to the limited signal-to-noise, these ratios are presented only as best approximations.

2.5.6 Membrane permeability

Protocol for the LIVE/DEAD BacLight Bacterial Viability kit (Invitrogen, L-7007) was followed exactly. In brief, two nucleic acid stains, green-fluorescent SYTO 9 and red fluorescent propidium iodide, are able to penetrate bacterial cell walls differentially and therefore the ratio between them indicates changes in membrane

permeability under varying conditions. Five replicates of incubation with the same batch of LAL-3346 nanoparticles with *M. smegmatis* were averaged in the data presented.

2.5.7 Membrane potential assay and flow cytometry

Protocol for the BacLight Bacterial Membrane Potential kit (Invitrogen, B34950) was also followed exactly. In brief, the carbocyanine dye $DiOC_2(3)$ (3,3'-diethyloxacarbocyanine iodide) fluoresces green in all bacterial cells, but shifts towards red fluorescence in the presence of larger membrane potentials. The positive control CCCP (carbonyl cyanide 3-chlorophenylhydrazone) molecule provided with the kit removes all membrane potential by destroying the proton gradient. In a one-time experiment, *M. smegmatis* was treated with pMBA-only, LAL-3346 nanoparticles (exchanged from the same batch of pMBA nanoparticles also tested) and CCCP, as well as left untreated, then all cultures were stained with $DiOC_2$ and analyzed by a Benton Dickinson FACScan Cytometer with FACScan software. Comparisons of green vs. red fluorescence for each resulted in an indication of the effect each particle type has on the membrane potential.

2.5.8 Transmission electron microscopy – Bacterial images

M. smegmatis was cultured in Middlebrook 7H9 media (Fisher) and adjusted to an OD_{600} = 1. pMBA-only or LAL-3346 nanoparticles were added to the mycobacterial solution at a concentration of 2 μM. After 24 hours, the mixture of mycobacteria and LAL-3346 was centrifuged at 12,000x g for 15 minutes. The cell pellets were resuspended in 1x PBS and centrifuged again. Washed cells were then fixed with 2.5% gluteraldehyde in 0.1 M sodium cacodylate buffer overnight at 4°C and post-fixed with 1% osmium tetraoxide in 0.1 M sodium cacodylate buffer at room temperature for two

hours. After washing with cacodylate buffer, fixed pellets were dehydrated with increasing concentrations of ethanol as follows: 70%, 80%, 90%, 95% and 100% for 10 minutes each, then 100% acetone twice for 10 minutes each time. Dehydrated cell pellets were then infiltrated with a mixture of propylene oxide and Spurr's resin in 1:2, 1:1 and 2:1 volume ratios for 1 hour each, then 100% resin overnight. Finally, pellets were embedded in resin at 60°C for 24 hours to 48 hours. Sections, 60 nm to 70 nm thick, were cut using a Leica UC6 Ultramicrotome and collected onto 300-mesh copper grids. Grids were stained with 2% uranyl acetate and 1% lead citrate solutions. TEM imaging and analysis were conducted using a Philips CM100 microscope with an 80 kV acceleration voltage.

2.6 References

[1] This chapter has been adapted from: Gifford, J.C.; Bresee, J.; Carter, C.J.; Wang, G.; Melander, R.J.; Melander, C.; Feldheim, D.L. *Chem. comm.*, **2014**, *50*, 15860-15863.
[2] Lewis, K. *Nature*, **2012**, *485*, 439-440.
[3] *Addressing the Threat of Drug-Resistant Tuberculosis: A Realistic Assessment of the Challenge.* Workshop Summary. The National Academies Press: 2009.
[4] Center for Disease Control and Prevention: Division of Tuberculosis Elimination, *Latent Tuberculosis Infection: A Guide for Primary Health Care Providers*. http://www.cdc.gov/tb/publications/ltbi/treatment.htm (Accessed April 9, 2015).
[5] World Health Organization, *Global Tuberculosis Report 2013*, pp. 1-306.
[6] Payne, D.J. *Science*, **2008**, *321 (5896)*, 1644-1645.
[7] Center for Disease Control and Prevention. *Antibiotic resistance threats in the United States*, 2013.
[8] World Health Organization. *Tuberculosis Fact Sheet °104.*
[9] World Health Organization. *Multidrug-resistant tuberculosis (MDR-TB)*, October 2013 Update.
[10] Infectious Diseases Society of America. *ID Physicians Call of 10 New Antibiotics by 2020*. http://www.idsociety.org/ID_Physicians_Call_for_10_New_Antibiotics_by_2020.aspx (accessed January 21, 2013).
[11] Spellberg, B.; Guidos, R.; Gilbert, D.; Bradley, J.; Boucher, H. W.; Scheld, W. M.; Bartlett, J. G.; Edwards, J., Jr. *Clin. Infect. Dis.,* **2008,** *46 (2)*, 155-64.
[12] Rowland, K. *Nature News*, **2012**.
[13] Falagas, M.E.; Maraki, S.; Karageorgopoulos, D.E.; Kastoris, A.C.; Mavromanolakis, E.; Samonis, G. *International Journal of Antimicrobial Agents* **2010,** *35 (3)*, 240-243.
[14] Alekshun, M; Levy, S. *Cell***, 2007**, *128 (6)*, 1037-1050.
[15] Drake, J. *Annals of the New York Academy of Sciences*, **1999**, *870*, 100-107.
[16] Martínez, J.L. *Science*, **2008**, *321*, 365-367.
[17] Randall, L.; Woodward, M. *Research in Veterinary Science*, **2002**, *72 (2)*, 87-93.
[18] Cohen, S.; Hachler, H.; Levy, S. *Journal of Bacteriology*, **1993,** *175 (5)*, 1484-1492.
[19] Li, X.; Zhang, L.; Nikaido, H. *Antimicrobial agents and Antibiotics*, **2004**, *48 (7)*, 2415-2423.
[20] Almeida Da Silva, P.; Palomino, J. *Journal of antimicrobial chemotherapy*, **2011**, *66 (7)*, 1417-1430.
[21] Schwarz, S.; Kehrenberg, C.; Doublet, B.; Cloeckaert, A. *FEMS Microbiol. Rev., **2004** 28*, 519–542
[22] Jacoby, G.A.; Munoz-Price, L.S. *N. Engl. J. Med.*, **2005**, *352*, 380–391.
[23] Gillespie, S. *Antimicrobial Agents and Chemotherapy*, **2002**, *46 (2)*, 267-274.
[24] Yao, C.; Zhu, T.; Li, Y.; Zhang, L.; Zhang, B.; Huang, J.; Fu, W. *Clinical Microbiology and Infection*, **2010**, *16 (11)*, 1639-1643.
[25] Sheen, P.; Lozano, K.; Gilman, R.H.; Valenica, H.J.; Loli, S.; Fuentes, P.; Grandjean, L; Zimic, M. *Tuberculosis*, **2013**, *93 (5)*, 515-522.
[26] Miller, L.; Crawford, J.; Shinnick, T. *Antimicrobial Agents and Chemotherapy*, **1994**, *38 (4)*, 805-811.
[27] Zhang, Y. *Annual review of pharmacology and toxicology*, **2005**, *45 (2)*, 529-564.

[28] Nair, J.; Rouse, D.; Bai, G.; Morris, S.L. *Molecular Microbiology*, **1993**, *10 (3)*, 521-527.
[29] Dhas, N.; Raj, C.; Gedanken, A. *Chem. Mater.*, **1998**, *10 (5)*, 1446-1452.
[30] Petroski, J,; Wang, Z.; Green, T.; El-Sayed, M.A. *Journal of Physical Chemistry B*, **1998**, *102 (18)*, 3316-3320.
[31] Jana, N.; Peng, X. *JACS*, **2003**, *125 (47)*, 14280-14281.
[32] Mott, D.; Galkowski, J.; Wang, L.; Luo, J.; Zhong, C.-J. *Langmuir*, **2007**, *23 (10)*, 5740-5745.
[33] Chen, H.; Kou, X.; Yang, Z.; Ni, W.; Wang, J. *Langmuir*, **2008**, *24 (10)*, 5233-5237.
[34] Rai, M.; Yadav, A.; Gade, A. *Biotechnology Advances*, **2009**, *27 (1)*, 76-83.
[35] Jadzinsky, P.D.; Calero, G.; Ackerson, C.J.; Bushnell, D.A.; Kornberg, R.D. *Science*, **2007**, *318* (*5849*), 430-433.
[36] Bresee, J. PhD Dissertation, University of Colorado, 2012.
[37] Wong, A.O.; Heinecke, C.L.; Simone, A.R.; Whetten, R.L.; Ackerson, C.J. *Nanoscale*, **2012**, *4*, 4099-4102.
[38] Bresee, J.; Maier, K.E.; Melander, C.; Feldheim, D.L. *Chem. Comm.,* **2010**, *46 (40)*, 7516-7518.
[39] Bresee, J.; Maier, K.E.; Boncella, A.; Melander, C.; Feldheim, D.L. *Small*, **2011**, *7 (14)*, 2027-2031.
[40] Andrews, J.M. *Journal of antimicrobial chemotherapy*, **2001**, *48 (1)*, 5-16.
[41] Corogeanu, D.; Willmes, R.; Wolke, M.; Plum, G.; Utermöhlen, O.; Krönke, M. *BMC microbiology*, **2012**, *12*, 160-170.
[42] Bresee, J.; Bond, C.M.; Worthington, R.J.; Smith, C.A.; Gifford, J.C.; Simpson, C.A.; Carter, C.J.; Wang, G.; Hartman, J.; Osbaugh, N.A.; Shoemaker, R.K.; Melander, C.; Feldheim, D.L. *JACS*, **2014**, *136 (14)*, 5295-5300.
[43] Smith, C.; Simpson, C.A.; Kim, G.; Carter, C.J.; Feldheim, D.L. *ACS Nano*, **2013**, *7 (5)*, 3991-3996.
[44] Reyrat, J.M.; Kahn, D. *Trends Microbiol.*, **2001**, *9 (10)*, 472-473.
[45] Tyagi, J.S.; Sharma, D. *Trends Microbiol.*, **2002**, *10 (2)*, 68-69.
[46] Singh, A.; Reyrat, J. *Current Protocols in Microbiology*, **2009**, *Chapter 10 (C)*, 1-12.
[47] Reyrat, J.; Kahn, D. *Trends in Microbiology*, **2001**, *9 (10)*, 472-473.
[48] Tyagi, J.; Sharma, D. *Trends in Microbiology*, **2002**, *10 (2)*, 68-69.
[49] Converse, S.; Cox, J. *Journal of Bacteriology*, **2005**, *187 (4)*, 1238-1245.
[50] Anuchin, A.; Mulyukin, A.; Suzina, N.; Duda, V.I.; El-Registan, G.I.; Kaprelyants, A.S. *Microbiology*, **2009**, *155 (Pt 4)*, 1071-1079.
[51] Cordone, A. Audrain, B.; Calabrese, I.; Euphrasie, D.; Reyrat, J.-M. *BMC Microbiology*, **2011**, *11 (1)* , 231-240.
[52] Mishra, A.K.; Driessen, N.N.; Appelmelk, B.J.; Besra, G.S. *FEMS Microbiol. Rev.*, **2011**, *35 (6)*, 1126-1157.
[53] Chaturvedi, V.; Dwivedi, N.; Tripathi, R.; Sinha, S. *J. Gen. Appl. Microbiol.*, **2007**, *53*, 333-337.
[54] Ramon-Garcia, S.; Ng, C.; Anderson, H.; Chao, J.D.; Zheng, X.; Pfeifer, T.; Av-Gay, Y.; Roberge, M.; Thompson, C.J. *Antimicrobial Agents and Chemotherapy*, **2011**, *55 (8)*, 3861-3869.

[55] Murdock, K.; Lin, Y.; Thomas, J.; Lang, Jr., S.A. *Journal of Medicinal Chemistry*, **1978**, *21 (4)*, 403-405.
[56] Lu, T.; Drlica, K. *Journal of Antimicrobial Chemotherapy*, **2003**, *52 (6)*, 1025-1028.
[57] Andries, K.; Verhasselt, P.; Guillemont, J.; Gohlmann, H.W.H.; Neefs, J.-M.; Winkler, H.; Gestel, J.V.; Timmerman, P.; Zhu, M.; Lee, E.; Williams, P.; de Chaffoy, D.; Huitric, E.; Hoffner, S.; Cambau, E.; Truffot-Pernot, C.; Lounis, N.; Jarlier, V. *Science*, **2005**, *307*, 223-227.
[58] Schaaf, T.; Whetten, R. *J. Phys. Chem. B*, **1999**, *103*, 9394-9396.
[59] Hong, S.; Bielinska, A.U.; Mecke, A.; Keszler, B.; Beals, J.L.; Shi, X.; Balogh, L.; Orr, B.G.; Baker, J.R.; Banaszak Holl, M.M. *Bioconjugate Chem.*, **2004**, *15 (4)*, 774-782.
[60] Leroueil, P.R.; Berry, S.A.; Duthie, K.; Han, G.; Rotello, V.M.; McNerny, D.Q.; Baker, J.R.; Orr, B.G.; Holl, M.M.B. *Nano Lett.*, **2008**, *8 (2)*, 420-424.
[61] Novo, D.; Perlmutter, N.G.; Hunt, R.H.; Shapiro, H.M. *Cytometry*, **1999**, *35 (1)*, 55-63.
[62] Williams, R.; Jencks, W.; Westheimer, F. *pKa Data Compilation*. http://research.chem.psu.edu/brpgroup/pKa_compilation.pdf (accessed February 23, 2015).
[63] Stahl, C.; Kubetzko, S; Kaps, I.; Seeber, S.; Engelhardt, H.; Niederweis, M. *Molecular Microbiology*, **2001**, *40 (2)*, 451-464.
[64] Faller, M.; Niederweis, M.; Schultz, G. E. *Science*, **2004**, *303 (1999)*, 1189-1192.
[65] Danilchanka, O.; Pavlenok, M.; Niederweis, M. *Antimicrobial agents and Chemotherapy*, **2008**, *52 (9)*, 3127-3134.
[66] Verma, A.; Uzun, O.; Hu, Y.; Hu, Y.; Han, H.-S.; Watson, N.; Chen, S.; Irvine, D. J.; Stellacci, F. *Nature materials*, **2008**, *7 (July)*, 588-595.
[67] Van Lehn, R. C.; Alexander-Katz, A. *Soft Matter*, **2011**, *7*, 11392-11404.
[68] Van Lehn, R. C.; Atukorale, P. U.; Carney, R. P.; Yang, Y.-S.; Stellacci, F.; Irvine, D. J.; Alexander-Katz, A. *Nano Letters*, **2013**, *13*, 4060-4067.
[69] Van Lehn, R. C.; Ricci, M.; Silva, P.H.J.; Andreozzi, P.; Reguera, J.; Voïtchovsky, K.; Stellacci, F.; Alexander-Katz, A. *Nature communications*, **2014**, *5*, 4482-4493.
[70] Centrone, A.; Penzo, E.; Sharma, M.; Myerson, J. W.; Jackson, A. M.; Marzari, N.; Stellacci, F. *PNAS*, **2008**, *105*, 9886-9891.
[71] Marrakchi, H.; Bardou, F.; Lanéelle, M.-A.; Daffé, M. A Comprehensive Overview of Mycolic Acid Structure and Biosynthesis. In *The Mycobacterial Cell Envelope*; Daffé, M. and Reyrat, J.-M., Ed.; ASM Press: Washington, D.C., 2008; pp 41-62.
[72] Deshayes, C.; Kocíncová, D.; Etienne, G.; Reyrat, J.-M. Glycopeptidolipids: a Complex Pathway for Small Pleiotropic Molecules. In *The Mycobacterial Cell Envelope*; Daffé, M. and Reyrat, J.-M., Ed.; ASM Press: Washington, D.C., 2008; pp 345-366.
[73] Gilleron, M.; Jackson, M.; Nigou, J.; Puzo, G. Structure, Biosynthesis, and Activities of the Phosphatidyl-*myo*-Inositol-Based Lipoglycans. In *The Mycobacterial Cell Envelope*; Daffé, M. and Reyrat, J.-M., Ed.; ASM Press: Washington, D.C., 2008; pp 75-105.
[74] Ackerson, C.; Jadzinsky, P. *Bioconjugate Chem.*, **2010**, *21 (2)*, 214-218.
[75] Franzblau, S.; Witzig, R.; Mclaughlin, J.; Torres, P.; Madico, G.; Hernandez, A.; Degnan, M.T.; Cook, M.B.; Quenzer, V.K.; Ferguson, R.M.; Gilman, R.H. *Journal of Clinical Microbiology*, **1998**, *36 (2)*, 362-366.
[76] Wagner, A.; Mills, K. *Journal of Clinical Microbiology*, **1996**, *34 (7)*, 1672-1676.

[77] Joloba, M.; Bajaksouzian, S.; Jacobs, M. *Journal of Clinical Microbiology*, **2000**, *38 (10)*, 3834-3936.
[78] Riska, P.; Su, Y.; Bardarov, S.; Freundlich, L.; Sarkis, G.; Hatfull, G.; Carriere, C.; Kumar, V.; Chan, J.; Jacobs, Jr., W. *Journal of Clinical Microbiology*, **1999**, *37 (4)*, 1144-1149.
[79] Siddiqi, S.; Libonati, J.; Middlebrook, G. *Journal of Clinical Microbiology*, **1981**, *13 (5)*, 908-912.
[80] Ardito, F.; Posteraro, B.; Sanguinetti, M.; Zanetti, S.; Fadda, G. *Journal of Clinical Microbiology*, **2001**, *39 (12)*, 4440-4444.

CHAPTER 3

Gold Nanoparticle Antibiotics – Part Two

Characterization of *E. coli* Nanoparticle Conjugates

3.1 Introduction & Background

The final chapter of this thesis will focus on further characterization methods employed to gain knowledge of primarily the previously developed *E. coli* nanoparticle conjugates – LAL-32, LAL-33, LAL-42 and LAL-52. First, in order to consider our SMVLD method and the resulting nanoparticle conjugates as potential therapeutics, possible *in vivo* toxicity of the nanoparticles needs to be evaluated. We started to approximate toxic effects on mammalian host cells using sheep's blood cells and two human cell lines in *in vitro* assays. Results from these studies will inform future changes and experiments necessary to treat a host infection, without the host experiencing negative side effects. Measuring mammalian cell lysis in order to assess cell viability in the presence of various nanoparticle conjugates was used as an initial approximation of potential toxicity.[1]

Second, the solid-state NMR spectroscopy method described previously was employed in two other scenarios. Other than the example already provided in Section 2.2.1.3, comparing LAL-33 and LAL-3346, NMR was also used to analyze nanoparticle conjugates LAL-42 and LAL-52. First, LAL-52 displays thiol 11, a thiolated and pegylated histidine, which is significantly larger and more complex than most others in our library. Quantitation of the ligands of LAL-52 demonstrated the ability of our NMR method to analyze complex systems using extensive deconvolution. Second, by

investigating LAL-42, which only has two exchanged ligands instead of three, a thorough and systematic approach was devised to make small alterations in the feed ratio of each thiol. Each variation was tested for its ability to inhibit *E. coli* growth, then a representative few were chosen to study by NMR in order to correlate feed ratio with molar ratio displayed on the nanoparticle surface. This third application of our NMR method will allow us to determine the sensitivity of this method.

3.2 *In vivo* toxicity evaluations[2]

3.2.1 Hemolysis of sheep blood cells and PEG addition effects

The possibility of gold nanoparticle antibiotics being used *in vivo* was considered. The selectivity of the active nanoparticle conjugates for bacterial cells vs. mammalian cells was determined first by conducting blood hemolysis assays on defibrinated sheep's blood cells. Within experimental error (~10%), no hemolysis was observed for LAL-33, LAL-42, and LAL-52 even at the highest concentration tested, 50 μM. Non-linear regression of the hemolysis vs. nanoparticle concentration plot for LAL-3346 yielded a relative EC_{50} of 5.6

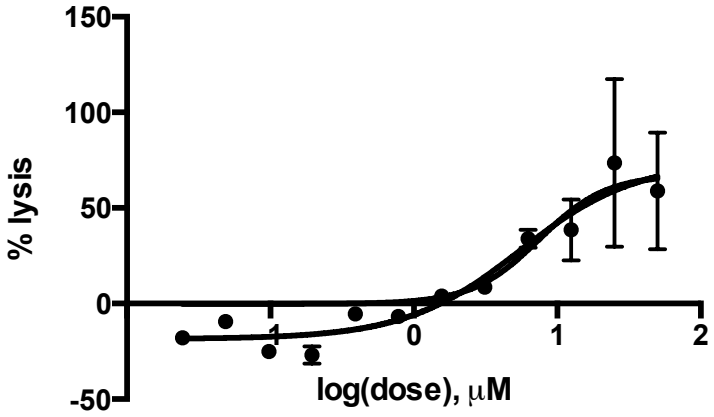

Figure 3.1 EC_{50} curve for the hemolysis of defibrinated sheep's blood cells in the presence of increasing concentrations of LAL-3346. This graph was generated using the nonlinear regression analysis titled "log(agonist) vs. response – variable slope (four parameters)" in GraphPad Prism 6 from triplicate data sets. This analysis determined an EC_{50} of 5.6 μM, with a 95% confidence interval from 1.8 μM to 18 μM. The Hill coefficient was reported as 1.078 and $R^2 = 0.9415$.

μM, shown in Figure 3.1. The equation that GraphPad Prism 6 used for fitting in this analysis is shown below.

$$y = \text{Bottom} + (\text{Top-Bottom}) / (1 + 10^{((\text{LogEC50} - X)(\text{Hill Slope}))})$$

This equation was chosen in order to provide freedom for all four variables, as suggested by the graphing program based on the sufficient number of dating points collected. The values for Top, Bottom, LogEC50 and the Hill Slope are all assigned during the analysis according on the data and its error bars.[3]

The hemolytic index, defined as $EC_{50}/IC_{99.9}$, for LAL-3346 was therefore determined to be 0.93. While the least toxic therapeutics have indices in the thousands, numerous common drugs have much lower therapeutic index values. The Food and Drug Administration (FDA) defines narrow therapeutic index compounds as having a ratio less than 2, described in the Code of Federal Regulations, Title 21, Section 320.33(c).[4] Acetaminophen, the active compound in Tylenol®, has an index between 7.5 and 30, and ethanol, which is regularly consumed in alcoholic beverages, has an index of 10.[5, 6] While both of these compounds are not recommended for regular or extended use due to their toxicity, in specific circumstances, their use is accepted and tolerated. Additionally, we have shown previously that mammalian cell toxicity can be attenuated by nanoparticle PEGylation. In the case of LAL-3346, an exchange of 8:1 thiolated triethylene glycol (PEG_3, Figure 3.2) to gold resulted in an increase in the EC_{50} to 8.2 μM and in the hemolytic index to 1.4, which almost removes LAL-3346 from the category of narrow therapeutic index compounds.

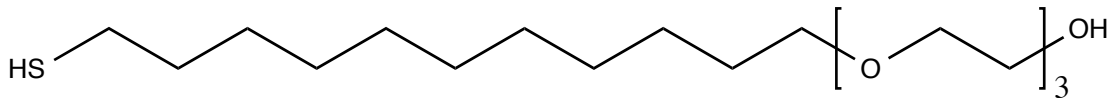

Figure 3.2 The chemical structure of a thiolated triethylene glycol, PEG_3, molecule that was added to LAL-3346 in an attempt to decrease mammalian cell toxicity.

3.2.2 Lysis of human cells

Toxicity assays were also conducted on both Hep G2/2.2.1 liver cell and MRC-5 lung cell lines. First, a colorimetric MTT (3-(4,5-dimethylthiazol-2-yl)-2,5-diphenyltetrazolium bromide) assay was completed with LAL-32 and LAL-52 to determine if nanoparticle conjugates cause liver cell death. No toxicity was observed up to concentrations of 0.8 mM and <40% toxicity was found at the highest concentrations tested, 50 mM. These studies provided some confidence that the LAL-32 and LAL-52 nanoparticles could be non-toxic to the liver *in vivo* at concentrations below 0.8 mM, more than 800 times the $IC_{99.9}$ of either of these conjugates.

The second toxicity experiment performed was with LAL-3346 and MRC-5 lung cells (ATCC CCL-171). While we were unable to obtain a complete dose-response curve (a maximum cell lysis plateau was not reached) even when increasing the nanoparticle concentration to 100 μM, this experiment suggested at least that LAL-3346 is significantly less toxic towards lung cells (EC_{50} > 50 μM, Figure 3.3) than blood cells (EC_{50} = 5.6 μM, refer back to Figure 3.1). All EC_{50} and therapeutic index values are summarized in Table 3.1.

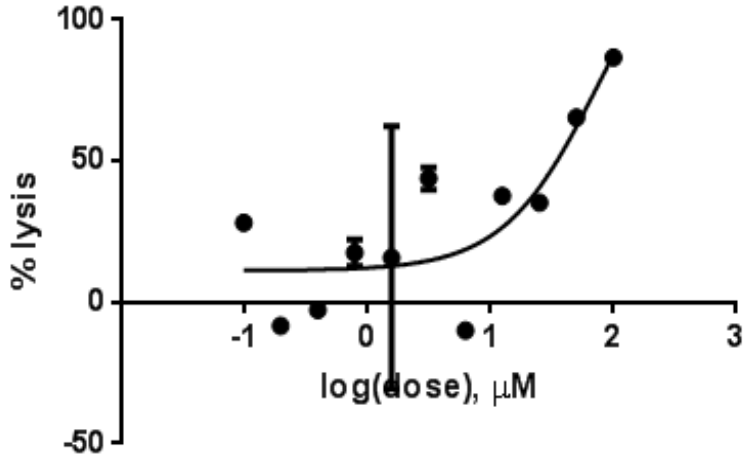

Figure 3.3 EC_{50} graph for the lysis of MRC-5 cells after a 24-hour incubation with LAL-3346. While an EC_{50} value could not be determined from this data, it is estimated to be greater than 50 μM, with 95% confidence, using the "log(agonist) vs. response – variable slope (four parameters)" best fit function in the Graph Pad Prism 6 program. For this fit, the Hill coefficient was 1.128 and R^2 = 0.7015, which again indicates that the data does not really fit the equation used in this analysis.

Table 3.1 Summary of EC_{50} values determined for LAL-3346 against sheep blood cells (with and without an 8:1 addition of thiolated PEG_3) and human lung cells. Therapeutic indexes, the ratio of EC_{50} to $IC_{99.9}$, are also presented.

Cell type	EC_{50}, μM	Index
Blood, sheep	5.6	0.93
	8.2 (w/ 8:1 PEG_3)	1.4
Lung, human	>50	>8.3

The observation that LAL-3346 was less toxic towards human lung cells than sheep's blood cells may be taken advantage of if exploited in an inhalable medication approach. Since TB most commonly manifests in the patient's lungs, our nanoparticle conjugates delivered directly to this location would be much less toxic than having to go through the bloodstream before reaching their desired targets.[7, 8] Numerous inhalable TB

medications are already in use and could provide the basis on which to develop LAL-3346 in the future.[9]

3.3 Ligand quantitation by NMR spectroscopy

3.3.1 Summary of LAL-33 vs. LAL-3346

As discussed in Section 2.2.1.3, the expanded feed ratio version of LAL-33, deemed LAL-3346, has bactericidal activity towards *M. smegmatis*. This comparison was the first application of our ligand quantitation method by solid-state NMR spectroscopy. The results of this experiment confirmed both that all expected ligands are indeed displayed on the surface of the gold nanoparticles and that a shift in the molar ratio of thiol 8 is observed from LAL-33 to LAL-3346.

3.3.2 Application to LAL-52

The second application of the solid-state NMR ligand quantitation method was to LAL-52, which displays pMBA, glutathione (thiol 5), cysteamine (thiol 6) and a thiolated pegylated histidine (3-(1H-imidazol-4-ye)-2-(((5-mercapto-3-oxypentyne)oxy)amino) propanoic acid, thiol 11). This conjugate has a similar growth inhibition efficacy towards *E. coli* as LAL-32, 250 nM; however, it displays two of the largest, amino acid-like thiols (5 & 11) from our original library, making it a particularly interesting and complex case for NMR.

While spectra from LAL-52 required significantly more work deconvoluting peaks to obtain information about individual ligands, we were still able to approximate the molar ratios of each ligand present. In this case, spectral features were attributed to thiol 11 first by obtaining a spectrum of thiol 11 only nanoparticles (a spectrum for

pMBA-only nanoparticles had previously been acquired for the LAL-33 vs. LAL-3346 analysis). Using the information gained by the spectra for pMBA-only, thiol 11 only and LAL-52, overlapping peaks and contributing carbons were deduced. First, all intensity specific to thiol 11 was subtracted from the entire spectrum of LAL-52, leaving only the peak intensity arising from pMBA, thiol 5 and thiol 6. The remaining peak intensity in the aromatic carbon region of the spectrum must be due to pMBA, as neither thiol 5 nor 6 contains aromatic carbons. This resulted in 3.3 pMBA molecules per thiol 11. This quantity of pMBA can then be subtracted from the remaining peak intensity in the carbonyl carbon region of the spectrum, resulting in 7.1 carbonyls due to thiol 5 as only pMBA and thiol 5 contribute to carbonyl intensity. Since thiol 5 has 4 carbonyls per molecule, dividing 7.1 by four gives 1.8 thiol 5 molecules per thiol 11. Finally, by subtracting the peak intensity due to both thiol 5 and thiol 11 from the alkyl carbon region of the spectrum and dividing the remaining quantity by two for the two alkyl carbons of thiol 6, it was determined that the molar ratio of thiol 6 was 7.4 per thiol 11 on LAL-52. The spectra for thiol 11-only and LAL-52 nanoparticles are shown in Figures 4.4 and 4.5, and a summary of the molar ratios is included in Table 3.2.

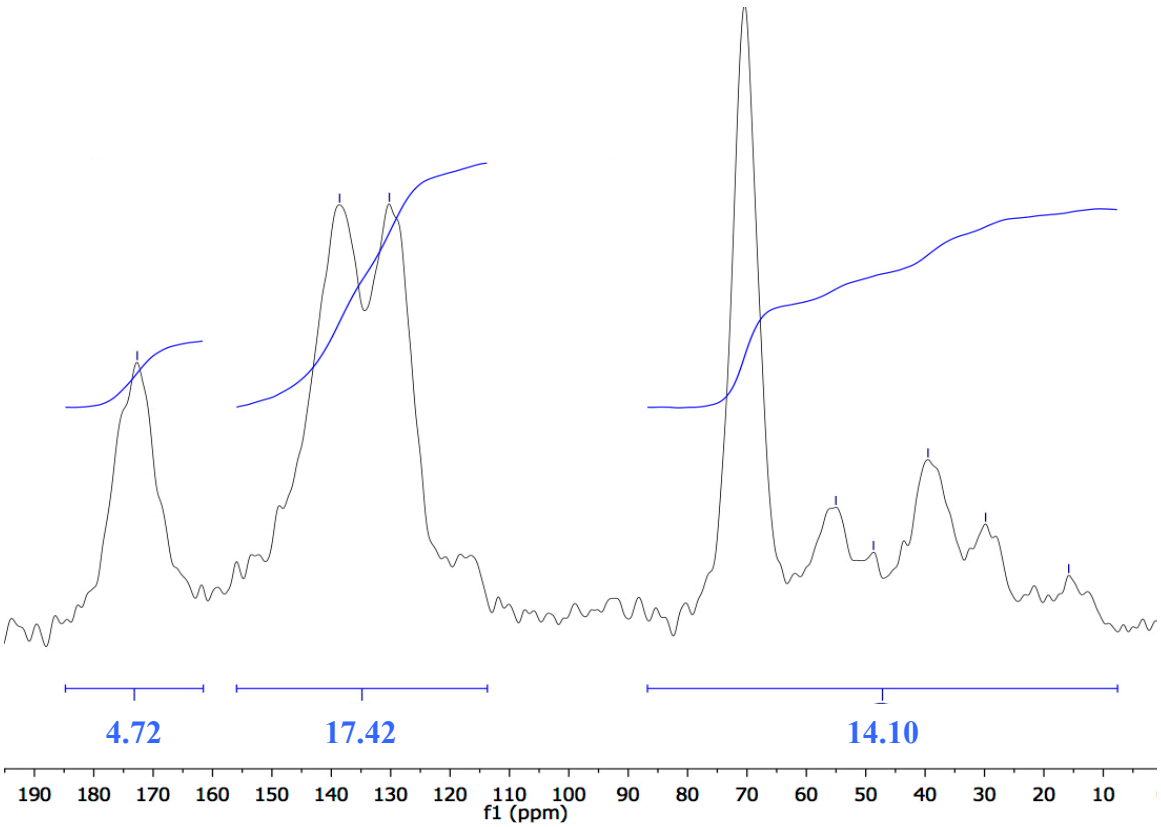

Figure 3.4 ^{13}C CPMAS NMR spectrum of thiol 11-only nanoparticles on SiO_2 (40% nanoparticles by weight). The integrated intensities between 170-180 ppm correspond to carbonyl carbons, between 120-150 ppm correspond to aromatic carbons and 20-80 ppm correspond to alkyl carbons.

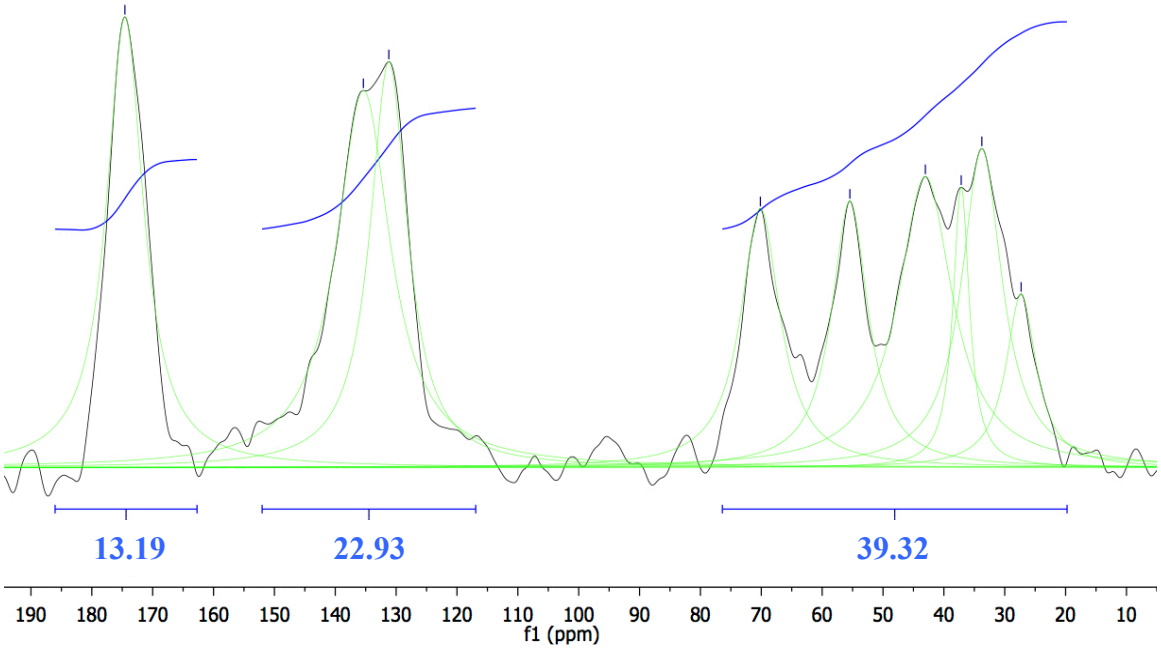

Figure 3.5 ^{13}C CPMAS NMR spectrum of LAL-52 nanoparticles on SiO_2 (40% nanoparticles by weight). The integrated intensities between 170-180 ppm correspond to carbonyl carbons, between 120-150 ppm correspond to aromatic carbons and 20-80 ppm correspond to alkyl carbons.

Table 3.2 Summary of feed ratios input into exchange reactions and molar ratios of resulting LAL-52 nanoparticles as determined by solid-state NMR ligand quantitation method. The molar ratio values have been normalized to pMBA for comparison purposes.

	Thiol 5	Thiol 6	Thiol 11	pMBA
Feed Ratio	34	46	17	N/A
Molar Ratio	0.5	2.2	0.3	1.0

3.3.3 Application to LAL-42

3.3.3.1 Result of expanded feed ratios

In order to further explore the expanded feed ratio space available for each nanoparticle conjugate, numerous manipulations were made to LAL-42. This nanoparticle was chosen as it is the simplest active system that we have developed, displaying pMBA and only two exchanged ligands (thiol 6 and thiol 8). As listed in Table 3.4, the original feed ratio for LAL-42 was 46x gold for thiol 6 and 34x gold for thiol 8.

Feed ratios of each thiol were varied independently (Tables 3.3 and 3.4), with most efficacy observed at lower ratios of thiol 6 and higher ratios of thiol 8 (i.e. approximately a 1:1 or greater molar ratio of thiol 8 to thiol 6); the resulting change in growth inhibition as a function of the ratio of thiol 8 to thiol 6 is graphed in Figure 3.6. These results have again confirmed the importance of both ligand identity and feed ratio, as well as indicated that function may simply depend on the presence of thiol 6 at a specific threshold concentration, while the amount of thiol 8 seems to more directly dictate the growth inhibition observed. Unfortunately, above a feed ratio of about 63x thiol 8 to gold, etching of the nanoparticles during exchange reactions dramatically decreased the yield of the exchanged nanoparticles. This capped the range of nanoparticles able to be tested against *E. coli*.

Table 3.3 Expanded feed ratios of LAL-42 tested for growth inhibition of *E. coli*. In this set, the feed ratio of thiol 8 was held constant at 34x gold.

Version of LAL-42	Feed Ratio, Thiol 6	Feed Ratio, Thiol 8
original	46	34
A	53	34
B	49	34
C	46	34
D	43	34
E	39	34
F	36	34

Table 3.4 Expanded feed ratios of LAL-42 tested from growth inhibition of *E. coli* in which the feed ratio of thiol 6 was held constant at 34x gold.

Version of LAL-42	Feed Ratio, Thiol 6	Feed Ratio, Thiol 8
i	34	63
a	34	53
b	34	49
c	34	46
d	34	43
e	34	39
f	34	36
g	34	32
h	34	29

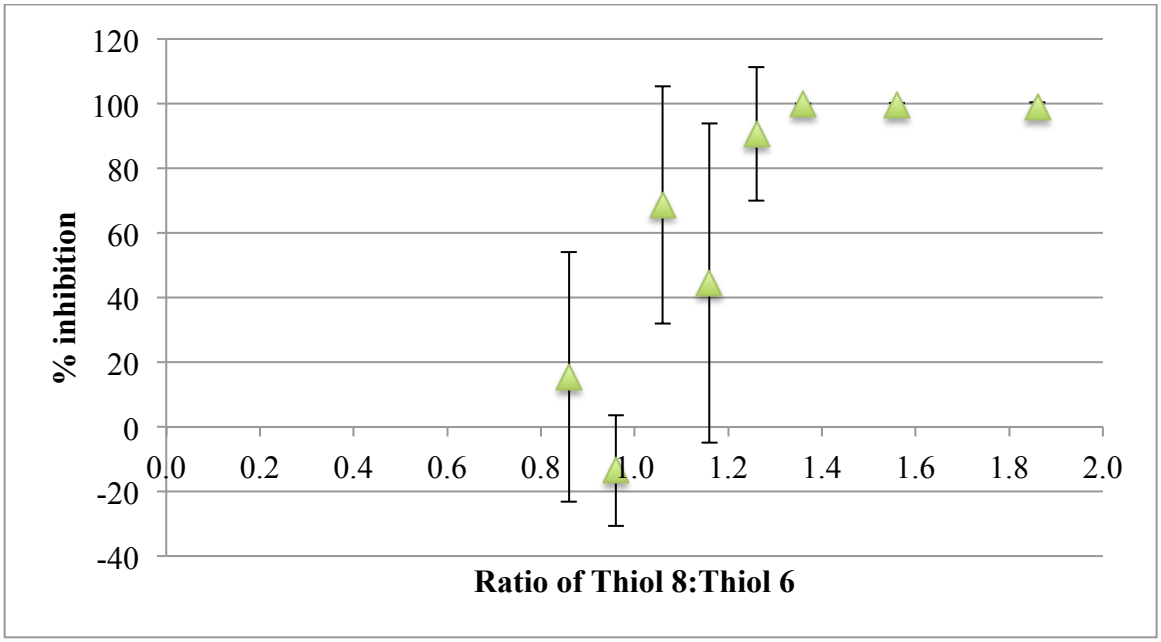

Figure 3.6 *E. coli* growth inhibition curve as a result of incubation with 1 μM feed ratio variations of LAL-42. Each error bar represents the standard deviation of at least three replicates.

3.3.3.2 Testing method sensitivity

The LAL-42 nanoparticle conjugate variations will then be employed as a sensitivity test of our solid-state NMR spectroscopy method for ligand quantitation. Small changes in feed ratios have already been shown to result in large alterations in growth inhibition; the goal is to determine if our NMR method as developed thus far can detect these slight variations in feed ratio and provide evidence of shifts in the quantity of thiols on nanoparticles after ligand exchange. Four representative LAL-42 variations were chosen to correlate changes in feed ratios, growth inhibition efficacy and ligand quantitation: LAL-42i, LAL-42c, LAL-42f and LAL-42h. These nanoparticle conjugates will be prepared for solid-state NMR as previously described, resulting in 25% to 40% nanoparticles by weight evenly distributed on silica, and will be analyzed by NMR spectroscopy.

3.4 Conclusions and future directions

Mammalian cell toxicity was determined for four different nanoparticles by first measuring hemolysis of sheep's blood cells. LAL-33, LAL-42 and LAL-52 all showed no hemolysis up to 50 μM, the highest concentration tested. LAL-3346, on the other hand, resulted in an EC_{50} of 5.6 μM; this value could be raised to 8.2 μM upon the addition of PEG_3 in an 8:1 feed ratio with gold. The addition of polyethylene glycol had previously been shown to decrease *in vivo* toxicity, an aspect that was replicated by its addition to LAL-3346. This improved EC_{50} unfortunately still results in a hemolytic index of 1.4, which is below the narrow therapeutic index as defined by the FDA.

However, the EC_{50} of LAL-3346 towards MRC-5 human lung cells was determined to be greater than 50 μM (a complete dose-response curve could not be obtained up to 100 μM nanoparticles). This implied that LAL-3346 is substantially less toxic towards lungs cells than blood cells, possibly presenting an inhalable drug delivery option for this nanoparticle conjugate. As a TB targeted-antibiotic, inhalable drugs are a common and reasonable method of treatment.

Details of a solid-state NMR spectroscopy method to quantify relative amounts of ligands displayed on the surface of the nanoparticles after exchange has also been fully developed and three different test cases were designed. LAL-33 and LAL-3346 were compared to correlate a feed ratio change of thiol 8 and thiol 9 to the molar ratio of each ligand on the two nanoparticles. These results were expanded to test ligand composition complexity using LAL-52, as well as molar ratio sensitivity via variations of LAL-42. Since LAL-52 displays two large amino acid-based ligands (glutathione, 5, and thiolated histidine, 11), this conjugate provided an example in which deconvolution of a relatively

complicated spectrum with numerous overlapping peaks was necessary. We successfully determined molar quantities for each ligand present by step-wise removal of intensity correlating to each ligand in specific functional group areas on the spectrum.

Finally, numerous variations of LAL-42 were created, the growth inhibition as a result of these nanoparticle conjugates was plotted, and four representatives were chosen to study further via ligand quantitation by NMR. These nanoparticles are currently being produced in large batches and will be submitted to the departmental NMR facility as soon as possible. The minute changes in feed ratio characterized by the differences in each of these nanoparticles will provide an idea as to the sensitivity of what our NMR method can detect.

3.5 Experimental

3.5.1 Place exchange reactions with PEG_3

Thiolated triethylene glycol was added in a molar feed ratio of 8:1 thiol:gold from 20 mM frozen stocks in water to post-exchanged LAL-3346 nanoparticles. These new, second-generation exchanges were taken through the exact same steps as previously described. Reactions were shaken at 19°C for 24 hours. The exchanged nanoparticle products were then harvested by the addition of 2 mL 5 M NaCl and 9 mL methanol. Precipitated nanoparticles were collected by centrifugation at 3,200x g for 5 minutes. Pellets were resuspended in 4-6 drops filter-sterilized ultrapure H_2O then precipitated again with 0.5 mL 5 M NaCl and approximately 8 mL methanol. Centrifugation was repeated and pellets were dried overnight then resuspended and washed eight times with filter-sterilized ultrapure H_2O over 10k M.W.C.O. filters (Millipore). Purified

nanoparticles are quantified as before, using UV-visible spectroscopy and a ε_{510} of 409,440 $M^{-1}cm^{-1}$.

3.5.2 Hemolysis assays

Mechanically-defibrinated sheep's blood (Hemostat Labs) was incubated with our nanoparticle conjugates for up to 24 hours. An aliquot of blood cells was washed three times with 1x PBS and then used in a 1:10 dilution. Nanoparticles (from the same batch) were added to blood cells in a range of concentrations, each in triplicate. After 24 hours, the remaining cells were washed with 1x PBS, lysed with 0.1% Triton and the release of heme was measured by UV-visible spectroscopy at 410 nm.

3.5.3 Mammalian cell culture

HepG2/2.2.1 liver cells (ATCC CRL-11997) and MRC-5 lung cells (ATCC CCL-171) were cultured in Corning flasks with DMEM or EMEM, respectively, supplemented with 10% FBS and 1% penicillin/strepavidin at 37°C and 5% CO_2. The media was changed to calcium and magnesium-free 1X D-PBS with 10% FBS for all nanoparticle assays.

3.5.4 MTT assays

Cell viability assays were conducted using an MTT kit (Biotium #30006) as indicated by manufacturer's instructions. Briefly, cells were seeded at 2.5 x 10^5 cells/well in 96 well plates in 1X D-PBS with 10% FBS. After 30 minutes, test compounds in triplicate were added to the cells and incubated at 37°C and 5% CO_2 for 24 hrs. Cells in media only were used as a negative control and 100% survival, whereas 0.1% Triton-X was added to cells as a positive control and zero percent survival. After the 24-hour

incubation, cells were washed two times with 1X D-PBS to remove excess nanoparticles and 100 μL of DMEM was added to the surviving cells. Ten microliters of MTT reagent was added to each well and the cells were incubated at 37°C, in 5% CO_2, for 4 hrs. Finally, 200 μL of DMSO was added to the media to dissolve the formazan salt product. Absorbance measurements at 595 nm were acquired and percent survival was determined. All experiments performed used cells from the same starting population and nanoparticles were a single preparation.

3.5.5 Solid-state NMR spectroscopy

Sample preparation and solid-state, CPMAS ^{13}C NMR spectroscopy was done in the same manner as previously described in section 3.5.5.

3.6 References

[1] Riss, T.L.; Moravec, R.A.; Niles, A.L.; Benink, H.A.; Worzella, T.J.; Minor, L. *Assay Guidance Manual*, Eli Lilly & Co.: Bethesda, MD, 2004.

[2] This section has been adapted from my contribution to: Bresee, J.; Bond, C.M.; Worthington, R.J.; Smith, C.A.; Gifford, J.C.; Simpson, C.A.; Carter, C.J.; Wang, G.; Hartman, J.; Osbaugh, N.A.; Shoemaker, R.K.; Melander, C.; Feldheim, D.L. *JACS*, **2014**, *136 (14)*, 5295-5300.

[3] GraphPad Software. Equation: log(agonist) vs. response – Variable slope. http://www.graphpad.com/guides/prism/6/curve-fitting/index.htm?reg_dr_stim_variable.htm (Accessed April 13, 2015).

[4] Food and Drug Administration. *Code of Federal Regulations*; 21CFR320.33(c), 2014.

[5]Rumack B.H.; Matthew, H. Acetaminophen poisoning and toxicity. *Pediatrics*. 1975; 55:871-876.

[6] Gable, R. *Addiction*. **2004**, *99 (6)*, 686-696.

[7]U.S. National Library of Medicine. Pulmonary Tuberculosis. http://www.nlm.nih.gov/medlineplus/ency/article/000077.htm (accessed February 10th, 2015).

[8] Lawlor, C.; O'Sullivan, M.P.; Rice, B.; Dillon, P.; Gallagher, P.J.; O'Leary, S.; Shoyele, S.; Keane, J.; Cryan, S.-A. *J. Mater. Sci*. **2012**, *23*, 89-98.

[9] Misra, A.; Hickey, A.J.; Rossi, C.; Borchard, G.; Terada, H.; Makino, K.; Fourie, P.B.; Colombo, P. *Tuberculosis*, **2011**, *91 (1)*, 71-81.

Bibliography

Ackerson, C.; Jadzinsky, P. *Bioconjugate Chem.*, **2010**, *21 (2)*, 214-218.

Addressing the Threat of Drug-Resistant Tuberculosis: A Realistic Assessment of the Challenge. Workshop Summary. The National Academies Press: 2009.

Aisen, P.; Enns, C.; Wessling-Resnick, M. *The International Journal of Biochemisty & Cell Biology*, **2001**, *33 (10)*, 940-959.

Aizenberg, J.; Tkachenko, A.; Weiner, S.; Addadi, L.; Hendler, G. *Nature*, **2001**, *412 (6849)*, 819-822.

Alekshun, M; Levy, S. *Cell***, 2007**, *128 (6)*, 1037-1050.

Almeida Da Silva, P.; Palomino, J. *Journal of antimicrobial chemotherapy*, **2011**, *66 (7)*, 1417-1430.

Almirón, M.; Link, A.J.; Furlong, D.; Kolter, R. *Genes & Development*, **1992**, *6*, 2646-2654.

Amptek, Inc. Periodic Table and X-Ray Emission Line Lookup Chart. http://www.amptek.com/periodic-table-and-x-ray-emission-line-lookup-chart/ (Accessed April 8, 2015).

Amptek, Inc. What is XRF?. http://www.amptek.com/xrf/ (Accessed April 8, 2015).

Anderson, D.E.; Gueiros-Filho, F.J.; Erickson, H.P. *J. Bacteriol.* **2004**, *186 (17)*, 5775-5781.

Andrews, J.M. *Journal of antimicrobial chemotherapy*, **2001**, *48 (1)*, 5-16.

Andries, K.; Verhasselt, P.; Guillemont, J.; Gohlmann, H.W.H.; Neefs, J.-M.; Winkler, H.; Gestel, J.V.; Timmerman, P.; Zhu, M.; Lee, E.; Williams, P.; de Chaffoy, D.; Huitric, E.; Hoffner, S.; Cambau, E.; Truffot-Pernot, C.; Lounis, N.; Jarlier, V. *Science*, **2005**, *307*, 223-227.

Anuchin, A.; Mulyukin, A.; Suzina, N.; Duda, V.I.; El-Registan, G.I.; Kaprelyants, A.S. *Microbiology*, **2009**, *155 (Pt 4)*, 1071-1079.

Arakaki, A.; Masuda, F.; Amemiya, Y.; Tanaka, T.; Matsunaga, T. *Journal of Colloid and Interface Science*, **2010**, *343*, 65-70.

Ardito, F.; Posteraro, B.; Sanguinetti, M.; Zanetti, S.; Fadda, G. *Journal of Clinical Microbiology*, **2001**, *39 (12)*, 4440-4444.

Atkins, P.; de Paula, J. *Elements of Physical Chemistry*, 4th ed.; Oxford University Press: New York, 2005.

Baker, C.J.; Mock, N.M.; Roberts, D.P.; Deahl, K.L.; Hapeman, C.J.; Schmidt, W.F.; Kochansky, J. *Free Radical Biology and Medicine*, **2007**, *43 (9)*, 1322-1327.

Barry, B. *Photochemistry and photobiology*, **1993**, *57 (1)*, 179-188.

Berges, J.; De Oliveira, P.; Fourre, I.; Houee-Levin, C. *Journal of Physical Chemistry B*, **2012**, *116 (31)*, 9352-9362.

Betzig, E. *Opt. Lett.* **1995**, *20*, 237-239.

Betzig, E.; Patterson, G.H.; Sougrat, R.; Lindwasser, O.W.; Olenych, S.; Bonifacino, J.S.; Davidson, M.W.; Lippincott-Schwartz, J.; Hess, H.F. *Science*, **2006**, *313 (September)*, 1642-1645.

Bozzi, M.; Mignogna, G.; Stefanini, S.; Barra, D.; Longhi, C.; Valenti, P.; Chiancone, E. *J. Biol. Chem*. **1997**, *272 (6)*, 3259-3265.

Braun, V.; Braun, M. *FEBS Letters*, **2002**, *529*, 78-85.

Bresee, J.; Bond, C.M.; Worthington, R.J.; Smith, C.A.; Gifford, J.C.; Simpson, C.A.; Carter, C.J.; Wang, G.; Hartman, J.; Osbaugh, N.A.; Shoemaker, R.K.; Melander, C.; Feldheim, D.L. *JACS*, **2014**, *136 (14)*, 5295-5300.

Bresee, J.; Maier, K.E.; Boncella, A.; Melander, C.; Feldheim, D.L. *Small*, **2011**, *7 (14)*, 2027-2031.

Bresee, J.; Maier, K.E.; Melander, C.; Feldheim, D.L. *Chem. Comm.,* **2010**, *46 (40)*, 7516-7518.

Bresee, J. PhD Dissertation, University of Colorado, 2012.

Buddelmeijer, N.; Beckwith, J. *Current Opinion in Microbiology*, **2002**, *5*, 553-557.

California State University, Dominguez Hills. Selected Solubility Products and Formation Constants at 25°C. http://www.csudh.edu/oliver/chemdata/data-ksp.htm (accessed April 7, 2015).

Carrondo, M. *EMBO Journal*, **2003**, *22 (9)*, 1959-1968.

Carter, C.J.; Ackerson, C.J.; Feldheim, D.L. *ACS Nano*, **2010**, *4 (7)*, 3883-3888.

Ceci, P.; Chiancone, E.; Kasyutich, O.; Bellapadrona, G.; Castelli, L.; Fittipaldi, M.; Gatteschi, D.; Innocenti, C.; Sangregorio, C. *Chem. Eur. J.*, **2010**, *16*, 709-717.

Center for Disease Control and Prevention. *Antibiotic resistance threats in the United States*, 2013.

Center for Disease Control and Prevention: Division of Tuberculosis Elimination, *Latent Tuberculosis Infection: A Guide for Primary Health Care Providers*. http://www.cdc.gov/tb/publications/ltbi/treatment.htm (Accessed April 9, 2015).

Centrone, A.; Penzo, E.; Sharma, M.; Myerson, J. W.; Jackson, A. M.; Marzari, N.; Stellacci, F. *PNAS*, **2008**, *105*, 9886-9891.

Chaturvedi, V.; Dwivedi, N.; Tripathi, R.; Sinha, S. *J. Gen. Appl. Microbiol.*, **2007**, *53*, 333-337.

Chen, C.; Rosi, N. *Angewandte Chemie International Edition*, **2010**, *49 (11)*, 1924-1942.

Chen, H.; Kou, X.; Yang, Z.; Ni, W.; Wang, J. *Langmuir*, **2008**, *24 (10)*, 5233-5237.

Chen, Y.; Erickson, H.P. *J. Biol. Chem.* **2005**, *280*, 22549-22554.

Cohen, S.; Hachler, H.; Levy, S. *Journal of Bacteriology*, **1993,** *175 (5)*, 1484-1492.

Converse, S.; Cox, J. *Journal of Bacteriology*, **2005**, *187 (4)*, 1238-1245.

Cordone, A. Audrain, B.; Calabrese, I.; Euphrasie, D.; Reyrat, J.-M. *BMC Microbiology*, **2011**, *11 (1)* , 231-240.

Corogeanu, D.; Willmes, R.; Wolke, M.; Plum, G.; Utermöhlen, O.; Krönke, M. *BMC microbiology*, **2012**, *12*, 160-170.

Cuculic, V.; Mlakar, M.; Branica, M. *Electroanalysis*, **1998**, *10 (12)*, 852-856.

Currey, J.D. Bones: Structure and Mechanics; Princeton University Press: Princeton, New Jersey, 2006.

Danilchanka, O.; Pavlenok, M.; Niederweis, M. *Antimicrobial agents and Chemotherapy*, **2008**, *52 (9)*, 3127-3134.

Davis, I. *Biochemical Society Transactions*, **2009**, *37 (5)*, 1042-1044.

DeFelippis, M.R.; Murthy, C.P.; Faraggi, M.; Klapper, M.H. *Biochemistry*, **1989**, *28 (11)*, 4847-4853.

Deshayes, C.; Kocíncová, D.; Etienne, G.; Reyrat, J.-M. Glycopeptidolipids: a Complex

Pathway for Small Pleiotropic Molecules. In *The Mycobacterial Cell Envelope*; Daffé, M. and Reyrat, J.-M., Ed.; ASM Press: Washington, D.C., 2008; pp 345-366.

Dhas, N.; Raj, C.; Gedanken, A. *Chem. Mater.*, **1998**, *10 (5)*, 1446-1452.

Dickerson, M.B.; Naik, R.R.; Stone, M.O.; Cai, Y.; Sandhage, K.H. *Chem. Comm.* **2004**, 1776-1777.

Drake, J. *Annals of the New York Academy of Sciences*, **1999**, *870*, 100-107.

Falagas, M.E.; Maraki, S.; Karageorgopoulos, D.E.; Kastoris, A.C.; Mavromanolakis, E.; Samonis, G. *International Journal of Antimicrobial Agents* **2010,** *35 (3)*, 240-243.

Faller, M.; Niederweis, M.; Schultz, G. E. *Science*, **2004**, *303 (1999)*, 1189-1192.

Fecenko, C.; Meyer, T.; Thorp, H. *JACS*, **2006**, *25*, 11020-11021.

Flynn, C.M. Jr. *Chemical Reviews*. **1984**, 31-41.

Food and Drug Administration. *Code of Federal Regulations*; 21CFR320.33(c), 2014.

Franceschini, S.; Ceci, P.; Alaleona, F.; Chiancone, E.; Ilari, A; *FEBS*. **2006**, *273*, 4913-4928.

Franzblau, S.; Witzig, R.; Mclaughlin, J.; Torres, P.; Madico, G.; Hernandez, A.; Degnan, M.T.; Cook, M.B.; Quenzer, V.K.; Ferguson, R.M.; Gilman, R.H. *Journal of Clinical Microbiology*, **1998**, *36 (2)*, 362-366.

Gable, R. *Addiction*. **2004**, *99 (6)*, 686-696.

Gayer, K.; Woontner, L. *Journal of Physical Chemistry*, **1956**, *57 (13)*, 1-3.

Giepmans, B.N.G. *Histochem. Cell. Biol.* **2008**, *130*, 211-217.

Gifford, J.C.; Bresee, J.; Carter, C.J.; Wang, G.; Melander, R.J.; Melander, C.; Feldheim, D.L. *Chem. comm.*, **2014**, *50*, 15860-15863.

Gilleron, M.; Jackson, M.; Nigou, J.; Puzo, G. Structure, Biosynthesis, and Activities of the Phosphatidyl-*myo*-Inositol-Based Lipoglycans. In *The Mycobacterial Cell Envelope*; Daffé, M. and Reyrat, J.-M., Ed.; ASM Press: Washington, D.C., 2008; pp 75-105.

Gillespie, S. *Antimicrobial Agents and Chemotherapy*, **2002**, *46 (2)*, 267-274.

Goreau, T.F. *Annals of the New York Academy of Sciences*, **1963**, *109*, 127.167.

Grady, J.; Chasteen, N.; Harris, D. *Analytical Biochemistry*, **1988**, *173 (1)*, 111-115.

GraphPad Software. Equation: log(agonist) vs. response – Variable slope. http://www.graphpad.com/guides/prism/6/curve-fitting/index.htm?reg_dr_stim_variable.htm (Accessed April 13, 2015).

Gustafsson, M. *Journal of microscopy*, **2000**, *198 (January)*, 82-87.

Guzman, L.-M.; Belin, D.; Carson, M.J.; Beckwith, J. *J Bacteriol.* **1995**, *177 (14)*, 4121-4130.

Harriman, A. *Journal of Physical Chemistry*, **1987**, *91 (3)*, 6102-6104.

Heintzmann, R.; Ficz, G. *Briefings in Functional Genomics and Proteomics*, **2006**, *5 (4)*, 289-301.

Held, D.; Yaeger, K.; Novy, R. *Novagen: inNovations*, **2004**, *19*, 17-19.

Hem, J.D. *Geological Society of America Bulletin*, **1972**, *February*, 433-450.

Hong, S.; Bielinska, A.U.; Mecke, A.; Keszler, B.; Beals, J.L.; Shi, X.; Balogh, L.; Orr, B.G.; Baker, J.R.; Banaszak Holl, M.M. *Bioconjugate Chem.*, **2004**, *15 (4)*, 774-782.

Ilari, A.; Latella, M.C.; Ceci, P.; Ribacchi, F.; Su, M.; Giangiacomo, L.; Stefanini, S.; Chasteen, N.D.; Chiancone, E. *Biochemistry*. **2005**, *44*, 5579-5587.

Infectious Diseases Society of America. *ID Physicians Call of 10 New Antibiotics by 2020*. http://www.idsociety.org/ID_Physicians_Call_for_10_New_Antibiotics_by_2020.aspx (accessed January 21, 2013).

Iron (II) sulfate heptahydrate; MSDS F7002; Sigma Aldrich: St. Louis, MO, Feb 27, 2015.

Jacoby, G.A.; Munoz-Price, L.S. *N. Engl. J. Med.*, **2005**, *352*, 380–391.

Jadzinsky, P.D.; Calero, G.; Ackerson, C.J.; Bushnell, D.A.; Kornberg, R.D. *Science*, **2007**, *318* (*5849*), 430-433.

Jambor, J.L.; Dutrizac, J.E. *Chemical Reviews*. **1998**, 2549-2587.

Jana, N.; Peng, X. *JACS*, **2003**, *125 (47)*, 14280-14281.

Jensen, G.J.; Briegel, A. *Curr. Op. Microbiol.* **2007**, *17*, 260-267.

Jolivet, J.-P.; Chanéac, C.; Tronc, E. *Chem. Comm.* **2003**, 481-487.

Joloba, M.; Bajaksouzian, S.; Jacobs, M. *Journal of Clinical Microbiology*, **2000**, *38 (10)*, 3834-3936.

Khlebnikov, A.; Skaug, T.; Keasling, J.D. *Journal of Industrial Microbiology and Biotechnology*, **2002**, *29*, 34-37.

Kidane, T.; Sauble, E.; Linder, M. *American Journal of Physiology: Cell Physiology*, **2006**, *291 (3)*, C445-C455.

Klar, T.; Jakobs, S.; Dyba, M.; Egnar, A.; Hell, S.W. *PNAS*, **2000**, *97 (15)*, 8206-8210.

Komeili, A.; Li, Z.; Newman, D.K.; Jensen, G.J. *Science*, **2006**, *311 (5758)*, 242-245.

Krewulak, K.; Vogel, H. *Biochimica et Biophysica Acta (BBA)*, **2008**, *1778 (9)*, 1781-1804.

Lawlor, C.; O'Sullivan, M.P.; Rice, B.; Dillon, P.; Gallagher, P.J.; O'Leary, S.; Shoyele, S.; Keane, J.; Cryan, S.-A. *J. Mater. Sci*. **2012**, *23*, 89-98.

Leroueil, P.R.; Berry, S.A.; Duthie, K.; Han, G.; Rotello, V.M.; McNerny, D.Q.; Baker, J.R.; Orr, B.G.; Holl, M.M.B. *Nano Lett.*, **2008**, *8 (2)*, 420-424.

Lewis, K. *Nature*, **2012**, *485*, 439-440.

Li, X.; Zhang, L.; Nikaido, H. *Antimicrobial agents and Antibiotics*, **2004**, *48 (7)*, 2415-2423.

Li, Z.; Jensen, G.J. *Curr. Op. Microbiol.* **2009**, *12*, 333-340.

Li, Z.; Trimbler, M.J.; Brun, Y.V.; Jensen, G.J. *The EMBO Journal*, **2007**, *26*, 4694-4708.

Link, S.; Beeby, A.; FitzGerald, S.; El-Sayad, M.A.; Schaaff, T.G.; Whetten, R.L. *J. Phys. Chem. B*. **2002**, *106*, 3410-3415.

Link, S.; El-Sayed, M. A. *Journal of Physical Chemistry B*, **1999**, *103 (40)*, 8410-8426.

Lu, T.; Drlica, K. *Journal of Antimicrobial Chemotherapy*, **2003**, *52 (6)*, 1025-1028.

Malone, S.A.; Lewin, A.; Kilic, A.; Svistunenko, D.A.; Cooper, C.E.; Wilson, M.T.; LeBrun, N.E.; Spiro, S.; Moore, G.R. *J. Am. Chem. Soc.* **2003**, *126*, 496-504.

Marambio-Jones, C.; Hoek, E.M.V. *J. Nanopart. Res.* **2010**, *12*, 1531-1551.

Marrakchi, H.; Bardou, F.; Lanéelle, M.-A.; Daffé, M. A Comprehensive Overview of Mycolic Acid Structure and Biosynthesis. In *The Mycobacterial Cell Envelope*; Daffé, M. and Reyrat, J.-M., Ed.; ASM Press: Washington, D.C., 2008; pp 41-62.

Martínez, J.L. *Science*, **2008**, *321*, 365-367.

Matsunaga, T.; Sakaguchi, T.; Tadakoro, F. *Appl. Microbiol. Biotechnol*. **1991**, *35 (5)*, 651-655.

Miller, L.; Crawford, J.; Shinnick, T. *Antimicrobial Agents and Chemotherapy*, **1994**, *38 (4)*, 805-811.

Milligan, J; Aguilera, J.; Ly, A.; Tran, N.Q.; Hoang, O.; Ward, J.F. *Nucleic Acids Research*, **2003**, *31 (21)*, 6258-6263.

Mishra, A.K.; Driessen, N.N.; Appelmelk, B.J.; Besra, G.S. *FEMS Microbiol. Rev.*, **2011**, *35 (6)*, 1126-1157.

Misra, A.; Hickey, A.J.; Rossi, C.; Borchard, G.; Terada, H.; Makino, K.; Fourie, P.B.; Colombo, P. *Tuberculosis*, **2011**, *91 (1)*, 71-81.

Mott, D.; Galkowski, J.; Wang, L.; Luo, J.; Zhong, C.-J. *Langmuir*, **2007**, *23 (10)*, 5740-5745.

Murdock, K.; Lin, Y.; Thomas, J.; Lang, Jr., S.A. *Journal of Medicinal Chemistry*, **1978**, *21 (4)*, 403-405.

Naik, R.R.; Stringer, S.J.; Agarwal, G.; Jones, S.E.; Stone, M.O. *Nat. Mater.* **2002**, *1 (3)*, 169-172.

Nair, J.; Rouse, D.; Bai, G.; Morris, S.L. *Molecular Microbiology*, **1993**, *10 (3)*, 521-527.

Nam, K.; Lee, Y.; Krauland, E. *ACS Nano*, **2008**, *2 (7)*, 1480-1486.

Nijamudheen, A.; Datta, A. *Journal of Molecular Structure: THEOCHEM*. **2010**, *945*, 93-96.

Novo, D.; Perlmutter, N.G.; Hunt, R.H.; Shapiro, H.M. *Cytometry*, **1999**, *35 (1)*, 55-63.

Palmal, S.; Jana, N.R. *WIREs Nanomed. Nanobiotechnol.* **2014**, *6*, 102-110.

Panáček, A.; Kvítek, L.; Prucek, R.; Kolář, M.; Večeřová, R.; Pizúrová, N.; Sharma, V.K.; Nevěčná, T.; Zbořil, R. *J. Phys. Chem. B*. **2006**, *110*, 16248-16253.

Pawley, J.B. Handbook of Biological Confocal Microscopy (3rd Ed.); Springer: New York, NY, 2006.

Payne, D.J. *Science*, **2008**, *321 (5896)*, 1644-1645.

Petroski, J,; Wang, Z.; Green, T.; El-Sayed, M.A. *Journal of Physical Chemistry B*, **1998**, *102 (18)*, 3316-3320.

Prozorov, T.; Mallapragada, S.K.; Narasimhan, B.; Wang, L.; Palo, P.; Nilsen-Hamilton, M.; Williams, T.J.; Bazylinski, D.A.; Prozorov, R.; Canfield, P.C. *Adv. Func. Mater.* **2007**, *17 (6)*, 951-957.

Rai, M.; Yadav, A.; Gade, A. *Biotechnology Advances*, **2009**, *27 (1)*, 76-83.

Ramon-Garcia, S.; Ng, C.; Anderson, H.; Chao, J.D.; Zheng, X.; Pfeifer, T.; Av-Gay, Y.; Roberge, M.; Thompson, C.J. *Antimicrobial Agents and Chemotherapy*, **2011**, *55 (8)*, 3861-3869.

Randall, L.; Woodward, M. *Research in Veterinary Science*, **2002**, *72 (2)*, 87-93.

Reyrat, J.M.; Kahn, D. *Trends Microbiol.*, **2001**, *9 (10)*, 472-473.

Riska, P.; Su, Y.; Bardarov, S.; Freundlich, L.; Sarkis, G.; Hatfull, G.; Carriere, C.; Kumar, V.; Chan, J.; Jacobs, Jr., W. *Journal of Clinical Microbiology*, **1999**, *37 (4)*, 1144-1149.

Riss, T.L.; Moravec, R.A.; Niles, A.L.; Benink, H.A.; Worzella, T.J.; Minor, L. *Assay Guidance Manual*, Eli Lilly & Co.: Bethesda, MD, 2004.

Rowland, K. *Nature News*, **2012**.

Rumack B.H.; Matthew, H. Acetaminophen poisoning and toxicity. *Pediatrics*. 1975; 55:871-876.

Schaaf, T.; Whetten, R. *J. Phys. Chem. B*, **1999**, *103*, 9394-9396.

Schwarz, S.; Kehrenberg, C.; Doublet, B.; Cloeckaert, A. *FEMS Microbiol. Rev., **2004** 28*, 519–542

Schwertmann, U.; Friedl, J.; Stanjek, H. *Journal of Colloid and Interface Science*, **1999,** *223*, 215-223.

Sheen, P.; Lozano, K.; Gilman, R.H.; Valenica, H.J.; Loli, S.; Fuentes, P.; Grandjean, L; Zimic, M. *Tuberculosis*, **2013**, *93 (5)*, 515-522.

Siddiqi, S.; Libonati, J.; Middlebrook, G. *Journal of Clinical Microbiology*, **1981**, *13 (5)*, 908-912.

Singh, A.; Reyrat, J. *Current Protocols in Microbiology*, **2009**, *Chapter 10 (C)*, 1-12.

Slocik, J.; Naik, R.; Stone, M.; Wright, D. *Journal of Materials Chemistry*, **2005**, *15 (7)*, 749-753.

Slocik, J.; Stone, M.; Naik, R. *Small*. **2005**, *1 (11)*, 1048-1052.

Smith, C.; Simpson, C.A.; Kim, G.; Carter, C.J.; Feldheim, D.L. *ACS Nano*, **2013**, *7 (5)*, 3991-3996.

Spellberg, B.; Guidos, R.; Gilbert, D.; Bradley, J.; Boucher, H. W.; Scheld, W. M.; Bartlett, J. G.; Edwards, J., Jr. *Clin. Infect. Dis.,* **2008,** *46 (2)*, 155-64.

Stahl, C.; Kubetzko, S; Kaps, I.; Seeber, S.; Engelhardt, H.; Niederweis, M. *Molecular Microbiology*, **2001**, *40 (2)*, 451-464.

Stumm, W.; Lee, G.F. *Aquatic Sciences*. **1960**, 295-320.

Sun, Q.; Margolin, W. *J. Bacteriol*. **1998**, *180 (8)*, 2050-2056.

Tan, Y.; Lee, J.; Wang, D. *JACS*, **2010**, *18*, 5677-5686.

Theil, E.C.; Takagi, H.; Small, G.W.; He, L.; Tipton, A.R.; Danger, D. *Inorganica Chimica Acta*, **2000**, *297 (1-2)*, 242-251.

Tinoco, Jr., I.; Sauer, K.; Wang, J.C. *Physical Chemistry: Principles and Applications in Biological Sciences*, 3rd ed.; Prentice Hall: Upper Saddle River, NJ, 1995.

Tran, M.L.; Zvyagin, A.V.; Plakhotnik, T. *Chem. Comm.* **2006**, 2400-2401.

Tyagi, J.S.; Sharma, D. *Trends Microbiol.*, **2002**, *10 (2)*, 68-69.

U.S. Geological Survey. Chemistry of Iron in Natural Water; Government Printing Office: Washington, D.C., 1962.

U.S. National Library of Medicine. Pulmonary Tuberculosis. http://www.nlm.nih.gov/medlineplus/ency/article/000077.htm (accessed February 10th, 2015).

Van Lehn, R. C.; Alexander-Katz, A. *Soft Matter*, **2011**, *7*, 11392-11404.

Van Lehn, R. C.; Atukorale, P. U.; Carney, R. P.; Yang, Y.-S.; Stellacci, F.; Irvine, D. J.; Alexander-Katz, A. *Nano Letters*, **2013**, *13*, 4060-4067.

Van Lehn, R. C.; Ricci, M.; Silva, P.H.J.; Andreozzi, P.; Reguera, J.; Voïtchovsky, K.; Stellacci, F.; Alexander-Katz, A. *Nature communications*, **2014**, *5*, 4482-4493.

Verma, A.; Uzun, O.; Hu, Y.; Hu, Y.; Han, H.-S.; Watson, N.; Chen, S.; Irvine, D. J.; \ Stellacci, F. *Nature materials*, **2008**, *7 (July)*, 588-595.

Wagner, A.; Mills, K. *Journal of Clinical Microbiology*, **1996**, *34 (7)*, 1672-1676.

Wang, Q.; Mercogliano, C.P.; Löwe, J. *Structure*, **2011***, 19*, 147-154.

Williams, R.; Jencks, W.; Westheimer, F. *pKa Data Compilation*. http://research.chem. psu.edu/brpgroup/pKa_compilation.pdf (accessed February 23, 2015).

Wong, A.O.; Heinecke, C.L.; Simone, A.R.; Whetten, R.L.; Ackerson, C.J. *Nanoscale*, **2012**, *4*, 4099-4102.

World Health Organization, *Global Tuberculosis Report 2013*, pp. 1-306.

World Health Organization. *Multidrug-resistant tuberculosis (MDR-TB)*, October 2013 Update.

World Health Organization. *Tuberculosis Fact Sheet °104.*

Xie, J.; Zheng, Y.; Ying, J.Y. *JACS*, **2009**, *131 (3)*, 888-889.

Yao, C.; Zhu, T.; Li, Y.; Zhang, L.; Zhang, B.; Huang, J.; Fu, W. *Clinical Microbiology and Infection*, **2010**, *16 (11)*, 1639-1643.

Yu, X.-C.; Margolin, W. *The EMBO Journal*. **1997**, *16 (17)*, 5455-5463.

Zhang, Y. *Annual review of pharmacology and toxicology*, **2005**, *45 (2)*, 529-564.

Zheng, J.; Petty, J.T.; Dickson, R.M. *JACS*, **2003**, *125*, 7780-7781.